# Electrical and Optical Properties of

# Upgraded Metallurgical Grade Silicon Solar Cells

**by**

**Jae Young Kwon**

A dissertation submitted in partial fulfillment

of the requirements for the degree of

Doctor of Philosophy

(Materials Science and Engineering)

in the University of Michigan

2013

Doctoral Committee:

Assistant Professor Akram Boukai, Chair

Associate Professor Jamie D. Phillips

Associate Professor Max Shtein

Assistant Professor Anish Tuteja

*Dedicated to my family*

*for being the biggest supporters throughout my school years..*

# Acknowledgements

First and foremost I would like to acknowledge my advisor, prof. Akram Boukai. Throughout the past years, I received guidance and interesting suggestions from him which were very helpful for accomplishing my research successfully. I really enjoyed solar cell research and various experiences in Boukai group. I also hope that my advisor continues successful career in his startup as well.

I also acknowledge the members of my thesis committee, prof. Jamie Phillips, prof. Max Shtein, and prof. Anish Tuteja. All of the professors gave me helpful comments and showed great interest in my research since my candidacy proposal presentation. Particularly struggling with prof. Shtein's huge amount of questions during my data meeting helped me to develop stronger background on the theoretical parts of my study and this made me understand my experimental results more clearly. Thank you for your attention and comments. I also thank prof. Tuteja and his group for the fruitful collaborations.

I also won't forget the good times I had with our group members. I truly thank Dr. Duckhyun Lee with whom I have worked together during the last three years. He was like my second advisor throughout my study and I have learned how to carry out projects and organize results from him. I could not have achieved all the high quality results without Dr. Lee's guidance and collaborations. I hope he could become a good professor soon and conduct more fascinating projects. Good luck Duckhyun! Also Xiao Guo and

Bingyuan Huang, and Craig Shaner, I will never forget the times we spent together getting training and working hard in the clean room. It was my great pleasure to work with you guys in the Boukai group and good luck with your preparation for graduations!

I would like to acknowledge all the good people I met at the University of Michigan. I had wonderful time with my MSE friends, Gibum Kwon, Myungkoo Kang, and Peter Chung having joyful talk in the office. Also Jinyoung Hwang (Dr. Hwang), thanks a lot for discussing solar cells with me and being my closest friend especially during the later days my Ph.D.

Last but certainly not least, I would like to acknowledge my family. I could not have come this far without support and encouragements I have gained from my parents. I am truly grateful for their endless love and prayers which led me to finally achieve this degree.

# Table of Contents

# List of Tables

# List of Figures

# Abstract

Silicon(Si) accounts for more than ~ 90 % of solar cell market due to its advantages of earth abundance, good reliability, performance, and a wealth of Si materials processing knowledge. However, as the photovoltaic industry matures, there have been more demands on lowering the cost of solar cells, which is mainly dominated by the cost of starting materials. Currently two major approaches are pursued to reduce the cost of Si- based solar cells per watt: the adoption of low-cost silicon such as metallurgical-grade (MG) Si or upgraded metallurgical-grade (UMG) Si, and reducing the usage of Si by producing ultrathin solar modules. UMG-Si is generally obtained by special heat treatment of MG- Si and is a much cost–efficient material compared to the solar-grade Si. However, UMG-Si contains high level of various metal impurities and defects which leads to diminished diffusion length and poor performance. Therefore, in order to achieve efficient photo-generated charge collection from a p-n junction made from low quality Si, the thickness of the solar cell should be within the diffusion length, particularly less than ~ 20 μm for the application of UMG-Si. Si thickness in this range does not allow sufficient light absorption and thus, designing of the structure of ultrathin solar cells to have optically thick active layer, so that the light absorbance can be improved, becomes very important.

Strategies to enhance optical absorbance in the solar cells include dielectric-anti reflection coating, surface texturing and exploitation of surface plasmon resonance.

Among them, the surface plasmon resonance, which is the collective oscillation of conduction electrons stimulated by incident light at the interface between a metallic (Ag, Au, Pt) nanostructure and a dielectric, has been an emerging method for achieving the light trapping in ultrathin Si solar cells.

This thesis presents ultrathin Si solar cells generated from UMG-Si wafers incorporating combinations of nanostructures that enable use of surface plasmon resonance, light scattering feature, and anti-reflection layers. Detailed studies of electrical and optical properties of the resulting solar cells provide useful design considerations for future MG-Si based and any classes of solar cell systems.

# Chapter 1

# Introduction

## 1.1 Low cost Si for Solar Cells

### 1.1.1 Solar Energy Utilization

Exploitation of clean renewable energy resources has attracted great interest due to limited supply of fossil fuels and efforts to reduce greenhouse gas emission. Among various renewable energy resources, solar energy is considered the most promising source as it provides $10^{17}$W of energy to the earth. This is more energy in one hour striking the earth than all of the energy currently consumed by humans in an entire year. However, currently less than 0.1% of the worldwide energy usage is being covered by solar energy due to the high cost of solar electricity (0.25 ~ 0.5 $/kWh) compared to the fossil based electricity [1, 2]. To harness the solar energy as our primary source, sunlight should be captured, converted, and stored in a cost-effective way. A Solar Cell is a device that enables capturing and converting the solar energy and has been extensively studied since 1950s [3]. The cost of electricity generated from solar cells need to be further reduced than current level for widespread adoption of solar energy and researches in this field are aimed at reducing the solar cell's cost which is mainly governed by the cost starting material and processing.

Various materials such as organics [4-8], thin films (CdTe, CIGS, amorphous-Si) [9-16], compound semiconductors [17-21] have been studied for solar cell applications. Nonetheless, Si remains the dominant choice for solar cell material [22-24]. Advantages of Si include its bandgap of 1.1eV, which is close to the optimum level (1.4eV) for photovoltaic conversion, earth abundance, excellent reliability, and wealth knowledge background in microelectronics based on monocrystalline Si. The theoretical conversion efficiency of a single bandgap Si solar cell, so called detailed balance limit [25], is 31% and the highest recorded efficiency based on monocrystalline Si solar cells fabricated from laboratory have reached ~ 25%, obtained by the PERL cell developed at the University of New South Wales [26].

Currently, polycrystalline Si wafer (99.99999%) is the most widely used material for Si solar cell production [27]. Around 30% of cost of Si-based solar module is the cost of polycrystalline Si wafers due to the complexities is purifying Si[28, 29]. Simplifying the purification procedures and using low-quality Si can reduce the cost of resulting Si solar module.

### 1.1.2 Silicon Preparation for Solar Cells

Process of producing Si wafers involves extraction, purification, crystallization and sawing procedures. In nature, Si is generally found in a form of silica ($SiO_2$) or silicates. Extracting Si starts with annealing these sources in electric arc furnaces where the temperature reaches higher than 2000°C [30]. The reactions occur in this step are:

$$SiO_2 + 2C \rightarrow Si + 2CO_2 \quad (1.1)$$

$$SiO_2 + 2C + O_2 \rightarrow Si + 2CO_2 \quad (1.2)$$

The Si obtained in this step is called, metallurgical-grade (MG) Si and the purity level is 98~99%, which is not suitable for solar cells or other electronics. As the MG-Si undergoes more directional solidification (generally twice), metal impurities can be significantly reduced. However, some elements with high segregation coefficients, such as boron (B), phosphorous (P) and aluminum (Al) cannot be easily removed [31]. Moreover, these elements act as dopants in Si and their amount should be reduced or controlled so that the electrical properties of the resulting Si can be identified. Having MG-Si react with hydrogen chloride (HCl) gas to form volatile chlorosilanes including trichlorosilane ($SiHCl_3$), followed by distillation and pyrolysis reduction reaction produce fine grain solar-grade polycrystalline Si with much lower dopant impurities [30, 31]. This process of purification is called Siemens method. The possible reactions during the process are as follow.

$$Si + 3HCl \rightarrow SiHCl_3 + H_2 \quad (1.3)$$

$$2SiHCl_3 \rightarrow Si + HCl + SiCl_4 \quad (1.4)$$

The polycrystalline Si obtained from repeating above process is composed of fine grains and grain boundaries whose purity is ~7N. The polycrystalline Si can become monocrystalline Si as it goes through crystallization step by employing Czochralski method, however this process makes Si expensive and such high quality Si is not necessarily required for solar cell production. Moreover, Siemens method of purifying MG-Si has been already considered expensive due to the complex process and it also lays possibilities of losing chlorinated gases in the atmosphere which can be severe environmental problem.

Current solar cell research is turning attention to exploitation of cheaper starting materials than polycrystalline Si such as amorphous thin film Si or upgraded metallurgical grade Si (UMG-Si) [32-34]. UMG-Si, which requires much simple purification process, is generally produced by purifying MG-Si without chlorine but annealing and crystallizing with a special temperature treatment during casting of the ingots [30]. It costs approximately $10/kg, which makes it almost 5-10 times less expensive than polycrystalline Si [35]. The main disadvantage of using UMG-Si for solar cells is the high impurity level (~ 5N) of the material which leads to decreased minority carrier diffusion length and thus diminished device efficiency. Hence, in order to utilize UMG-Si for solar cells, small physical thickness of the overall device that allows shorter pathway from metallurgical p-n junction to the electrode or other innovative device designs such as radial p-n junctions [36, 37] are required for efficient carrier collection.

## 1.2 Solar Cell Operation Physics

### 1.2.1 Photocurrent and Quantum Efficiency

In order to evaluate optical absorbance, reflectance and performance of a solar cell, the spectral distribution of incident solar flux should be known. The solar irradiances vary due to seasonal and daily variations, the position of the sun with respect to the Earth, and the condition of the atmosphere. For convenience, a reference solar spectrum is required. The standard terrestrial solar spectrum is defined as the Air Mass 1.5 (AM 1.5) spectrum which represents an average atmospheric attenuation due to incident sunlight

arriving from varying angles throughout the day. The AM 1.5 spectrum has an irradiance of 853W/$m^2$ for direct or 1000W/$m^2$ for direct and diffuse light. The most widely used reference solar cell device simulation is the AM 1.5 spectrum that includes both direct and diffuse which is shown in Fig. 1.1 [38].

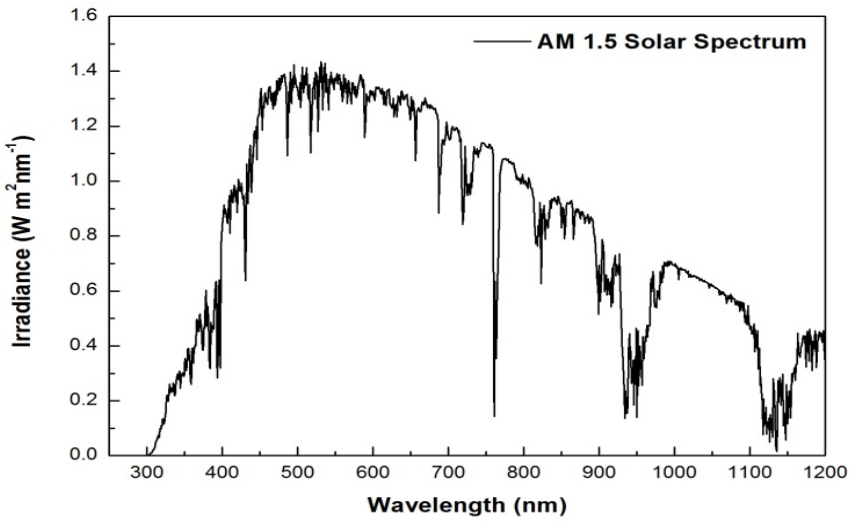


**Figure 1.1 Spectral distribution of AM 1.5 provided from NREL [38].**

Photocurrent from a solar cell results from the net absorbed flux due to the sun. Current density measured from a solar cell when light is present without load, is short circuit current density. If we assume that each electron has a probability $\eta_c(E)$ of being collected, the short circuit current density ($J_{SC}$) can be calculated from the below equation.

$$J_{SC} = q\int_0^{\infty} \eta_c(E)\big(1 - R(E)\big)a(E)b_s(E)dE \qquad (1.5)$$

Where a(E) is absorbance, R(E) is reflectance, and $b_S(E)$ is solar photon fluxof a photon of energy E. A solar cell's external quantum efficiency (EQE) at E is the probability that

an incident photon of energy E will deliver one electron to the external circuit. To put it simply, it is the ratio of number of electrons flowing per second in the external circuit of a solar cell to number of photons provided to the solar cell per second of a specific energy. In eq. (1.5), the term $\eta_c(E)(1-R(E))a(E)$ indicates EQE of a solar cell. Hence, combination of the absorption of light, separation and the collection of photogenerated carriers in a solar cell are reflected in the EQE. Substituting EQE to eq. (1.5) gives

$$J_{SC} = q\int_0^{\infty} EQE(E)b_s(E)dE \tag{1.6}$$

If EQE is 1, which is an ideal case, it means that the cell is absorbing 100% of incident photons and the electron-hole pairs generated by the photons are completely being collected. There is another quantity called, internal quantum efficiency (IQE), which is a ratio of the number of charge carriers collected by a solar cell to the number of absorbed photons. In other words, this is the ratio of EQE to absorbance, which informs how well the device converts absorbed photons to external current. Hence if IQE is 100%, it implies that every absorbed photons result in decoupled electron-hole pairs and that all the photo-generated carriers contribute to photocurrent. Both EQE and IQE are useful parameters for evaluating the performance of a solar cell.

### 1.2.2 Power Output from a Solar Cell

Solar cell is simply a diode, which is mainly composed of a p-n junction that creates a special asymmetry to decouple light generated electron-hole pairs, and ohmic contacts to extract electric power to the outer circuit. Fig. 1.2 (a) illustrates the basic structure of a solar cell under illumination. When light with energy greater than the bandgap of the solar cell material is absorbed, electron-hole pairs are generated at various

locations throughout the cell. The photogenerated carriers on each side of the p-n junction diffuse into the depletion region where they are spatially separated and driven through the external circuit by the built-in-potential barrier.

When bias is applied to the cell in the dark, the built in potential barrier is reduced and more majority carriers are able to diffuse across the junction, and consequently there is now a net current of electrons from n to p and holes from p to n. The current that flows through the cell is combination of contributions from the minority carrier diffusion current, $J_{diff}$, and the recombination current in the space charge region, $J_{scr}$. However, in indirect bandgap materials like Si, diffusion lengths are normally longer than the depletion width and very little recombination occurs in the depletion region, so $J_{scr}$ is negligible. $J_{dark}$ can be expressed as,

$$J_{dark} \approx J_{diff,0} \left(e^{\frac{qV}{k_B T}} - 1\right) \tag{1.7}$$

This is the ideal diode equation which is also quoted for the dark current of a solar cell. However, in real case, several other factors can affect the diode behavior and the $J_{dark}$ can appear as

$$J_{dark} \approx J_0 \left(e^{\frac{qV}{mk_B T}} - 1\right) \tag{1.8}$$

Where $J_0$ is a constant that depends on the material and m is the ideality factor[39]. In ideal case, m=1. In real cells, due to some recombination currents, m can be even greatethan 2 [40].

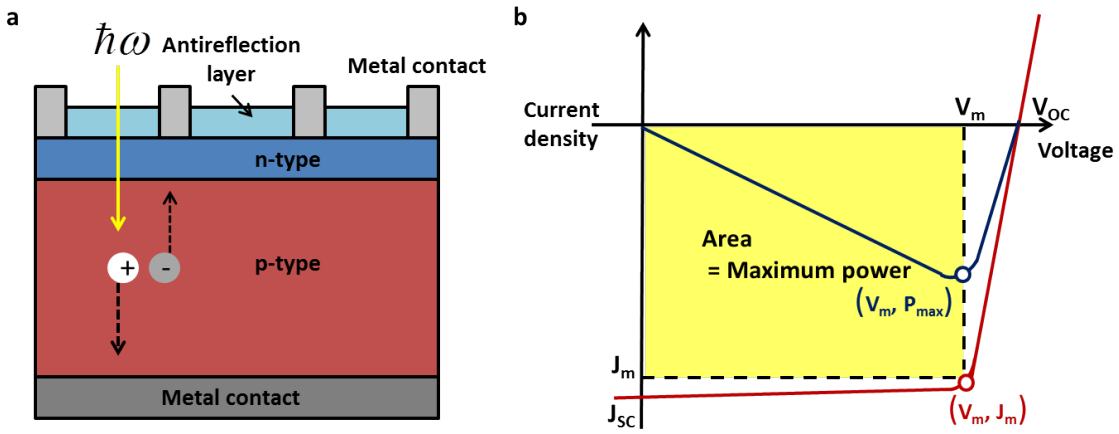


**Figure 1.2 (a) Schematic of a p-n junction solar cell under illumination. Photogenerated carriers diffuse into the depletion region where they are swept into the adjacent region by the built-in-potential. (b) Generic current density (J) – voltage (red) and power (P) – voltage (blue) characteristics of a solar cell under illumination. Power density reaches maximum at $V_m$ close to $V_{OC}$. The maximum poer density $J_m \times V_m$ is given by the area of the inner rechtangle (yellow).**

When a load is connected between the terminals of the illuminated cell, the overall current density of the cell is given by subtracting the current density that flows in the cell when the bias is applied in the dark (dark current) from the integrated short circuit current density. Overall current density at bias in ideal case, J (V) is

$$J(V) = J_{SC} - J_0 \left(e^{\frac{qV}{k_B T}} - 1\right) \tag{1.9}$$

As the bias (V) increases, the net current density becomes zero. The voltage when this occurs is open circuit voltage ($V_{OC}$) and from eq (1.9), we get

$$V_{OC} = \frac{k_B T}{q} \ln\left(\frac{J_{SC}}{J_0} + 1\right) \tag{1.10}$$

The above equation shows that photovoltage is obtained only when the forward bias is applied.

The typical J-V characteristic of a solar cell is shown in Fig. 1.2 (b). The solar cell generates power when the applied bias lies between 0 and $V_{OC}$. The power density from a solar cell is product of current density and voltage (P = JV). Fill factor (FF) is a parameter that tells how close the J-V characteristic of the device is to the ideal diode behavior. It is given by

$$FF = \frac{J_m V_m}{J_{sc} V_{oc}} \tag{1.11}$$

Where $J_m$ and $V_m$ are current density and voltage where the power reaches maximum. The closer the FF to the maximum, which is unity, the better the device is considered to perform. In case of silicon, its maximum value is 0.88. The efficiency (η) of a solar cell is defined as a ratio of power at the maximum operating level ($J_m V_m$) to the power from the sun ($P_s$),

$$\eta = \frac{J_m V_m}{P_s} \tag{1.12}$$

If we relate the efficiency (η) with $J_{SC}$, $V_{OC}$, and FF,

$$\eta = \frac{J_{sc} V_{oc} FF}{P_s} \tag{1.13}$$

As discussed in 1.2.1, the standard test condition of solar cells is the AM 1.5, an incident power density of 1000W/$m^2$, and a temperature of 25°C. This condition is often referred as 1 Sun [40].

## 1.3 Flexible Inorganic Devices Generated from Wafers

Increase in demand for unusual properties in electronic devices, such as nano-scale dimensions, flexibility, and transparency, has brought applications of unconventional materials such as nanowires [41, 42], thin films [43, 44] and organics[45, 46] to devices and much progress in fabrication techniques. Although these materials have shown some promising results, uncertain reliability, poor performance compared to crystalline-based inorganic devices, and difficulties in assembling nanoscale features for large areas have been critical drawbacks in device applications. In recent years, various electronic devices based on ultrathin monocrystalline inorganic semiconductor (Si, GaAs, GaN) elements generated from wafer forms have been introduced by John Rogers' group at UIUC [47-49]. The inorganic semiconductor elements created from innovative means of processing of wafers are called "ribbons" and they are integrated into device by lying on flexible supporting substrates which enables mechanical bendability to the final device [47]. Moreover, since the devices are based on crystalline semiconductors, they show comparable performance and reliability to conventional bulk form of devices.

According to the previous works, the undercut etching which is the key procedure to release the ultrathin ribbons from the wafer, has been carried out by wet chemical anisotropic etching which is highly dependent on the orientation of the wafer [48]. Thus the starting material to produce the ribbons has been constrained to monocrystalline wafers which are expensive for solar cell application. However, by implementing proper isotropic dry etching, complete undercut can be achieved regardless of the orientation of the material. This approach can offer expanded options of starting materials to produce ultrathin flexible device including polycrystalline wafers.

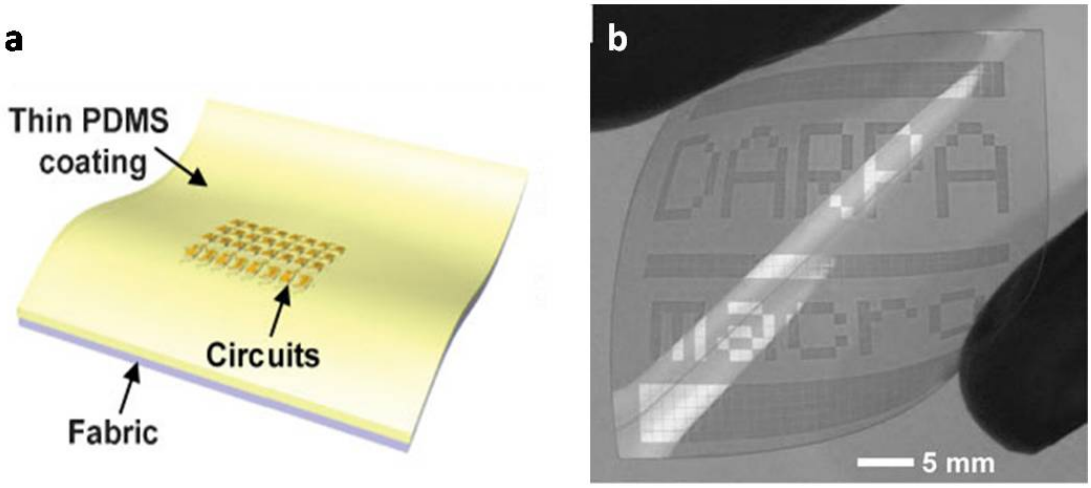


**Figure 1.3 (a) Schematic of a flexible electronic device composed of ribbons, electrodes, and polymeric supporting substrate lying on a fabric [48]. (b) An optical image of ultrathin flexible microscale Si elements on plasmic [49].**

## 1.4 Localized Surface Plasmon Resonance

Surface plasmon polaritons are electromagnetic excitations propagating at the interface between a dielectric and a conductor, usually a metal. These surface waves arise by the coupling of the electromagnetic field (light) to oscillations of the conductor's electron plasma. Confinement of these waves to the small sphere (nanoparticle) sphere gives rise to resonant electromagnetic behavior and unique properties. The resonant behaviors of surface plasmons in metallic nanoparticles with a diameter a << λ, where λ is the wave length of light in the surrounding medium is called localized surface plasmon resonance (LSPR) [50-53].

### 1.4.1 Surface Plasmon in a Single Nanoparticle

When a particle's diameter size (a) is much smaller than the wavelength, below 100 nm, and is subjected to an external optical wave, the phase of the oscillating electromagnetic field can be considered to be constant over the particle volume. This

quasistatic assumption serves well to explain the plasmonic properties in metallic nanoparticles [54, 55]. As illustrated in Fig. 1.4 (a), the external light's wave displaces the electrons in the metal with respect to the lattice ions and hence creates buildup of polarization charges on the particle surface. Because these charges also attract each other, they act as restoring force, oscillating electrons allowing resonance to take place at a certain frequency. The quantum of these oscillating electrons is surface plasmon. For a small metallic sphere, the dipole moment (**p**) and the polarizability (α) formed inside its volume are given as

$$\mathbf{p} = 4\pi\varepsilon_0\varepsilon_m a^3 \frac{\varepsilon(\omega)-\varepsilon_m}{\varepsilon(\omega)+2\varepsilon_m} \tag{1.14}$$

$$\alpha = 4\pi a^3 \frac{\varepsilon(\omega)-\varepsilon_m}{\varepsilon(\omega)+2\varepsilon_m} \tag{1.15}$$

where a is the diameter of the particle, $\varepsilon_m$ is the dielectric constant of the medium, and $\varepsilon(\omega)$ is the dielectric function of the sphere. From the above equations, it is apparent that the polarizabiliy undergoes resonant enhancement when $|\varepsilon + 2\varepsilon_m|$ is minimum [55]. This relationship is called the Fröhlich condition and it reveals large dependence of the resonance frequency (ω) on the material of the sphere and the dielectric environment ($\varepsilon_m$). There have been numerous reports regarding tuning the plasmon resonance peaks by engineering the surrounding dielectric matrix which also supports this relationship [56-58]. For example, Ag or Au particles with diameter a << λ surrounded by air, have resonance peaks at ~ 350 nm and ~ 480 nm respectively [59]. However, these spectral positions redshift when the dielectric constant of the environment increases due to the buildup of polarization charges on the dielectric side of the interface which screens the surface charges on the metal sphere and results in reduction of the restoring force. Fig.

1.4 (b) [60] depicts the electric field distribution when a consistent external field pointing right is confronting a small metal sphere. The surface charges on the particle builds resonantly enhanced field inside the sphere and also produces dipolar field outside the sphere. The strong amplification of the electric field intensity $|\mathbf{E}|^2$can be 100 to 10,000 times greater in magnitude than the incident electric field [61-63].

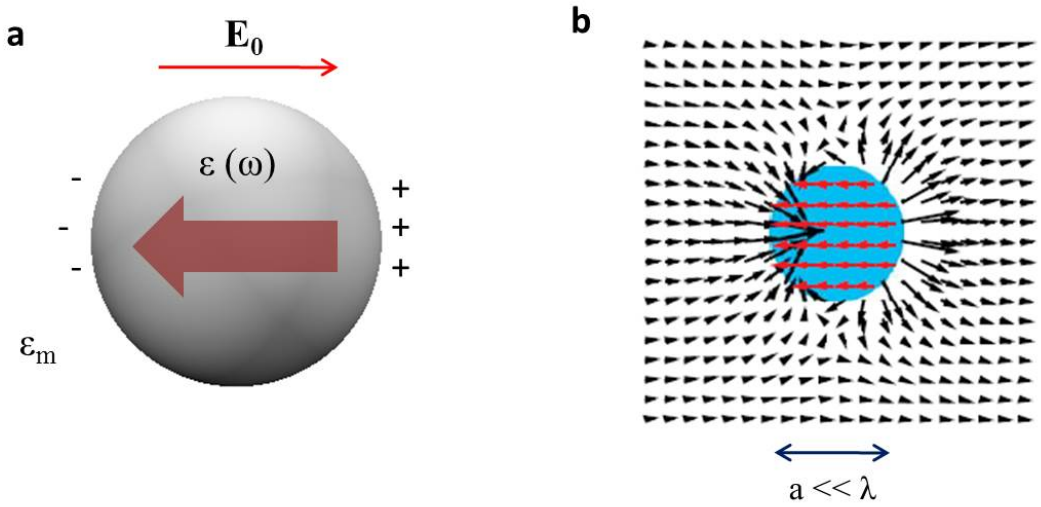


**Figure 1.4 (a) Polarization (electric field pattern) for TM (transverse magnetic) modes due to interaction of light with a small sphere. When the particle size is much smaller than the wavelength of the light, only dipolar mode exists. (b) The electric field (black arrows) from displaced electrons is greatly amplified on opposite sides just outside the metallic sphere. Inside the sphere, the electric field is uniform (red arrows) and is on the same order of magnitude as the local field just outside the sphere [60].**

## 1.4.2 Enhanced Scattering of light from Nanoparticles

When Fröhlich condition is satisfied, resonantly enhanced polarization α also enhances the scattering effect by the metallic nanoparticle and light absorption in the nanoparticle. The cross sections for scattering ($C_{sca}$) and absorption ($C_{abs}$) of a sphere of volume V and dielectric function $\varepsilon = \varepsilon_1 + i\varepsilon_2$ are given by[53]

$$C_{sca} = \frac{k^4}{6\pi}|\alpha|^2 \quad (1.16)$$

$$C_{abs} = k\mathrm{Im}[\alpha] \quad (1.17)$$

where α is polarizability as in eq (1.15) and k is the wave number. The extinction cross section ($C_{ext}$) of a sphere which is summation of its absorption cross section ($C_{abs}$) and scattering cross section ($C_{sca}$) is given as

$$C_{ext} = 9\frac{\omega}{c}\varepsilon_m^{3/2}V\frac{\varepsilon_2}{[\varepsilon_1 + 2\varepsilon_m]^2 + \varepsilon_2^2} \quad (1.18)$$

The extinction cross section equation shows that its magnitude is proportional to the volume of the small sphere. For particles of larger dimensions whose diameter is greater than 100 nm, point dipole prediction is not justified because of significant phase changes of the driving field over the particle volume and hence, rigorous electrodynamic approach is required to describe the plasmonic phenomenon. In 1908, Mie developed a theory of the scattering and absorption of electromagnetic radiation by a sphere [64] and this Mie theory is still applicable. However, we will not cover this part since the diameters of the nanoparticles we produced are less than 50 nm and their properties can be explained by the point dipole model.

The light scattering from a small metal sphere in a homogeneous medium is symmetric. Fig. 1.5 (a) shows 3-D surface plot of scattering pattern of a point dipole located at (0, 0, 0) oscillating in x direction. However when this particle is placed at the interface between two dielectrics, light scatters preferentially into the dielectric with larger permittivity. Fig. 1.5 (b) [65] shows radiation patterns of a point dipole oriented parallel to the surface in air (black line) and at 20 nm above Si substrate (blue dashed

line). In air, the radiation of the dipole is symmetric perpendicular to the surface whereas near Si, most of the light is radiated into Si. This is related to high density of optical modes within Si compared to air. The result is higher light absorption of underlying material from which application of light scattering nanoparticles to the solar cells stems [65-71].

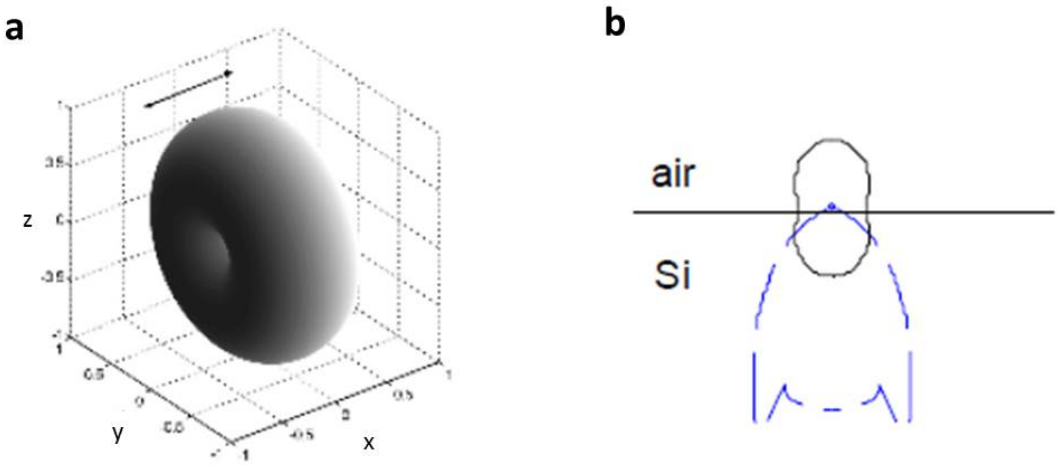


**Figure 1.5 (a) 3-D surface plot of radiation pattern of a dipole located at (0, 0, 0) oscillating in the x direction. (b) Radiation patterns for a point dipole oriented parallel to the surface at a distance of 20 nm from a Si substrate (blue dashed line). The radiation pattern for the case of free space is shown for reference (black solid line) [65].**

The geometry of a single metal nanoparticle also is one of the primary factors that determines the surface plasmonic resonance and scattering efficiency [61]. Fig. 1.6 (a) shows an example of dipolar plasmon line shapes of colloidal Ag particles of different shapes. Although the Ag particles in Fig. 1.6 (a)[72] are in similar volume, their different shapes result in different charge distribution on the metal surface and consequently the scattering peaks which is similar to the resonance peaks, appear at different wavelengths. Fig. 1.5 (b) shows scattering efficiency of Ag nanoparticles on Si with various shapes and

sizes [59]. The scattering fraction shows that smaller nanoparticles, with their effective dipole moment located closer to the semiconductor layer couple a larger fraction of the incoming light to the underlying layer. In this study, due to ease of fabrication, nanoscale hemisphere on Si structure was employed for inducing plasmonically enhanced scattering.

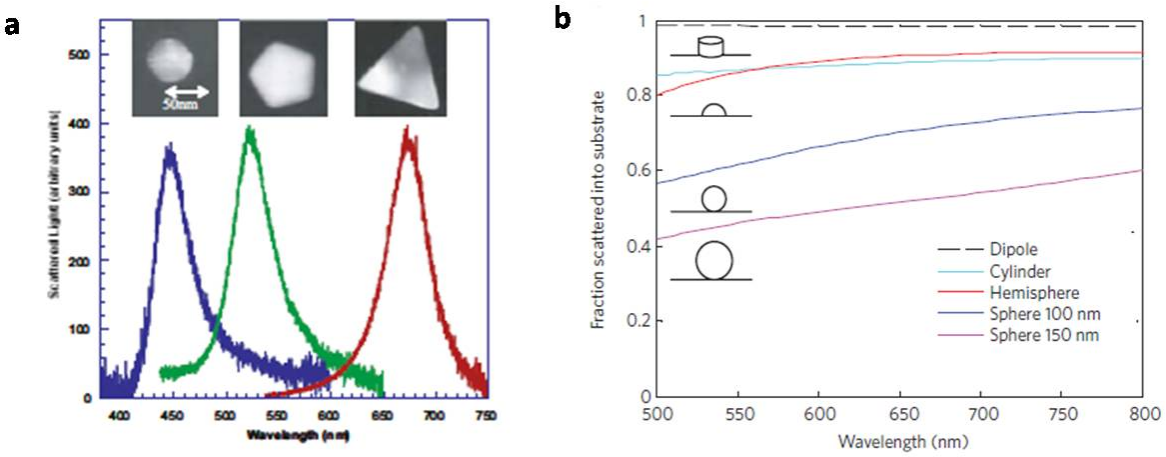


**Figure 1.6 (a) Scattering spectra of single Ag nanoparticles of different shapes obtained in dark-field configurations [72]. (b) Fraction of light scattered into the substrate divided by total scattered power, for different sizes and shapes of Ag nanoparticles on Si [59].**

## 1.4.3 Surface Plasmons in Arrays of Nanoparticles

In ensembles of metal nanoparticles, additional shifts can occur due to electromagnetic interactions between the localized surface plasmons. For small particles (diameter << 100 nm), the interactions can be treated as an ensemble of interacting dipoles. Depending on the interparticle spacing d, plasmon peaks can be shifted from the case where isolated single particle is present. When the particles are closely spaced, $d << \lambda$, near-field interactions with a distance dependence of $d^{-3}$ dominate [73, 74]. Taking account of an array of metal nanoparticles as interacting point dipoles, the direction of the resonance shifts for in-phase illumination can be determined by types of polarizations in

the nanoparticles. Fig. 1.7 illustrates that the restoring force acting on the oscillating electrons is either increased or decreased by charge distributions of neighboring particles [55]. The polarization direction in the nanoparticles depends on the polarization of the exciting light and either blue-shift of red-shift can occur.

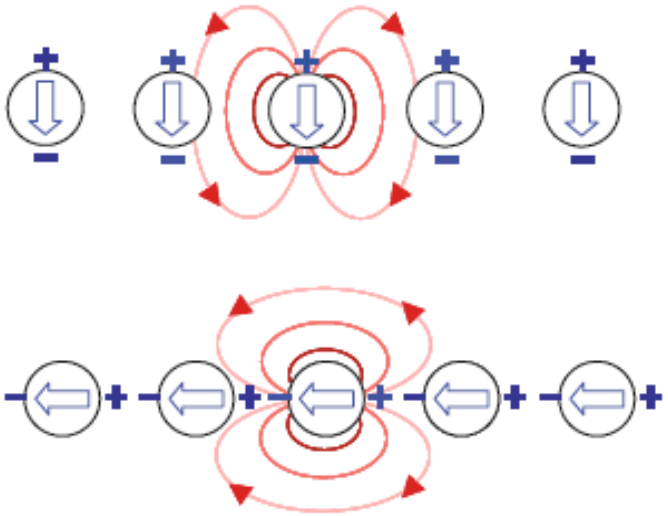

**Figure 1.7 Schematic of near-field coupling between metallic nanoparticles for the two different polarizations. For the excitation of transverse modes, blue-shift occurs whereas the excitation of longitudinal modes, red-shift occurs [55].**

Besides the polarization of the incident field, interparticle distance also affects the shifts in resonance energy. Fig. 1.7 (a) shows arrays of 50 nm size Au nanoparticles with varying interparticle distance [73]. The dependence of the spectral position of the plasmon resonance on interparticle distance is shown in Fig. 1.7 (b) both for transverse and longitudinal polarization [73]. In this system, particle distance in excess of 150 nm is sufficient to recover the behavior of isolated particles.

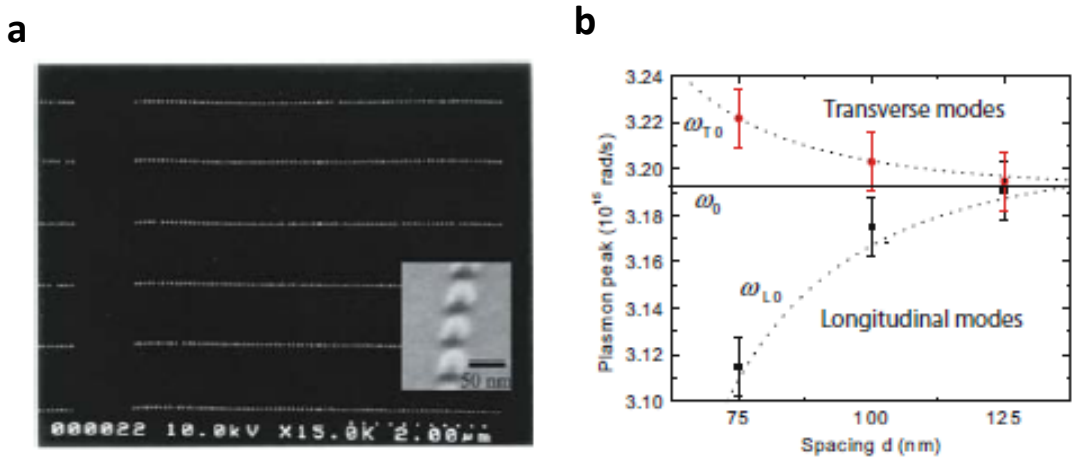


**Figure 1.8 (a) SEM image of arrays of closely spaced Au nanoparticles and (b) dependence of the spectral position of the dipole plasmon resonance on interparticle spacing. The dotted lines show a fit to the $d^{-3}$ of the coupling [73].**

There have been great amount of works in investigating properties and applications of plasmonic resonances in metal particles, especially in photonic relevant applications such as chemical/biological sensing [75-79] , optical waveguides[52, 80-82], and surface-enhanced Raman scattering [62, 83, 84] . The pioneering work in the field of plasmonic enhancement in light-sensitive device was accomplished by Stuart and Hall who demonstrated the enhancements in photocurrent from a photodetector by distributing Ag nanoparticles on the surface of the device [85] .

The field of plasmonics is also gaining huge amount of interests from solar cell researchers as exploitation of LSPR can be a new route to improve absorbance and performance of solar cells while permitting small physical thicknesses [67, 86-88]. In order to make use of LSPR of nanoparticle systems advantageously, nanopatterning technique that enables producing metallic nanoscale features is required.

## 1.5 Nanopatterning Techniques

Conventional lithography techniques include photolithography and maskless scanning-beam based techniques such as electron beam lithography or focused ion beam lithography. However the resolution from employing photolithography which is limited by diffraction cannot be scaled below ~ 500 nm ranges. Scanning-beam techniques yield sub 50 nm scale patterns but require long exposure time and high cost. To overcome these drawbacks, numerous unconventional nanopatterning techniques which allow fabrication of nanoscale features with periodic sizes and shapes have been developed. In this section, nanoimprinting lithography and block copolymer self-assembly which can bring high-throughput and low-cost is demonstrated.

### 1.5.1 Nanoimprinting

Nanoimprinting is a simple process that is basically divided into two steps as shown in Fig. 1.9 (a) [89]. The first step is the imprinting step in which a mold with nanopatterns on its surface is pressed into a thin resist cast on a substrate with proper pressure, temperature, and pressing time. The resultant topography on the resist is an inverse image of the original mold as shown in Fig. 1.9 (b) [90] . The second step is the pattern transfer where an isotropic dry etching process, such as reactive ion etching is employed to remove the residual resist in the compressed area. Since this lithography process does not use any energetic beams, the resolution is not limited by the effects of wave diffraction, scattering and interference in the resist and therefore ultrahigh resolution can be obtained without much difficulty. The mold used in the imprint lithography is generally made by using a high-resolution but low- throughput lithography which lays issues of mold fabrication costs.

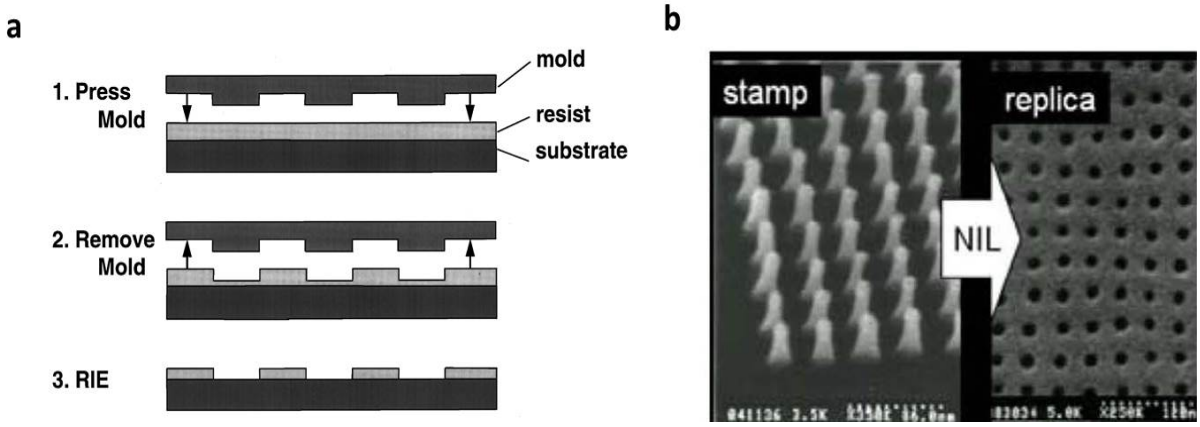


**Figure 1.9 (a) Schematic of nanoimprint process: (1) imprinting to form thickness contrast in resist, (2) mold removal, and (3) pattern transfer via reactive ion etching (RIE) [89]. (b) SEM images of a nanoimprinting mold (stamp) and replicated morphology [90].**

## 1.5.2 Block Copolymer Self Assembly

Block Copolymer is composed of two or more chemically distinct polymer blocks, which are covalently bonded together to form a larger, more complex macromolecule. Fig. 1.10 (a) depicts a schematic of diblock copolymers containing two different blocks, A and B [91]. Diblock copolymers spontaneously self-assemble into microphase-separated nanometer-sized domains (10 nm ~ 50 nm) that exhibit ordered morphologies due to connectivity constraints and incompatibility between the two blocks [92, 93]. Self-assembly of block copolymers have been extensively studied from 1960s and applications of this property to obtain block copolymer thin films with various morphologies have been proposed from 1995 [94-96].

In a given diblock copolymer bulk system, the resulting morphology is strongly determined by the composition. As shown in Fig. 1.10 (b) [91], the variety of morphologies include spheres (S), cylinders (C), bicontinuous gyroids (G), lamellae (L),

and etc. There are three parameters that influence the phase separation of the diblock copolymers [91, 93]: (1) the volume fractions of A and B blocks ($f_A + f_B = 1$), (2) the total degree of polymerization ($N = N_A + N_B$), and (3) the Flory–Huggins parameter ($\chi_{AB}$), which indicates the degree of incompatibility between the A and B blocks. The Flory - Huggins parameter is related to enthalpic contribution for phase separation. In binary phase system the enthalpy change as a result of mixing A and B is

$$\Delta \mathrm{H_m} = \mathrm{k_B T} N_\mathrm{A} f_\mathrm{B} \chi_\mathrm{AB} \tag{1.19}$$

The total free energy of mixing A and B is

$$\Delta \mathrm{G_m} = \mathrm{k_B T} \left\{ \frac{f_\mathrm{A}}{N_\mathrm{A}} \ln(f_A) + \frac{f_B}{N_\mathrm{B}} \ln(f_B) + f_A f_B \chi_{AB} \right\} \tag{1.20}$$

When the $\Delta G_m$ is greater than 0, phase separation is thermodynamically stable. The theoretical phase diagram shown in Fig. 1.10 (c) [91] reflects the relationships between the morphologies and three parameters. The degree of microphase separation of diblock copolymers depends on the segregation product, $\chi N$, which reflects segregation strength of the constituents. The incompatibility between the constituent polymers decreases as the temperature of the environment increases or $\chi N$ decreases. As this condition continues, the block copolymer undergoes order-to-disorder transition and finally become disordered.

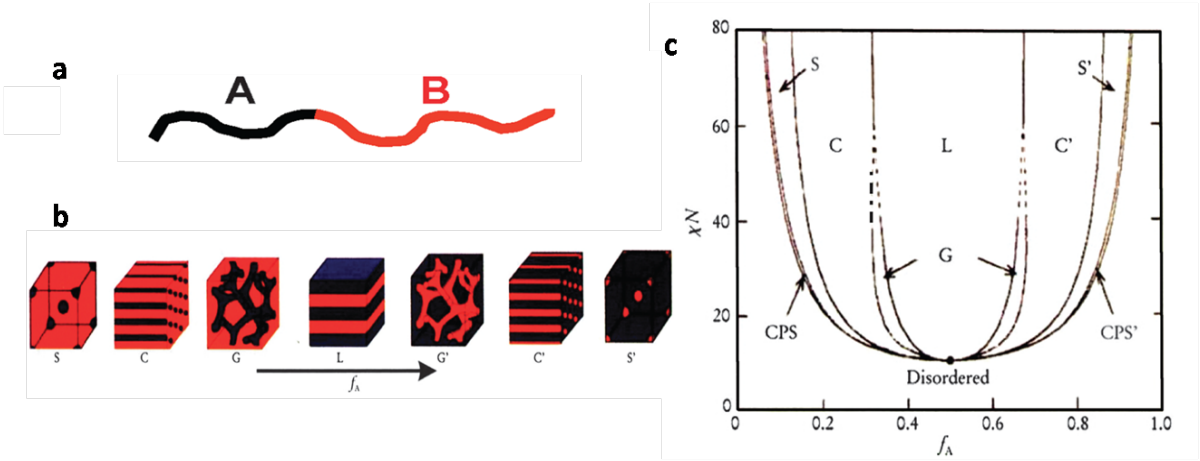


**Figure 1.10 (a) Typical structure of diblock copolymer containing two types of blocks, A and B. (b) Various equilibrium morphologies of AB diblock copolymers in bulk. (c) Theoretical phase diagram of AB diblocks predicted by self-consistant mean-field theory, depending on the volume fraction (*f*) of the blocks, and the segregation parameter, $\chi N$, where $\chi$ is the Flory – Huggins segment – segment interaction energy and $N$ is the degree of polymerization [88].**

The chemical dissimilarities between the constituents of the self-assembled film allow selective processing of one block relative to the other [97]. Therefore, one block in a blended film can be chosen for specific application [98, 99]. For example, in PS (Polystryrene)-b-PMMA (Poly methyl methacrylate) diblock copolymer system, the blend can self-assemble into structure of hexagonally arranged PMMA cylinders in PS matrix on a substrate as shown in Fig. 1.11(a). The diameter of the cylinders (D) and the center to center distance between neighboring cylinders (L) depend on the molecular weight of block copolymers (M) which is given by the following scaling law [100]:

$$D, L \propto M^{\frac{2}{3}} \tag{1.21}$$

Therefore variations in both D and L can be achieved by adjusting the molecular weight of the block copolymers. As the morphology is subjected to the UV light, PMMA degrades whereas PS gets cross linked. And by acetic acid cleaning, the hydrophilic

PMMA comes off from the substrate while the hydrophobic PS stays and finally forms nanopatterned template for further applications [100-102].

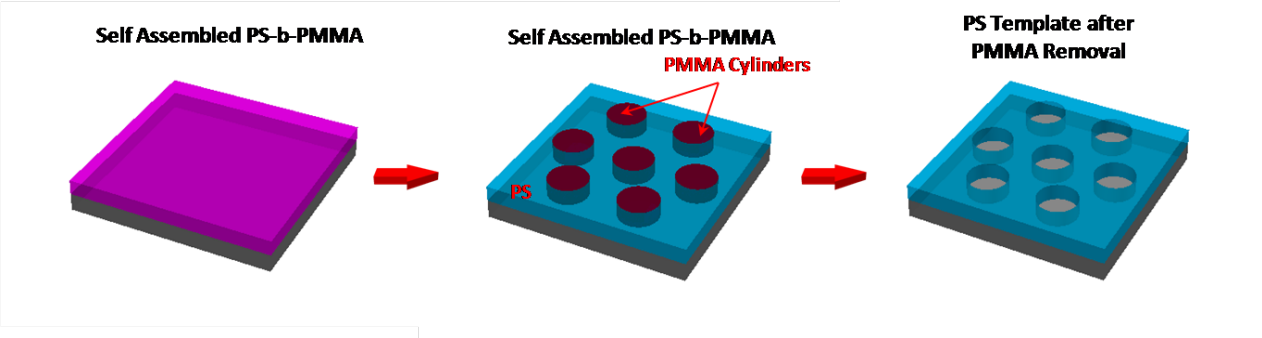


**Figure 1.11 Steps for forming nanoporous template on a substrate via diblock copolymer (PS - b - PMMA) self - assembly and selective processing.**

Diblock copolymer self-assembly has been considered new route to obtain nanoscale periodic patterned template for various applications[103]. Particularly this technique is attractive in the field of semiconductor fabrication due to its potential for replacing conventional lithography process allowing smaller dimensions, less number of process steps and reduced costs[104-108].

# Chapter 2

# Properties of Upgraded Metallurgical Grade Silicon (UMG-Si)

## 2.1 Introduction

Simple p-i-n diodes were fabricated from both upgraded metallurgical grade Si (UMG-Si) and crystalline Si. The behaviors of these diodes at dark and under illumination of 1 Sun were investigated. The results were used as references for further comparison with the solar cells that will be introduced in the later chapters. Also the majority carrier mobility in the UMG-Si was obtained via Hall Effect measurement. The properties of UMG-Si acquired from SIMS analysis and Hall mobility revealed some problems that we need to overcome for utilizing UMG-Si as a solar cell material.

## 2.2 Diminished Performance in UMG-Si based Diode

### 2.2.1 Preparation and Electrical Measurement of UMG-Si based Diode

Generally commercial solar cells have properly textured surface, anti-reflection layer to maximize the light absorption and point contacts on both sides of p and n (top and bottom) to minimize the series resistance in addition to a bulk p-i-n junction. However, the reference cells we introduce in this chapter leave out all those features and are simply composed of bulk p-i-n junction and Al metallization layer. Therefore these

cells are not competing with the commercial Si-based solar cells in terms of the performance. The schematic of the structure of the cells under investigation is shown in Fig. 2.1.

The process of making the UMG Si based p-i-n junction cell starts with polishing both sides of UMG-Si wafer with chemical mechanical polisher (CMP IPEC 472). Then the top and the bottom surfaces were doped with phosphorous and boron respectively using solid state target (PH-1000N, BN-1250, Saint Gobain) diffusing into the wafer at 1000°C under Ar ambient for 15 min (boron) and 20 min (phosphorous) in a tube furnace. Bonding Al wire on the top surface and sputtering Al on the bottom surface of the cell formed the front and back ohmic contacts. The crystalline Si based cell was fabricated in the same manner.

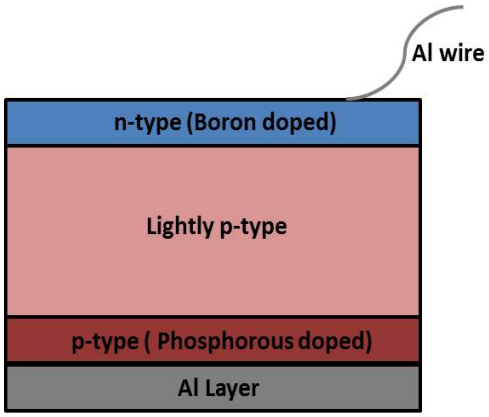


**Figure 2.1 Schematic for the structure of the p-i-n diode (solar cell) generated from both UMG-Si and c-Si for comparison. To form ohmic contacts, Al film was coated on the backside and Al wire was bonded on the front side to simplify the fabrication process.**

I-V measurements of the diodes both at dark and under illumination of full spectrum of 1000W/$m^2$ (1 sun) at room temperature were conducted using a d. c. source meter (Keithley) operated by a custom written LabVIEW and a solar simulator (Newport). The input power of light from the solar simulator was calibrated by a

broadband detector (Newport) at the point where the sample's top surface was placed to confirm the 1 sun illumination. I-V scan under dark and illumination were conducted between -0.8 V and +0.8 V with 0.01 V increment. The current density was calculated by dividing the output current by the area of the cell that was measured. The schematic of the set up for testing the solar cell is depicted in Fig. 2.2.

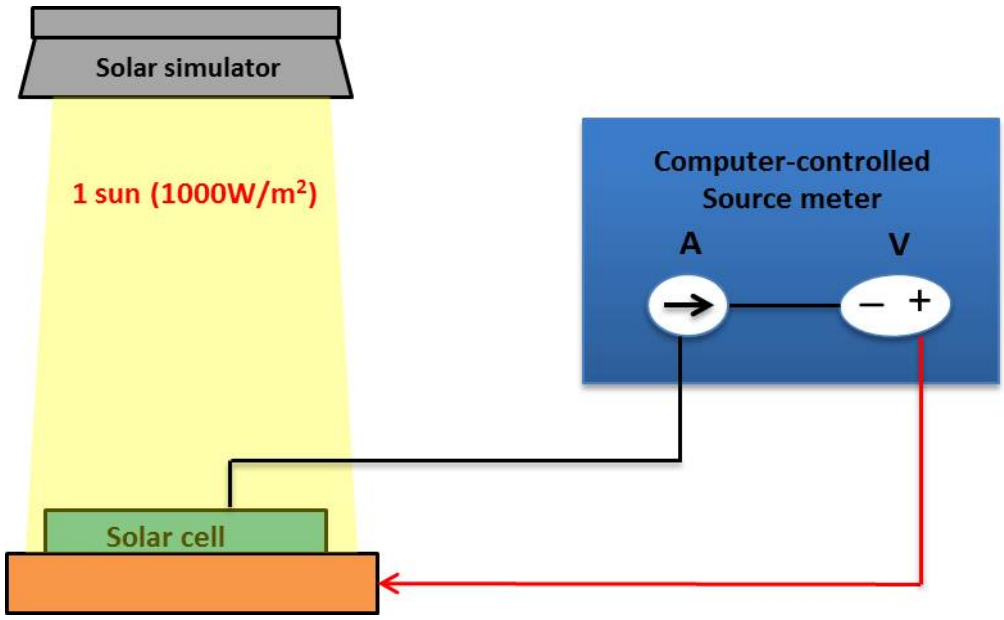


**Figure 2.2 Schematic illustration of a simple I-V tester. The solar simulator provides light intensity of 1000W/m$^2$ under AM 1.5 condition.**

## 2.2.2 Performance of UMG-Si based Diode

Fig. 2.3 (a) shows the semi log J-V plots of UMG-Si based and crystalline Si based cells at dark. Since both cells had Al wire bonded to the front surface for ohmic contacts instead of having electrodes directly onto the surface, both cells suffer power loss from series resistances as the magnitude of diode ideality factor from both cells exceed 2. The diode ideality factor of crystalline Si based cell is 2.2 while that of UMG-

Si based cell is 2.8. These values show that more recombination can occur in UMG Si cell under illumination.

The J-V curves of the cells under illumination are shown in Fig. 2.3 (b) and their characteristics are in Table 2-1. Although the cells had same structure, due to the material properties, UMG-Si based cell exhibits much diminished performance compared to the crystalline Si based cell. The energy conversion efficiency of the UMG-Si based cell is almost half of the efficiency of the crystalline Si based cell showing 3.77%.

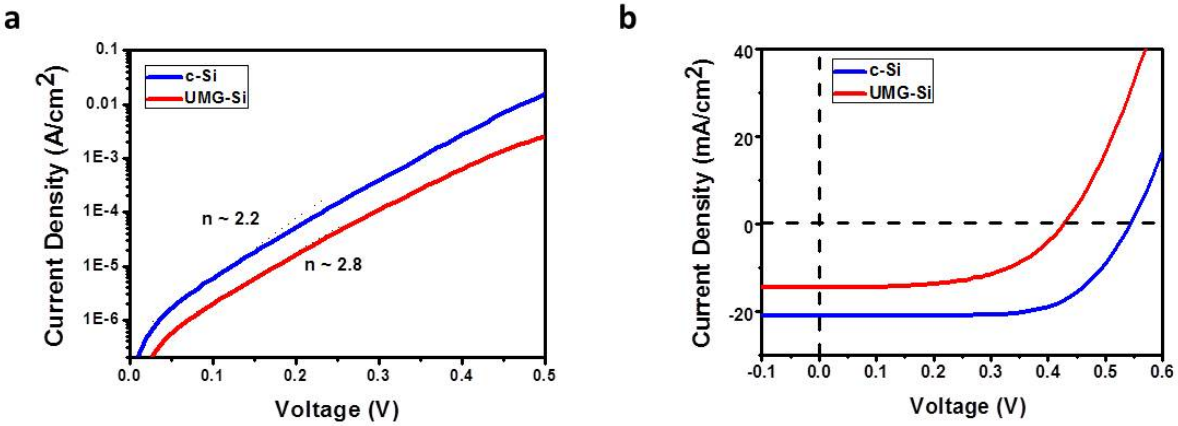


**Figure 2.3 Representative J-V curves for bulk UMG-Si based cell (blue) and crystalline Si based cell (red) under (a) dark condition and under (b) illumination of simulated AM 1.5, full spectrum of 1000W/m$^2$.**

**Table 2-1 J-V characteristics of UMG-Si based cell and crystalline Si based cell.**

| **Materials** | **$J_{SC}$ (mA/cm$^2$)** | **$V_{OC}$(V)** | **FF** | **η (%)** |
|---|---|---|---|---|
| c-Si | 21.08 | 0.53 | 0.66 | 7.37 |
| UMG-Si | 14.63 | 0.47 | 0.77 | 3.77 |

## 2.3 Majority Carrier Mobility in UMG-Si

Mobility is a principal parameter in characterizing electron and hole transport due to drift. Mobility of majority carriers in semiconductor can be measured by using Hall Effect and the acquired mobility from this method is called "Hall mobility ($\mu_H$)". Hall Effect is due to the nature of carriers in conductors. When we consider a semiconductor in the presence of magnetic field and supplied with d.c. current in perpendicular direction from the direction of the magnetic field, the electrons shown as in Fig. 2.4 (a), the semiconductor material experiences force called Lorentz force. Because of this force, the electrons in the material are deflected upwards as illustrated in the Fig. 2.4 (a). As a consequence, electrons and holes accumulate on the opposite side of the subjected material. The separation of charge establishes an electric field which prevents further migration of the charges, and so a steady state voltage across the material develops as long as the current is supplied.

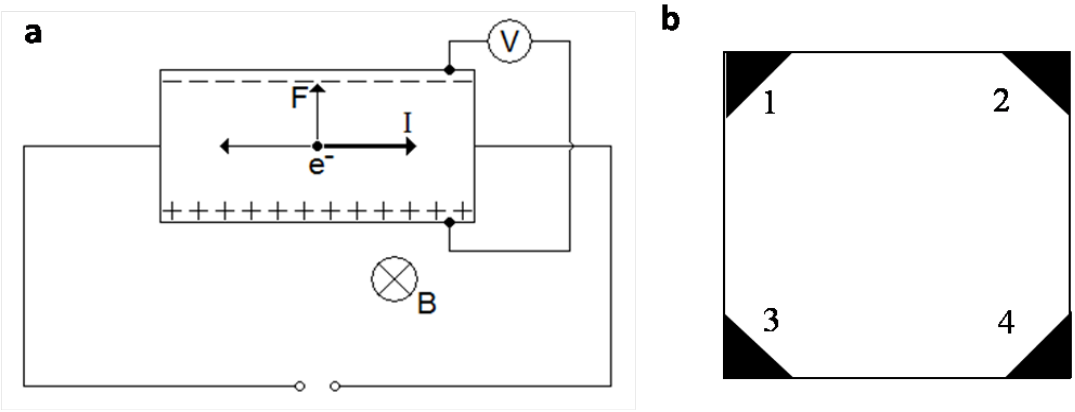


**Figure 2.4 (a) Schematic representation of the measurement of the Hall Effect. (b) A simple Van der Pauw test structure used to measure the resistance and mobility of a conductor.**

By measuring the developed voltage which is called Hall voltage ($V_H$), sheet carrier density and the mobility of majority carriers in the semiconductor can be calculated from the flowing equations.

$$n_s = \frac{IB}{q\,|V_H|} \tag{2.1}$$

$$\mu = \frac{|V_H|}{R_s IB} \tag{2.2}$$

where $n_s$ is sheet carrier density (= n×d) and $R_s$ is the sheet resistance ( = r/d) of the measured semiconductor. For convenience in preparing for the sample, Van der Pauw method was used to obtain Hall coefficients. A common geometry for this measurement has four electrical contacts at the four corners of a roughly square sample as shown in Fig. 2.3 (b). A current is injected through one pair of the contacts, and the voltage is measured across another pair of contacts. Two of these measurements can be related by equations below which is also known as Van der Pauw equation.

$$e^{-\frac{\pi R_A}{R_s}} + e^{-\frac{\pi R_B}{R_s}} = 1 \tag{2.3}$$

where $R_A = \frac{V_{43}}{I_{12}}$ and $R_B = \frac{V_{14}}{I_{23}}$ respectively [109]. For the measurement of UMG-Si, the sample was cut into a square and the four corners were doped with boron to create ohmic contacts for electrical tests. The parameters in this experiment are given as below.

- Temperature : 300K
- B = 1240 Gauss
- Supplied current (I) = 1mA
- Sample thickness (Z) = 1.72 ×$10^{-2}$ cm

The results of the resistivity measurement and Hall measurements are shown in Table 2-2 and Table 2-3 respectively.

**Table 2-2 Measured voltage across the four pairs of corners when 1mA was supplied to the opposite corners.**

| | | $I_{24}$ | | $I_{34}$ | | $I_{12}$ | | $I_{13}$ |
|---|---|---|---|---|---|---|---|---|
| V (mV) | $V_{13\_avg}$ | 22.2985 | $V_{12\_avg}$ | 0.23835 | $V_{34\_avg}$ | 0.2382 | $V_{24\_avg}$ | 22.30085 |

**Table 2-3 Measured voltage across the two pairs of corners when 1240 Gauss was present in opposite directions and 1mA was supplied to $I_{23}$ and $I_{14}$.**

| | B=+ | $I_{23}$ | B =- | $I_{23}$ | B=+ | $I_{14}$ | B=- | $I_{14}$ |
|---|---|---|---|---|---|---|---|---|
| I= + | $V_{14}$ | 22.0379 | $V_{14}$ | 22.1048 | $V_{23}$ | 22.1 | $V_{23}$ | 22.0383 |
| I = - | $V_{14}$ | -22.036 | $V_{14}$ | -22.1027 | $V_{23}$ | -22.0995 | $V_{23}$ | -22.0383 |
| V (mV) | | $V_{14\_avg}$ | 0.0334 | | | $V_{23\_avg}$ | 0.03095 | |
| | $V_a$ | -0.0669 | $V_b$ | 0.0667 | $V_c$ | 0.0617 | $V_d$ | -0.0621 |

The resistivity of the UMG-Si wafer calculated from equation (2.4) by substituting measured results in Table 2-2 is 0.8683Ω-cm.

$$\rho = \left(\frac{Z\pi}{\ln 2}\right)\left(\frac{V_{13} + V_{12} + V_{34} + V_{24}}{4I}\right) = 0.8683\ \Omega - \text{cm} \tag{2.4}$$

The carrier type was found p–type. The carrier concentration and the mobility were calculated from the below equations by substituting the results in Table 2-3.

$$n = \frac{2 \times 10^{-8} IB}{\frac{1}{4}(|V_a| + |V_b| + |V_c| + |V_d|)} = 1.42 \times 10^{17}\ /\text{cm}^3 \tag{2.5}$$

$$\mu = \frac{1}{ne\rho} = 50.80\ \text{cm}^2/\text{V} \cdot \text{s} \tag{2.6}$$

The obtained majority carrier (hole) concentration of UMG-Si is $1.42\times10^{17}/cm^3$ and their average mobility is 50.80 $cm^2/V\cdot s$. In semiconductor, mobility is a measure of ease of carrier motion in a crystal. Therefore increase in the motion-impeding collisions within a crystal due to the presence of high level of impurity and defects leads to decrease in the mobility of carriers [39]. The general hole mobility of p-type crystalline Si wafer is around 400 ~ 500 $cm^2/V\cdot s$ as in Table 2.4 [110]. However in UMG-Si, the hole mobility was measured to be much smaller value of ~ 50 $cm^2/V\cdot s$ manifesting its poor material quality.

**Table 2-4 Comparison of physical properties of crystalline Si and upgraded metallurgical grade (UMG) Si, where n is the carrier concentration (hole) and μ is the mobility (hole). The crystalline Si data was taken from previous work [107].**

| Materials | type | ρ (Ω-cm) | n ($cm^{-3}$) | μ ($cm^2/V\cdot s$) |
|---|---|---|---|---|
| c-Si* | p | 1 | 1.46e16 | 428.08 |
| UMG-Si | p | 0.868 | 1.42e17 | 50.80 |

## 2.4 Conclusion

The examinations of the properties of the UMG-Si and the comparisons with those of crystalline Si were carried out. By evaluation of the diode behavior of UMG-Si based cells both under dark and light conditions and comparing with the crystalline Si based cell, higher deviation from the ideal diode characteristic and diminished photon energy conversion were measured from the UMG-Si based cells.

The Hall Effect measurement of the UMG –Si allowed getting the value of majority carrier mobility. The hole mobility in the UMG-Si was measured almost 8 times

smaller than the hole mobility in normal p-type crystalline Si due to higher frequency of scattering in the material resulting from impurities and defects.

From the mobility examination and the purity level analysis (SIMS, 5N), it becomes obvious that the minority carrier diffusion length in the UMG-Si is much smaller than that of crystalline Si. Despite advantage of low cost, UMG-Si is in fact not a good candidate for solar cell material. However, in the next chapters, attempts of enhancing the efficiency of the solar cell generated from UMG-Si will be introduced. The strategies are (1) reducing the physical thickness of the solar cell and (2) incorporating nanoscale features for light trapping.

# Chapter 3

# Ag Nanoparticles (AgNP) and Si Nanopillar Arrays (SiNA) for Light Trapping

## 3.1 Introduction

The solar module introduced in this chapter is based on UMG-Si and is composed of parallel connected, ultrathin ~17μm thick microcell arrays on flexible supporting substrates. The microcell arrays incorporate Ag nanoparticles (AgNP) and Si nanopillar arrays (SiNA) [111], which serve to enhance light absorption and increase cell efficiency [112].

The Ag nanoparticles and the Si nanopillar arrays created on the solar cell's surface can significantly increase the light absorption by one or more of the following mechanisms: (1) LSPR at the vicinity of the metallic nanoparticles' surfaces [50-53], (2) scattering of incident light at oblique angles thereby elongating the optical path-length [113, 114], (3) substrate-coupled Mie resonances [115], and (4) impedance matching caused by a tapered refractive index [114].

In this chapter, methodology of creating Ag nanoparticles and Si nanopilllar arrays which served as field enhanceing and light scattering layer, and finally integrating these structures to the solar microcell module is demonstrated. The changes in the

electrical and optical properties in the microcells caused by the presence of the nanostructures are also discussed.

## 3.2 Fabrication of Ag Nanoparticles and Si Nanopillar Arrays

The schematic of producing Ag nanoparticles and Si nanopillar arrays on Si substrate is depicted in Fig. 3.1. The preparation of plasmonic Ag nanoparticles and Si nanopillar arrays were performed through block copolymer lithography on Si, Ag deposition and lift-off, followed by reactive ion etching (RIE). As discussed in chap. 1.5, block copolymers are self-assembling polymeric materials that provide a variety of periodic nanoscale morphologies having feature\e sizes ranging from 5nm to 50nm. Unlike other nanopatterning techniques such as focused E-beam lithography [116] or nanoimprint lithography [117], block copolymer self-assembly provides a high throughput patterning process, thereby enabling ease of scalability[97, 100, 101, 103, 111, 118, 119]. Here, for the block copolymer lithography process, polystyrene-block-poly methyl methacrylate (PS-b-PMMA) block copolymers were chosen and the self-assembly yielded perpendicular domains of PMMA cylinders in PS matrix [100-102].

The process starts with having the Si surface exposed to UV light which results in formation of OH group on the Si surface followed by neutrally treating the microcells with a random copolymer brush. A thin film (thickness: 100 nm) of asymmetric block copolymers, polystyrene-block-poly(methyl methacylate)s (PS-b-PMMAs) forming cylindrical nanostructures (molecular weight: PS/PMMA-140k/60k, PMMA cylinder diameter: 34 nm, center to center distance between neighboring cylinders: 64 nm &

molecular weight: PS/PMMA-46k/21k, PMMA cylinder diameter: 18 nm, center to center distance between neighboring cylinders: 34 nm) were spin-coated onto the surface of the module. After high temperature annealing at 190 °C, the substrates were irradiated with UV and subsequently rinsed with acetic acid and water to remove PMMA cylinder cores and crosslink the PS matrix. The substrate was further treated in oxygen plasma for 10s for the purpose of removing the remnant cylinder cores. The Ag thin film (5-30 nm) was deposited over the PS template. After the deposition process, the remaining PS nanoporous template was lifted-off by sonicating in toluene. Through this procedure, Ag nanoparticles having uniform size and arrayed following the hexagonal lattice of the nanotemplates were formed on the Si surface. Using the remaining Ag nanoparticles as an etching mask, the Si layer was etched by RIE (LAM 9400) to produce s dense Si nanopillar structure. The Si nanopillars formed still have Ag nanoparticles sitting on the top end.

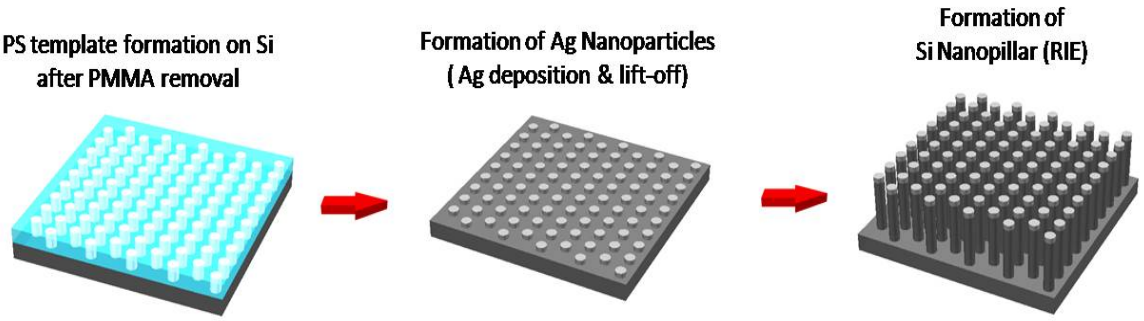


**Figure 3.1 Schematic illustration of creating Ag nanoparticles and Ag nanoparticle/Si nanopillar Arrays on Si substrate employing block copolymer lithography.**

The UMG-Si solar cell now has the structure of Ag nanoparicle/Si nanopillar arrays on the surface. The diameters of the Ag nanoparticles were either 18 nm or 34 nm, depending on the molecular weight. The SEM image of Ag nanoparticles with 18 nm and

34 nm-diameters on Si are shown in Fig. 3.2 (a) and (b). In Fig 3.2 (a), defects of the pattern along domain boundaries are observed. Inside each domain, the pattern shows almost perfect periodicity as shown in the inset of Fig. 3.2 (a).

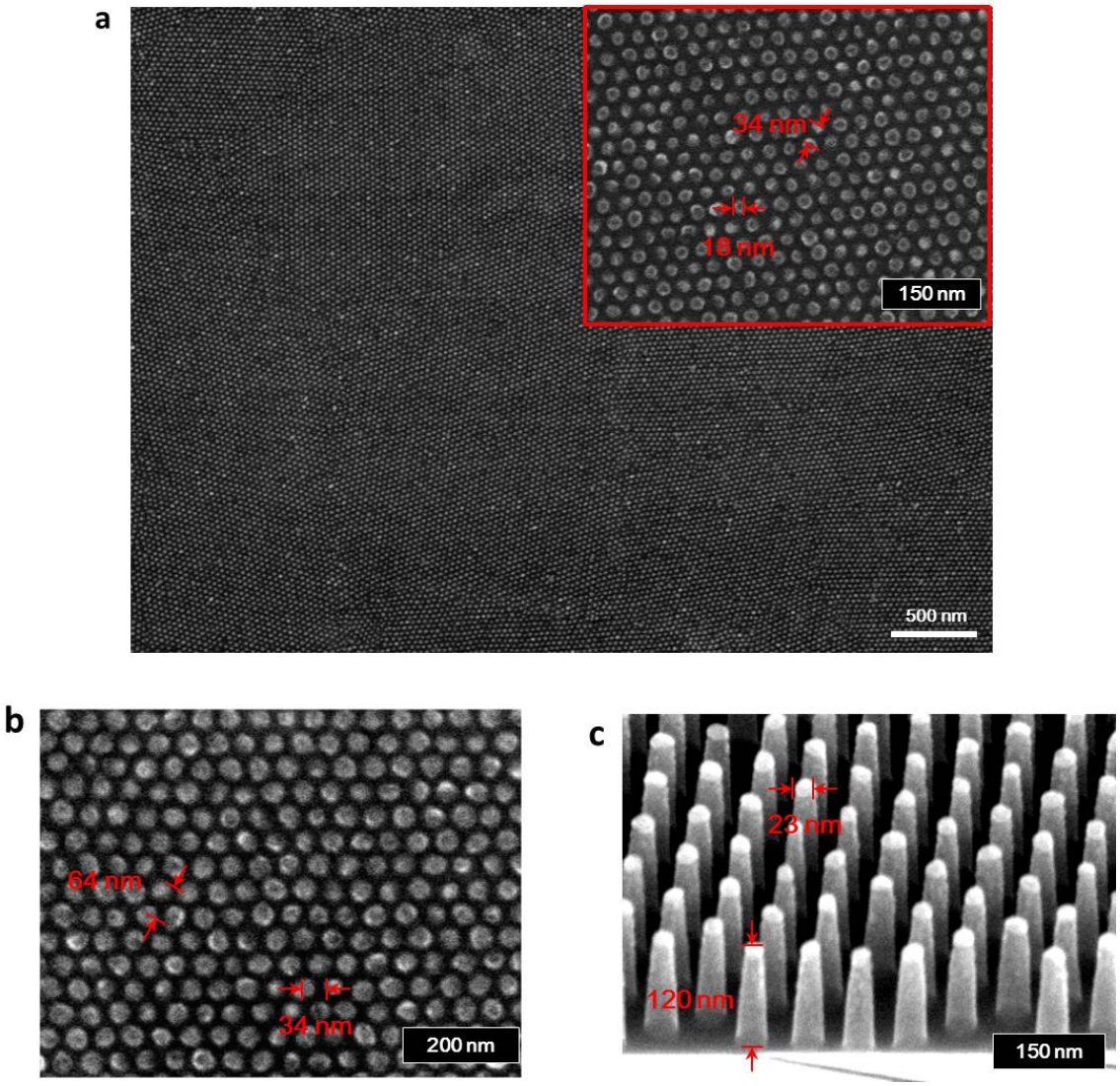


**Figure 3.2 SEM images of (a and b) Ag nanoparticles (D = 18 nm, D = 34nm, t = 30 nm) prepared by block copolymer lithography on top of Si surface. The Ag fill fraction of 18 nm size nanoparticles is 24.4% and that of 34 nm size nanoparticles is 24.6%. (c) Tilted SEM image of Ag nanoparticle/Si nanopillar arrays prepared by reactive ion etching (RIE). The prepared Ag nanoparticles (D = 34 nm, t = 30 nm) were used as a mask for Si etching.**

After formation of the nanopillars via RIE, the diameter of nanoparticles sitting on the nanopillars decreased slightly (to ~23nm) and this can be confirmed from the SEM image of Ag nanoparticle/Si nanopillar arrays shown in Fig. 3.2 (c). The height of the Si nanopillars was approximately 120 nm and the sidewalls of the prepared nanopillars were slightly tapered due to the RIE process.

## 3.3 Evaluation of Optical and Electrical Enhancements

### 3.3.1 External Quantum Efficiency (EQE) Measurements

Quantum efficiency measurements were obtained with an Oriel 150 W Xe arc lamp (Newport) and a quarter-turn single-grating monochromator (Newport). Sample measurements were recorded with chopped illumination (15 Hz), and a quartz beam splitter was used to simultaneously record the light output intensity with a separate Si photodiode (Newport) to adjust for fluctuations in lamp intensity. The potential of the working photoelectrode was set to 0 V relative to the solution potential, and the absolute photocurrents were measured by a digital PAR 273 potentiostat. The output current signal was connected to a Stanford Instruments SR830 lock-in amplifier, and the output signals from the lock-in amplifier and the reference Si photo-diode were fed into a computer controlled by custom-written LabVIEW software.

### 3.3.2 Optical Studies of Ag nanoparticles and Si Nanopillars

For a detailed evaluation of the effects of Ag nanoparticles and Si nanopillar arrays, different diameters (18 nm a d 34 nm) of Ag nanoparticles and Ag nanoparticle/Si nanopillar arrays were prepared on 180μm thick bulk UMG-Si solar cells as introduced in

chap 2.2.1. Fig. 3.3 (a) shows the optical images of the five cells that were examined : (1) as-doped UMG-Si, (2) Ag nanoparticles (D, 18 nm; t, 30 nm) on UMG-Si, (3) Ag nanoparticles/ Si nanopillar arrays prepared with 18 nm Ag nanopariticles on UMG-Si, (4) Ag nanoparticles (D, 34 nm; t, 30 nm) on UMG-Si, and (5) Ag nanoparticles/Si nanopillar arrays prepared with 34 nm Ag nanoparticles on UMG-Si. The optical images of the prepared cells clearly show that the color of the cells gets darker with the presence of the Ag nanoparticles and Ag nanoparticles/Si nanopillar arrays and this implies that the reflectance is increasing as the nanostructures are added to the surface. For quantitative analysis, reflectances of these samples were measured between wavelengths of 300 nm – 950 nm. As illustrated in Fig. 3.3 (b) and (c), reflectance comes in two varieties, specular and diffusion. Specular reflectance is generated by a light ray incident on a smooth surface. In this case, the light ray's incidence is equal to the angle of reflection. Diffuse reflectance is generated by a light ray incident on a rough surface. The incident light ray gives rise to multiple reflection angles. Most materials present both specular and diffusion reflectance. Therefore the summation of these two reflectances, which is the total reflectance (total = specular + diffuse), should be obtained for accurate result. The diffusion reflectance and specular reflectance of the five cells are shown in Fig. 3.3 (b) and (c) respectively and the summation of them, which is the total reflectance, is shown in Fig. 3.3 (d).

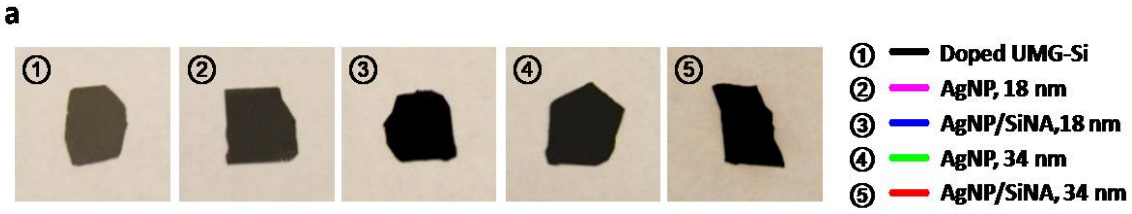

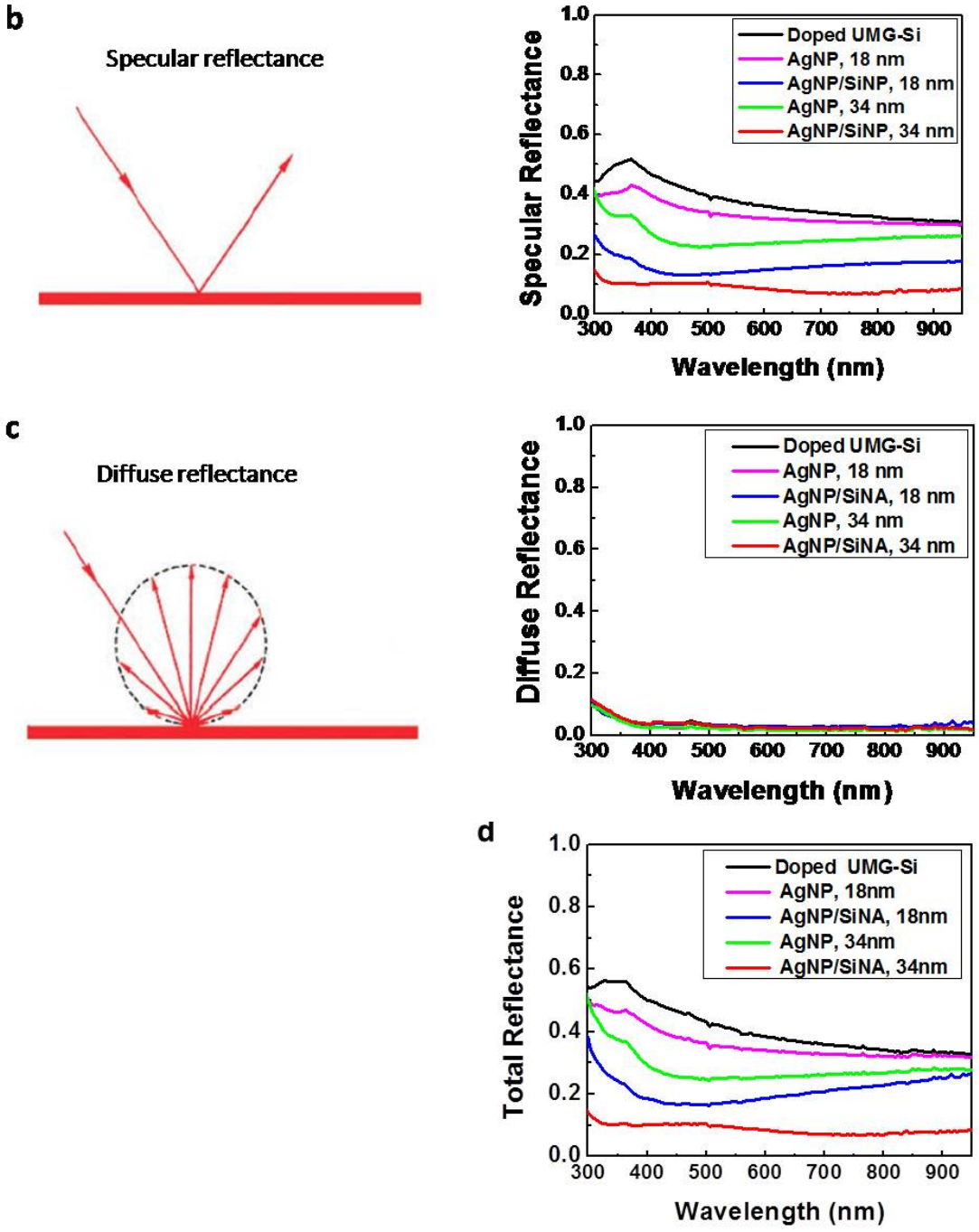


**Figure 3.3 (a) Optical images, (b) diffuse reflectance, (c) specular reflectance and (d) total reflectance curves for the as-doped UMG-Si (black), Ag nanoparticles (D = 18 nm, t = 30 nm) on UMG-Si (magneta), Ag nanoparticle/Si nanopillar arrays prepared with 18 nm Ag nanoparticles on UMG-Si (blue), Ag nanoparticles (D = 34 nm, t = 30nm) on UMG-Si (green), and Ag nanoparticle/Si nanopillar arrays prepared with 34nm Ag nanoparticles on UMG-Si (red).**

The absorbances of the cells were calculated by assuming that the transmittance through 180 μm thick Si for wavelengths shorter than 950 nm is negligible since the thickness was thick enough not to allow the light to transmit. Therefore, the absorbance was obtained by simply subtracting the total reflectance from unity (α (E) = 1 – R (E) – Γ (E), Γ (E) ≈ 0). Fig. 3.4 (a) shows the calculated absorbance curves for the five cells. Both the 18 nm and 34 nm Ag nanoparticles increased absorbance of UMG-Si in the short wavelength region (~ 450 nm) and this is more clearly shown in the plot of absorbance difference with respect to the bare cell in Fig. 3.4 (b). As the size of Ag nanoparticles becomes larger (D = 18 nm → D = 34 nm) absorbance enhancement becomes more pronounced. This trend is consistent with the theoretical predictions regarding plasmonically enhanced scattering of metal nanoparticle discussed in chapter 1.4 [51, 73, 79, 120]. Metal particle with diameter less than 100 nm can meet point dipole prediction. According to the eq. (1.16), the scattering cross section of a single spherical metal nanoparticle is proportional to the volume of the nanoparticle.

$$C_{sca} = \frac{k^4}{6\pi}|\alpha|^2 = \frac{8\pi}{3}k^4a^6\left|\frac{\varepsilon-\varepsilon_m}{\varepsilon+2\varepsilon_m}\right|^2 \quad (1.16)$$

Since Ag nanoparticles on the UMG-Si have diameter of 18 nm and 34 nm, their plasmonic behavior can be described by the point dipole model and Fröhlich condition. The reason for higher absorbing intensity in 34 nm size particle relative to the 18 nm size particle is due to greater extinction cross section in larger particle [68]. According to point dipole prediction, the resonance of an Ag sphere in air occurs at wavelength of 350 ~ 400nm. However our cells exhibit maximum absorption at the wavelength of ~ 450 nm. These shifts can be described by change in the nanoparticles' dielectric environment and

the interparticle coupling [73, 74, 120]. In our cells, the Ag nanoparticles are placed at the interface between Si substrate and air which can enhance scattering into Si and shift the resonance peaks toward the longer wavelength region. Also as discussed in chapter 1.4, additional resonance shift can occur in ensemble of nanoparticles when the interparticle spacing, d is less than 100 nm. The UMG-Si cell that with18 nm size Ag nanoparticles, had interparticle spacing of 18 nm whereas the cell with 34 nm size Ag nanoparticles had interparticle spacing of 30 nm. Since the near-field interaction strength shows $d^{-3}$ dependence, we can infer that strong interparticle interaction took place in our cells and also affected the absorption intensity. Although both cells with 18 nm and 34 nm size nanoparticles have Ag fill fractions between 24 - 25%, due to unique properties of LSPR, variations in size and the spacing of the particles resulted in different optical responses.

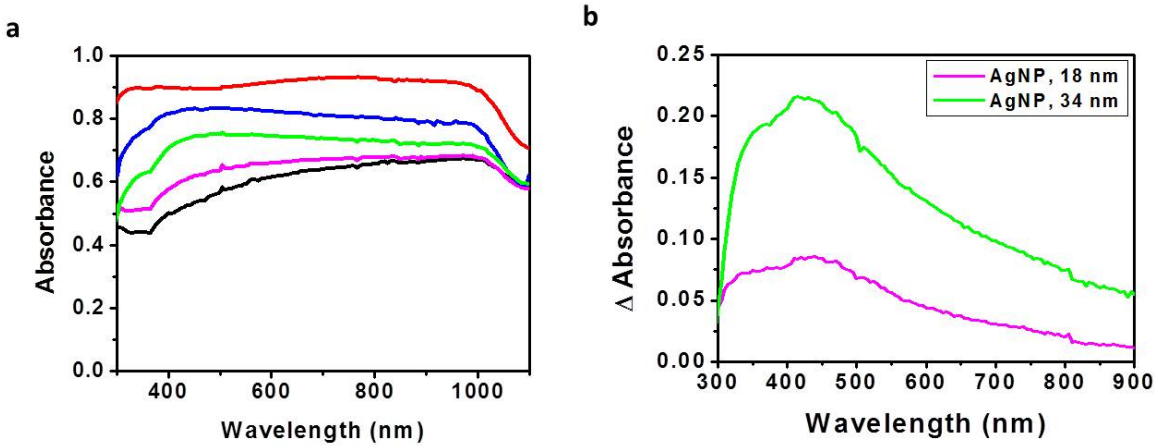


**Figure 3.4 (a) Absorbance spectra of as-doped UMG-Si (black), Ag nanoparticles (D = 18 nm, t = 30 nm) on UMG-Si (magneta), Ag nanoparticle/Si nanopillar arrays prepared with 18 nm Ag nanoparticles on UMG-Si (blue), Ag nanoparticles (D = 34 nm, t = 30 nm) on UMG-Si (green), and Ag nanoparticle/Si nanopillar arrays prepared with 34 nm Ag nanoparticles on UMG-Si (red). (b) Absorbance difference with respect to the bare cell for 18 nm Ag nanoparticles and the 34 nm Ag nanoparticles cells. As the size of Ag nanoparticles increases the absorbance intensity became more pronounced.**

Unlike the LSPR effect, Si nanopillar arrays increase the absorbance across the entire wavelength spectrum. Especially the Ag nanoparticles/ Si nanopillar arrays prepared with 34nm diameter Ag nanoparticles on a UMG-Si cell showed excellent absorbtance of greater than 90% between wavelengths of 300 – 950 nm. This is attributed to the texturing effects caused by forming Si nanopillars on the cell's surface. The nanopillars scatters light within the entire wavelengths of the light and increase their path length in the cell, which leads to enhanced absorption over a broad range of wavelength, from the visible to IR.

### 3.3.3 Electrical Studies of Solar Cells with Ag Nanoparticles and Si Nanopillar Arrays

External quantum efficiency (EQE) measurements of the UMG-Si cells presented in the previous chapter were carried out in the visible and near IR (300 ~ 1100 nm of $\lambda$) and the plotted curves are in Fig. 3.5 (a). The EQE of the five cells showed enhancements in similar fashion as the absorbance enhancements. For example, at a wavelength ~ 700 nm, the bare doped UMG-Si cells exhibits ~ 42% quantum efficiency, whereas the EQE of the Ag nanoparticle/Si nanopillar arrays cell prepared with 34nm Ag nanoparticles reaches ~ 81%. The enhanced EQE in cells with larger Ag nanoparticles and with both Ag nanoparticle and Si nanopillar arrays is due to enhanced absorption as the EQE is proportional to the absorbance.

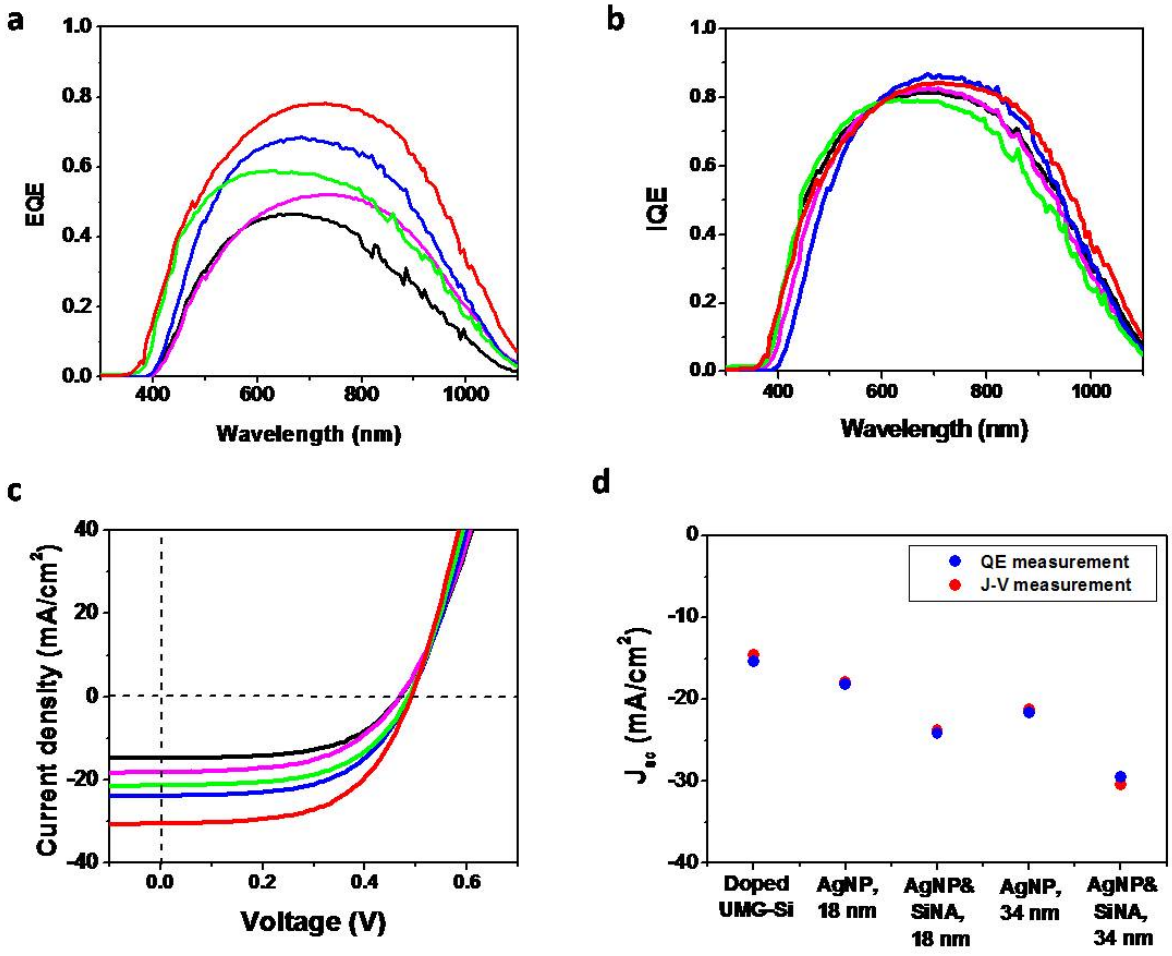


**Figure 3.5 (a) External quantum efficiency, (b) internal quantum efficiency, and (c) J-V curves of the as doped UMG-Si (black), Ag nanoparticles (D = 18 nm, t = 30 nm) on UMG-Si (magenta), Ag nanoparticles/Si nanopillar arrays prepared with 18nm Ag nanoparticles on UMG-Si (blue), Ag nanoparticles (D = 34 nm, t = 30 nm) on UMG-Si (green), and Ag nanoparticles/Si nanopillar arrays prepared with 34 nm Ag nanoparticles on 180 μm thick UMG-Si (red). (d) Comparison of $J_{SC}$ acquired from quantum efficiency measurement and J-V measurement.**

The general trend shown in EQE plots is that EQE approaches to 0 both at short wavelength regions (350 ~ 400 nm) and at long wavelength regions (~ 1100 nm) even though the absorbance spectra shows that the cell is absorbing light throughout the entire spectrum. The absorption loss shown here is due to the intrinsic nature of Si. Light with

short wavelength is normally absorbed at the front surface of the Si where the recombination occurs most frequently due to the dangling bonds of Si. On the other hand, light with long wavelength is absorbed at the rear surface of the Si and therefore suffers from rear surface recombination. Also carriers created near the rear of the solar cells mostly fails to traverse the thickness of the cell when the material has short diffusion length. These trends are often showed in Si-based solar cells.

Since external quantum efficiency and the absorbance of the five cells were obtained, internal quantum efficiency that excludes the absorption contribution in the external quantum efficiency quantity was achieved. The internal quantum efficiency curves are plotted in Fig. 3.5 (b). The five curves are showing little variations as the cells are based on the same material (UMG-Si) and doped under the same condition. This clarifies that the probability of delivering photogenerated carrier to the outer circuit from absorbed photon is similar in all five cells.

**Table 3-1 J-V characteristics of doped UMG-Si, Ag nanoparticles (18 nm) on UMG-Si, Ag nanoparticle/Si nanopillar arrays prepared with 18 nm Ag nanoparticles on UMG-Si, Ag nanoparticles (34 nm) on UMG-Si, and Ag nanoparticle/Si nanopillar arrays prepared with 34 nm Ag nanoparticles.**

| Cells | $J_{SC}$ (mA/cm$^2$) | $V_{OC}$(V) | FF | η (%) |
|---|---|---|---|---|
| Doped UMG-Si | 14.63 | 0.47 | 0.55 | 3.78 |
| AgNP, 18 nm | 17.94 | 0.47 | 0.55 | 4.64 |
| AgNP/SiNA, 18 nm | 23.79 | 0.49 | 0.55 | 6.41 |
| AgNP, 34 nm | 21.28 | 0.49 | 0.54 | 5.63 |
| AgNP/SiNA, 34 nm | 29.98 | 0.49 | 0.55 | 8.08 |

The J-V curves of the cells under illumination of 1 sun are shown in Fig. 3.5 (c) and the detailed characteristics are in Table 3-1. The cells with larger EQE yield greater $J_{sc}$ and increasing efficiencies of the cells are concomitant with this. $V_{oc}$ (~ 0.48V) and FF (~ 0.55) is similar for all of the cells. $J_{sc}$ can be calculated from the EQE with using eq. (1.6), which is

$$J_{SC} = q \int_0^{\infty} EQE\,(E) b_S(E) dE \qquad (1.6)$$

where $b_S(E)$ is the photon flux density of the solar spectrum at AM 1.5 and 1 sun. The calculated $J_{SC}$ by substituting the EQE measurement results and the AM 1.5 solar spectrum (downloaded from NREL) to the above equation, shows good agreement with the experimentally derived $J_{sc}$ from J-V measurement. The comparisons are plotted in Fig. 3.5 (d). The good agreement between the calculated value and experimentally obtained values of $J_{sc}$ clearly shows that the solar simulator (Newport) used for cell testing is providing illuminating condition that is almost same as standard 1 sun condition. The $J_{SC}$ data showed that the structure of Ag nanoparticle/Si nanopillar array prepared from 34 nm Ag nanoparticles increased $J_{SC}$ of UMG-Si cell from 14.63 to 29.98 $mA/cm^2$ and $\eta$ from 3.78 to 8.08%. This is enhancement greater than 100%. So far, from various analyses, it has been clarified that optimized surface design for maximum light absorption among the evaluated UMG-Si based cells is the Ag nanoparticle/Si nanopillar arrays generated from 34 nm size Ag nanoparticles.

### 3.3.4 Analysis of Individual Effects of Ag Nanoparticles and Si Nanopillar Arrays

From previous chapters, the structure of Ag Nanoparticle/Si nanopillar arrays was found to be more effective for the light absorption than the structure of Ag nanoparticles alone. However, apart from the surface structure that contains both Ag nanoparticles and Si nanopillars, the sole effect of Si nanopillars on UMG-Si has not been clarified yet. In order to identify the individual contributions of Ag nanoparicles and Si nanopillars on the UMG-Si cell's efficiency, UMG-Si cell with Si nanopillar only was examined. The cell was prepared by acid etching the UMG-Si cell with Ag nanoparticle/Si nanopillar arrays (cell 5 from chapter 3.3.2) so that the Ag nanoparticles can be removed. Energy dispersive spectroscopy (EDS) analysis was carried out before and after the process of Ag nanoparticle removal to ensure Ag content. The EDS result is shown in Fig. 3.6 (a). J-V measurements of the cell with Ag nanoparticle/Si nanopillar array and the cell with Si nanopillars under illumination were carried out and the details are in Fig. 3.6 (b), (c) and Table 3-2. After removing the Ag nanoparticles and leaving Si nanopillars only, the cell's efficiency dropped by 0.9%.

Through this investigation, we estimate that Ag nanoparticles sitting on top of Si nanopillars on cell 5 contributed a 0.9% increase in the overall efficiency, while the Si nanopillar arrays contributed a 3.4% increase in the overall efficiency of the solar cells. Although, the Si nanopillars were created by etching into Si from 34nm size Ag nanoparticles the diameter of Ag nanoparticles shrunk down to 23 nm after the process of reactive ion etching. As a result, due to decreased particle volume, the LSPR effect declined compared to the cell with 34 nm size Ag nanoparticles.

To conclude, it became clear that the Si nanopillar arrays are more effective than Ag nanoparticles in improving the absorbance of light on the UMG-Si solar cell.

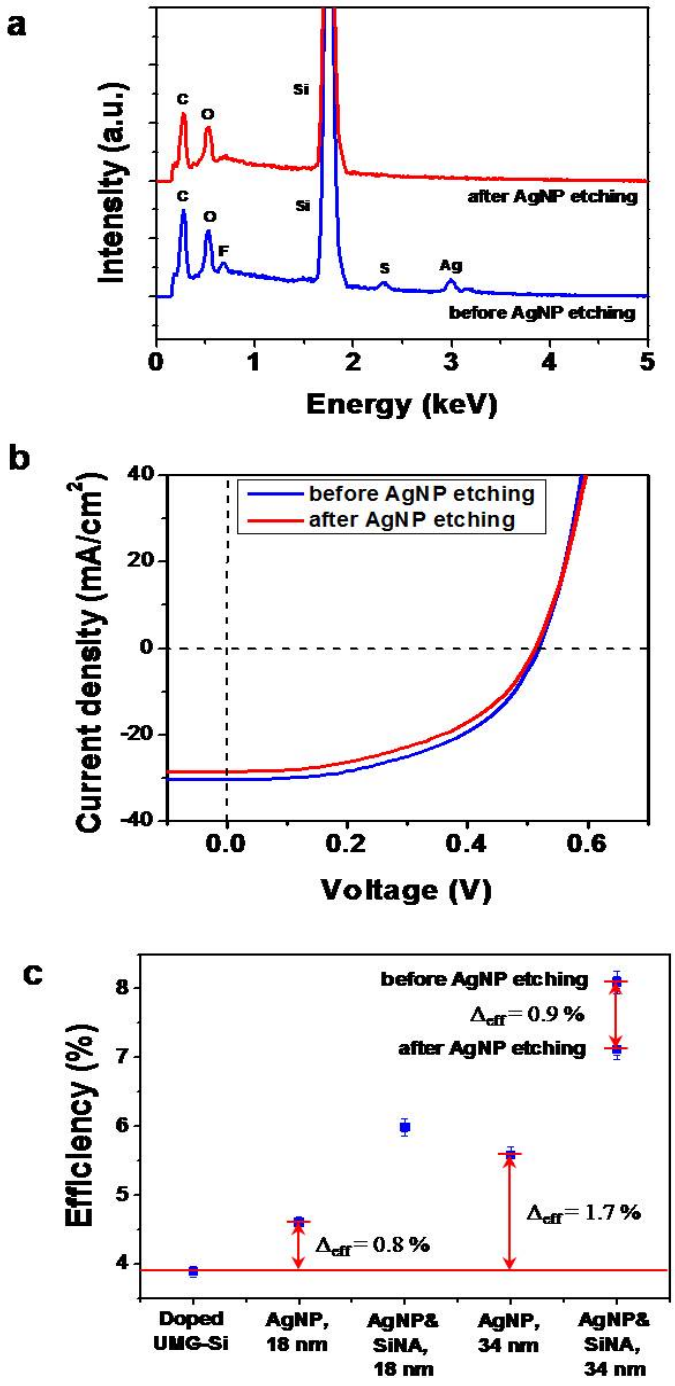


**Figure 3.6 (a) Energy dispersive spectroscopy (EDS) and (b) J-V curves of UMG-Si cells before (blue) and after (red) Ag nanoparticle removal. (c) Efficiency enhancement of UMG-Si cells caused by Ag nanoparticles and Ag nanoparticle/Si nanopillar arrays.**

**Table 3-2 J-V Characteristics of UMG-Si solar cell with Ag nanoparticle/Si nanopillar arrays structure before and after Ag removal.**

| Cells | $J_{SC}$ (mA/cm$^2$) | $V_{OC}$(V) | FF | η (%) |
|---|---|---|---|---|
| Before AgNP etching | 29.98 | 0.49 | 0.55 | 8.08 |
| After AgNP etching | 27.70 | 0.48 | 0.54 | 7.18 |

### 3.3.5 Optical Modeling of Ag Nanoparicles and Si Nanopillar Arrays on Si

To further elucidate the optical effects of Ag nanoparticles and Si nanopillar arrays on the efficiencies of the solar cells, optical modeling of Ag nanoparticles on Si and Ag nanoparticles/Si nanopillar arrays on Si were conducted. The commercial Finite Difference Time Domain (FDTD) method provided from Lumerical was used to carry out the modeling. Generally FDTD simulations are being used to solve Maxwell's equations in complex geometries. Under the simulated light, which is plane source of electromagnetic wave, in the given structure, the power absorption per unit volume ($P_{abs}$) can be calculated from the divergence of the Poynting vector ($\vec{P}$) with the following equation.

$$P_{abs} = -0.5 \text{ real } (\vec{\nabla} \cdot \vec{P}) \quad (3.1)$$

Here, the Poynting vector ($\vec{P}$) represents the directional energy flux density (in W/m$^2$) of an electromagnetic field. It is defined as cross product of electric field and magnetic field.

$$\vec{P} = \vec{E} \times \vec{H} \quad (3.2)$$

By substituting the eq. (3.2) to eq. (3.1), the normalized power absorption ($P_{abs}$) of underlying Si becomes

$$P_{abs}(x, \omega) = -0.5\omega|E(x, \omega)|^2 \mathrm{Im}(\varepsilon_{Si}(\omega)) \quad (3.3)$$

Above equation shows that electric field intensity calculation should be obtained prior to calculating the normalize power absorption in Si. For the simulation of electric field intensity and the power absorption on the surface within the structure, the material properties of Ag was taken from the material database of Johnson and Christy [121], and that of Si was taken from the material database of Palik [122].

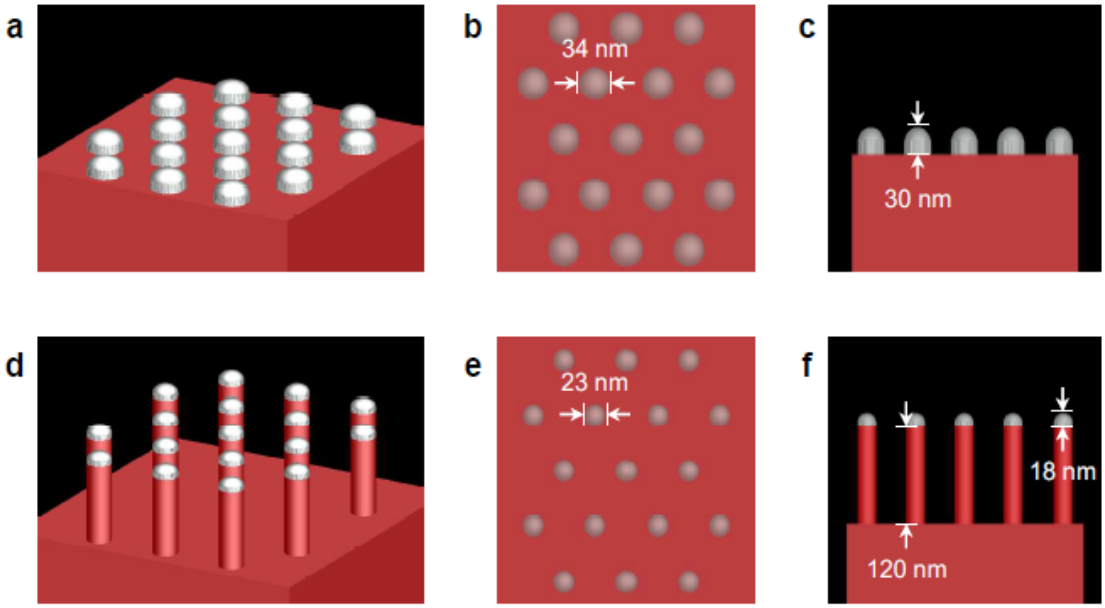


**Figure 3.7 The simulated structures of Ag nanoparticles (a, b, and c) and Ag nanoparticle/Si nanopillar arrays (d, e, and f) on Si substrate. The perspective views (a and d), x-y plane views ( b and e), and x-z plane views (c and f) are also shown. The diameter and height of the Ag nanoparticles (a, b, and c) on the top of Si were 34 nm and 30 nm, while the diameter of Ag nanoparticles on Ag nanoparticles/Si nanopillars (d, e, and f) were 23 nm and 18 nm. The heights of Si nanopillars were 120 nm.**

The dimensions and the layout of the structures were set to be the same with the actual device (diameter = 34 nm, t = 30 nm, h = 120 nm). The dimensions of the rectangular Si substrate were set to be 300 nm by 300 nm with a thickness of 10 μm. The incident light is propagating along z-axis and is polarized along the x-axis. The light source was placed in the center of the structures, 100 nm above the Si substrate, with the wavelength ranging from 400 nm to 1100 nm. Fig. 3.7 shows the simulated structure in the Lumerical.

Fig. 3.8 and Fig. 3.9 shows the calculated electric field intensity maps and normalized power absorption maps under an incident light of wavelength λ =700 nm where the maximum external quantum efficiency was observed, for the x-y plane and x-z plane. The FDTD calculations clearly show light trapping at the interface of the Ag nanoparticles and Si. Perhaps more interestingly, the data also show that the electric field intensity and power absorption significantly increase at the immediate surface of the Si nanopillars in Ag nanoparticles/Si nanopillar array system. The optical modeling results that demonstrate more pronounced light trapping effect in Ag nanoparticle/Si nanopillar array agree with the experimental results as well.

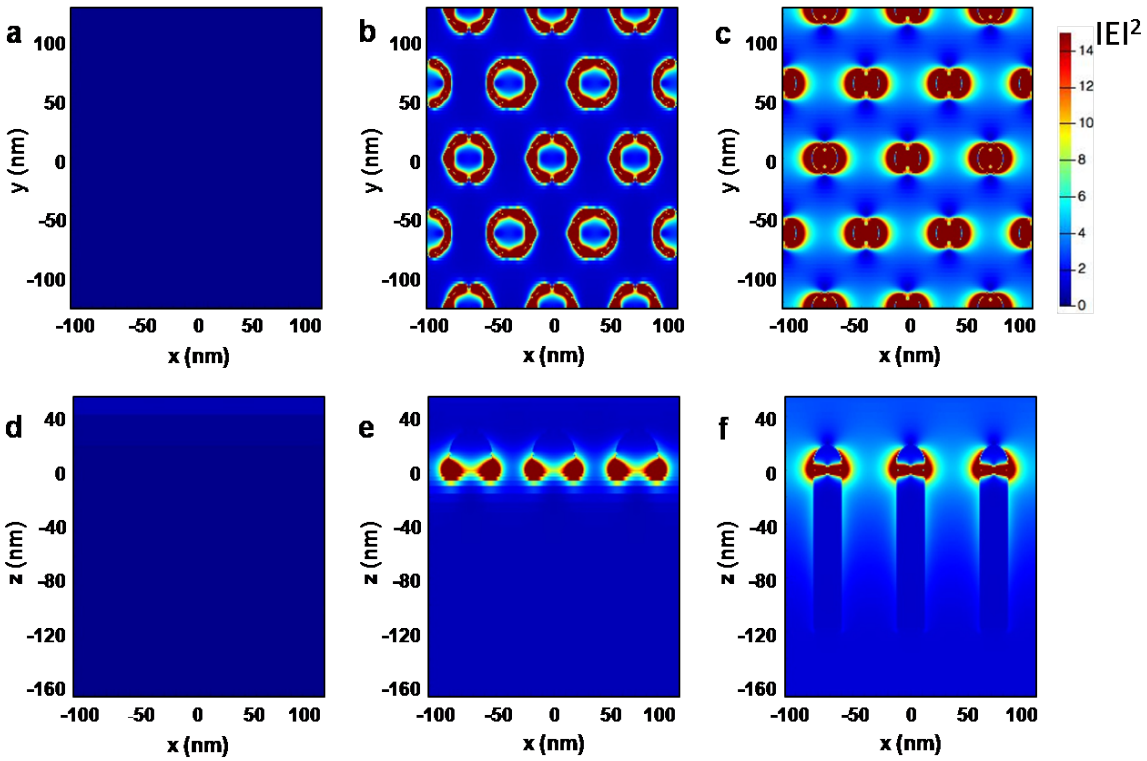


**Figure 3.8 Electrical field intensity maps ($|E|^2$) calculated by FDTD model under an incident light of 700 nm for x-y plane (a, b, and c) and x-z plane (d, e, and f) of bare Si (a, d) and Ag nanoparticles on Si (b, e) and Ag nanoparticle/Si nanopillars on Si (c, f). Note that incident light is propagating along z-axis and is polarized along x-axis.**

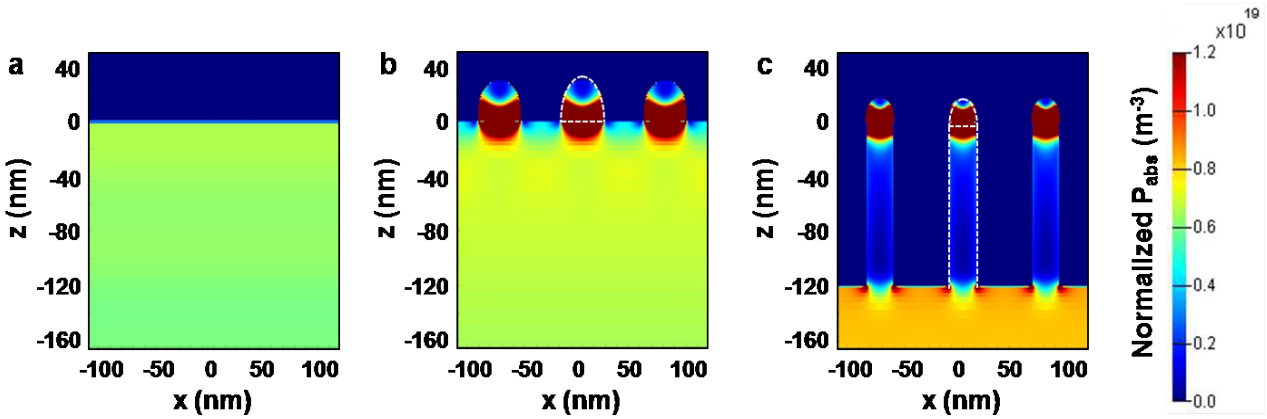


**Figure 3.9 The simulated power absorption per unit volume of (a) bare, (b) Ag nanoparticle, and (c) Ag nanoparticle/ Si nanopillar array on Si under incident light of 700nm for x-z plane. The power absorption calculations show the absorption enhancement effect at the Si substrate in the presence of Ag nanoparticle and Ag nanoparticle/Si nanopillar array structures.**

## 3.4 Solar Microcells from an UMG-Si Wafer

### 3.4.1 Creating Solar Microcells

In chapter 2, the issue of diminished performance of the bulk form of UMG-Si based cell due to the poor material quality was raised. Here, ultrathin (~ 17 μm thick) solar microcells were produced from bulk UMG-Si wafer to reduce the thickness of the cells so that the carrier collection can occur more easily. The schematic of overall process of fabricating the ultrathin solar microcells from the UMG-Si wafer is illustrated in Fig. 3.9. Most of the process steps adapted from the monocrystalline Si microcell process developed by the Roger's research group [123, 124]. The process starts with polishing a p-type UMG-Si wafer in chemical mechanical polisher (CMP IPEC 472). Then, a 3μm thick layer of photoresist (SPR 220-3.0, Shipley) was spin-coated on the wafer and baked for 90s at 115°C. The lateral dimensions (8 μm × 650 μm) and the layout of the microcells were defined by 365 nm UV exposure (Karl Suss MA6 mask aligner) and developing in AZ300 MIF. Next, inductively coupled plasma reactive-ion etching (ICP-DRIE, STS Pegasus) formed ~ 25 μm deep trenches in the exposed regions, and the photoresist was stripped (Baker PRS 2000). The cross-section view of Si trenches formed at this step is shown in Fig. 3.11 (a). For the selective area doping of the microcells, 500 nm of $SiO_2$ deposited with plasma-enhanced chemical vapor (PECVD) deposition at 200°C, was patterned by photolithography, BHF etching, and photoresist stripping, to serve as a doping mask. Solid-state targets of boron (BN-1250, Saint Gobain) and phosphorous (PH-1000N, Saint Gobain) were used as doping sources and were diffused into the wafer at 1000°C under Ar ambient for 15 min (boron) and 20 min (phosphorous)

in a tube furnace. The remaining dopant and oxide film were cleaned in diluted HF solution (HF:$H_2O$ = 1:1) for 1 min. Then layers of $SiO_2$(100 nm)/$Si_3N_4$(300 nm) were coated in PECVD system at 200°C followed by angled deposition of Ni, 30° tilted with respect to the wafer, in an ebeam evaporator to cover the sidewalls and the top surface of the microbars. The wafer was then, etched in ICP-RIE to remove $SiO_2$/$Si_3N_4$ on the surface of the trenches to expose Si that is not covered with Ni. The wafer was diced in the dicing saw (ADT 7100 Dicing saw) and the diced pieces were finally ready for the undercut etching. To obtain the complete undercut, we employed $XeF_2$ (Xactix, 3mT, 40s per cycle, 8cycles) dry etching method, which is independent of the crystal orientation. The top-down view of the microbars tethered to the wafer is shown in Fig. 3.11 (b) and the cross-section views of the partially undercut etched microbars are shown in Fig. 3.11 (c). The $XeF_2$ etching finally provided the freestanding microbars (Fig. 3.11 (d)).The thickness of the freestanding microbars were approximately 20μm. The Ni layer was removed in etching solution ($HCl/H_2O_2/H_2O$=1:1:5). The pieces were again, doped with boron by spin coating spin- on-dopant (Filmtronics) followed by annealing at 1000°C for 1min in rapid thermal annealing to create back-surface field on the bottoms of the cells. Finally $SiO_2$/$Si_3N_4$ layers were removed in HF solution ($HF/H_2O$ =1:1) and the microbars were ready for transferring printing.

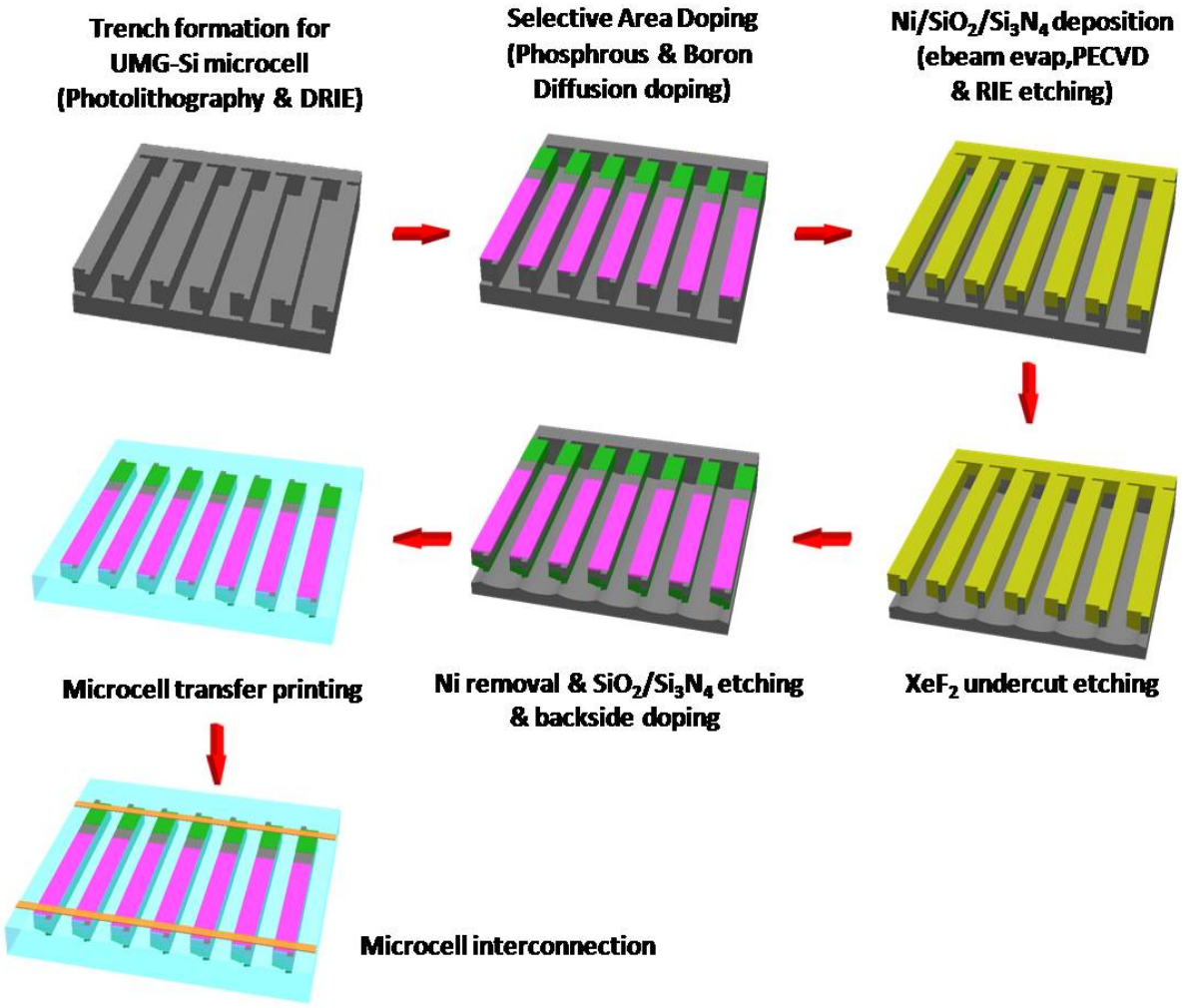


**Figure 3.10 Schematic illustration of the steps of producing of ultrathin UMG-Si solar microcells and the process of integrating them into the completed module.**

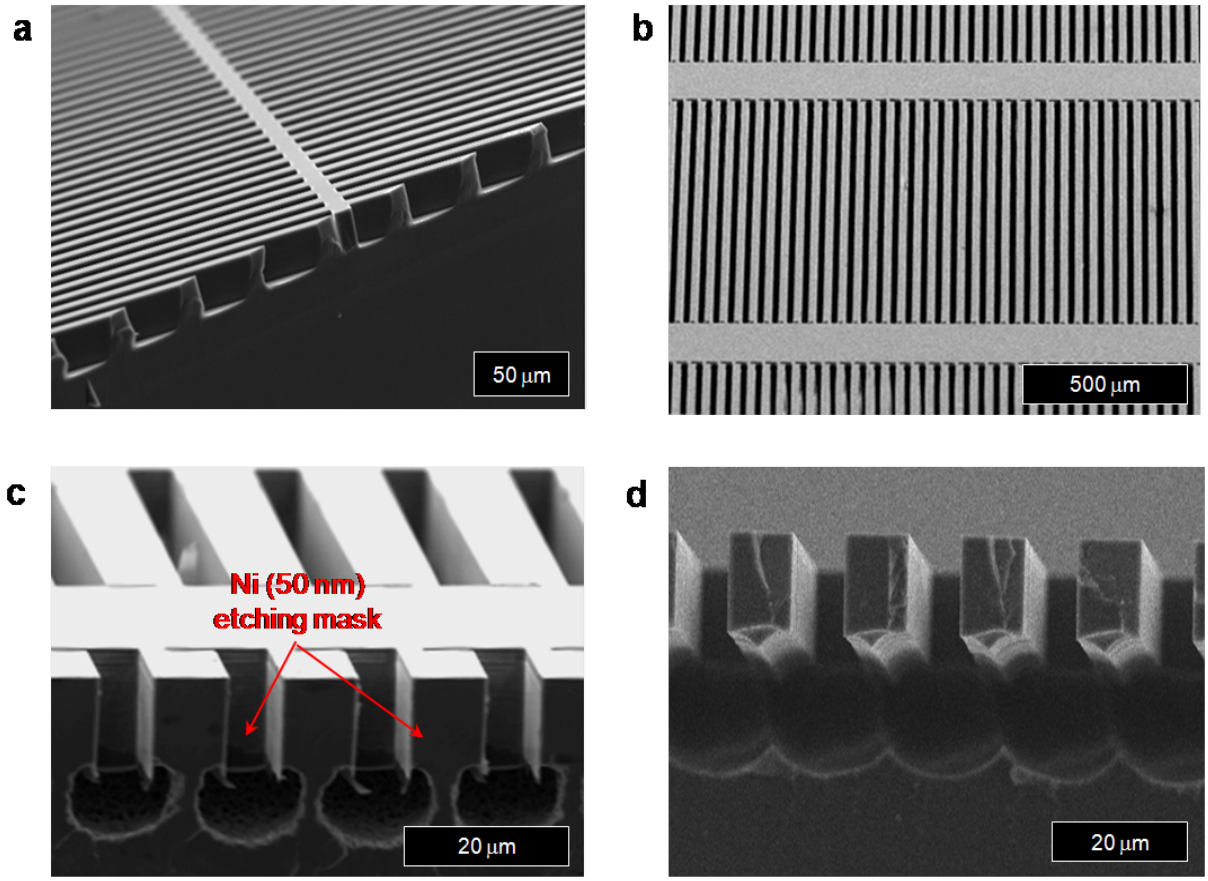


**Figure 3.11 (a) Cross-sectional SEM image of the trenches formed from STS DRIE to create microcells. (b) Top-down and (c) cross-section view of the microcells after subjected to 4 cycles of $XeF_2$ etching. The thin Ni and the $SiO_2/Si_3N_4$ layers underneath, protecting the sidewalls and the top surface of the microcells served as etching mask under $XeF_2$ ambient. (d) The freestanding microcells tethered to the wafer after 8 cycles of $XeF_2$ etching which offered complete undercut.**

### 3.4.2 Transfer Printing and Finishing the Solar Microcell Module

The freestanding microcells got released and transferred on to a polymeric substrate that enables the final module to have properties of flexibility and semitransparency. The process starts with making elastomeric printing stamps which were prepared by mixing PDMS prepolymer and cross-linking agent (Sylgard 184, Dow

Corning Corp.) at the volume ratio of 10:1 and curing at 80°C for 2h. The stamps were placed against the donor pieces and were applied with sufficient stress, then peeled off quickly to release the microcells from the donor substrate and ink them onto the surface of the PDMS stamp. Fig. 3.12 (b) and Fig. 3.12 (c) show the solar microcells tethered to the donor piece ready for retrieval. Receiving substrates were prepared by cleaning a glass slide with UV/$O_3$ for 10 min and spin coating with a photo-curable polymer (NOA61, Norland Products Inc.). The PDMS stamp inked with microcells was placed against this substrate and the whole system was cured in UV light for ~15 min. Then the PDMS stamp was peeled off leaving the microcells embedded in a NOA matrix. Fig. 3.12 (d) shows the aligned microcells printed on the NOA matrix by PDMS stamping. Interconnects on the microcells-inked NOA substrate, were made by Cr/Au (30/400 nm) sputtering followed by spin coating photoresist (AZ 5214, Shipley) for photolithography. The exposed metal layers were removed in Au etchant Type TFA and CR-14 Cr etchant to define the electrodes and the remaining photoresist was stripped in acetone to finish the device. The schematic of the final ultrathin solar microcells is depicted in Fig. 3.12 (a) and the optical image of the device wrapping a glass tube is shown in Fig. 3.12 (e). As shown in Fig. 3.11 (b), each microcell is 9 μm wide, 650 μm long and ~ 17 μm thick. The green colored region and the purple colored region in Fig. 3.12 (a) were doped with boron and phosphorous respectively. The completed microcell module exhibited excellent mechanical flexibility and semitransparency.

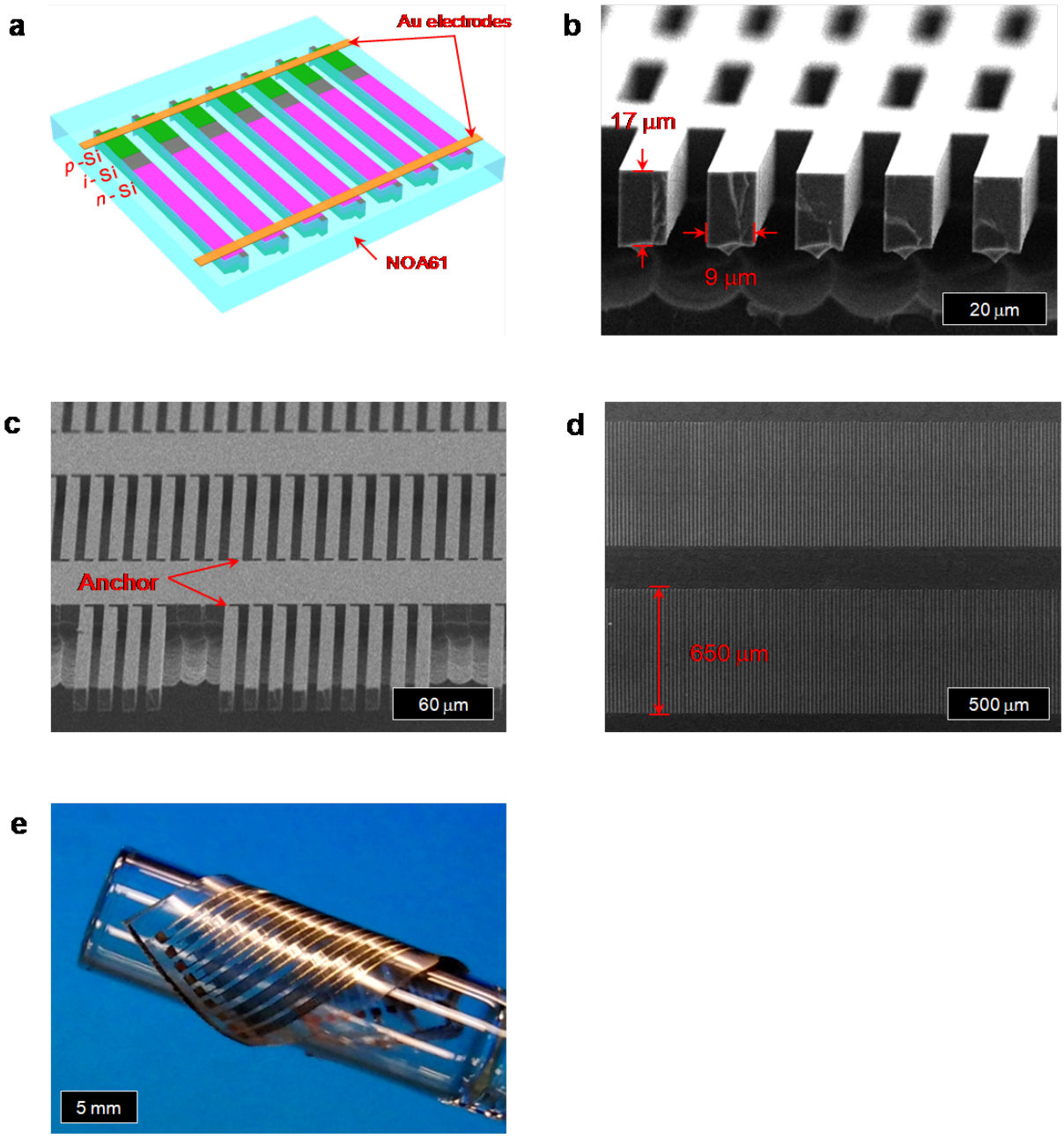


**Figure 3.12 (a) Schematic illustration of the prepared microcell module. (b and c) Tilted SEM images of suspended microcell arrays prepared with isotropic $XeF_2$ etching and supported by two narrow anchors. (d) SEM image of the microcell arrays retrieved from the substrate and transferred on a polymer substrate (NOA 61). (e) An optical image of a complete module consisting of ultrathin microcells interconnected by metal (Cr/Au, 30/400 nm) lines.**

### 3.4.3 Electrical Characteristics of the Solar Microcells

The J-V measurements of the ultrathin microcells both at dark and under illumination of full spectrum of 1000W/$m^2$ at room temperature were carried out. In order to examine the difference in the electrical properties arising from reduction of thickness of solar cells, a 180 μm-thick bulk p-i-n planar junction UMG-Si solar cell that was presented in chapter 2 was used as a reference cell. Fig. 3.13 (a) shows the J-V characteristics of both ultrathin and bulk solar cells under J-V scan between -0.5 V and + 0.7 V in the presence of the light. The detailed parameters of these solar cells are in the Table 3-3. Note that the current density of the microcell module was calculated using the active area of microcells (area of UMG-Si elements) rather than the total surface area.

As discussed in the previous chapter (2.2), the UMG-Si contains high level of impurities (5N) and thus has relatively short minority carrier diffusion length, which plays detrimental role in collections of photogenerated carriers. The ultrathin microcells can bring enhanced carrier collection and make the cell act more like an ideal diode by offering shorter carrier collection pathway from the junction to the electrode. The diode ideality factors (n) of microcell and bulk cell as shown in Fig. 3.12 (b), were obtained from the slopes of the linear regions in the forward bias semilog plots. This value for the 180μm-thick bulk UMG-Si cell is 2.9, whereas that of each microcell is 2.1 The lower value implies improved performance and compares favorably to monocrystalline Si microcells ( n=1.85)[123].

The J-V characteristics under illumination of the two solar cells also manifests that shorter pathway increases the short circuit current density ($J_{SC}$) and efficiency (η). Thinning the thickness of the cell enhanced $J_{SC}$ from 14.63mA/$cm^2$ to 19.55mA/$cm^2$.

However, the open circuit voltage ($V_{OC}$) of the microcells exhibit diminished value from that of the bulk cells. This is due to the difference in the backside field of the each device. The backside field which is achieved by doping boron on the bottom surface of the cells was not formed sufficient for the microcells because the doping solid source was facing opposite side of the targeting surface when the doping process took place whereas for the bulk reference cell, the solid source was facing directly targeting surface during the doping. This caused difference in the doping level of cells on the backside and resulted in reduced back bias in the microcells.

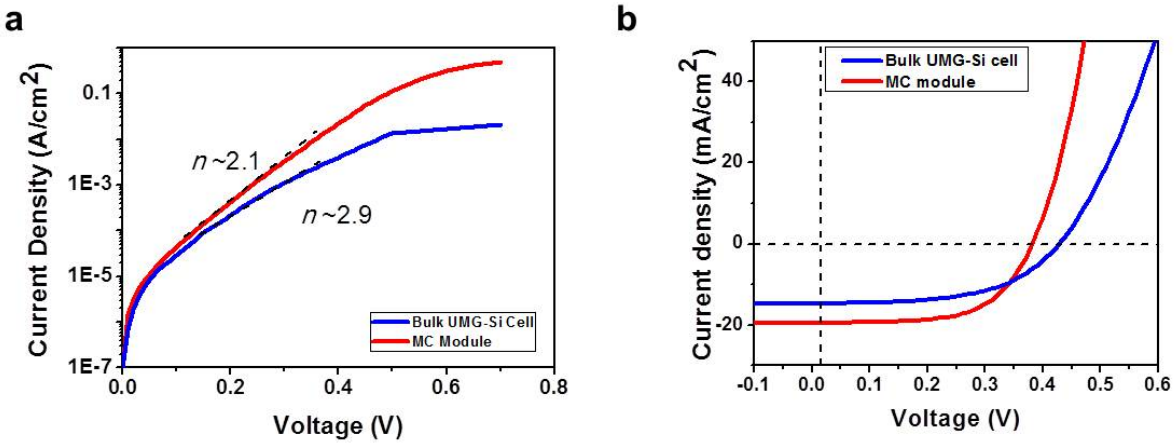


**Figure 3.13 Representative J-V curves for the 180 µm thick UMG-Si cell (blue) and the prepared microcell module (red) under (a) dark condition and (b) under illumination of 1000W/m$^2$.**

**Table 3-3 J-V characteristics of the 180 µm thick bulk UMG-Si solar cell and the prepared ultrathin microcell module.**

| **Microcells** | **$J_{SC}$ (mA/cm$^2$)** | **$V_{OC}$(V)** | **FF** | **η (%)** |
|---|---|---|---|---|
| Doped UMG-Si | 14.63 | 0.47 | 0.55 | 3.77 |
| Ribbon MC | 19.55 | 0.40 | 0.60 | 4.69 |

Degradation of hydrogenated amorphous-Si (α-Si:H) thin film solar cells during long term exposure of light is a well-known phenomenon and this is called as "Staebler-Wronski effect"[125-128]. Although our microcells have small thickness compared to the conventional bulk cells, because they are generated from multicrystalline wafer, we predicted that the microcells would show good stability in terms of performance over time. In order to verify this, we measured the J-V of newly made microcells and 3 month old microcells and compared their performances under 1 sun illumination. Fig. 3.14 shows the measured J-V curves and the detailed characteristics are in Table 3-4. The differences that can be found from the $J_{SC}$ and η values are negligible and therefore these results demonstrate robust device performance of the ultrathin solar microcells

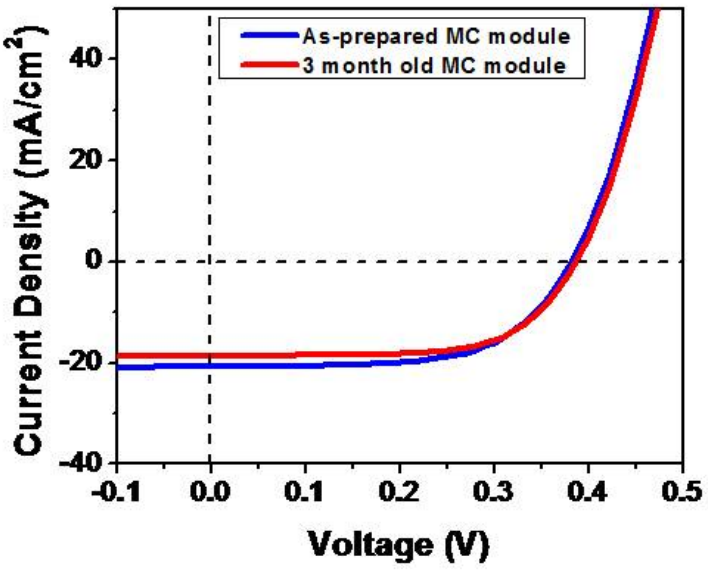


**Figure 3.14 J-V curves of as prepared microcell module (blue) and 3 month old microcell module (red). The prepared microcell module has good sustainability over 3 months.**

**Table 3-4 J-V characteristics of as prepared microcell module and 3 month old microcell module.**

| Microcells | $J_{SC}$ (mA/cm$^2$) | $V_{OC}$(V) | FF | η (%) |
|---|---|---|---|---|
| As-prepared MC module | 19.55 | 0.40 | 0.60 | 4.69 |
| 3 month old MC module | 19.47 | 0.39 | 0.60 | 4.56 |

### 3.4.4 Optical Characteristics of the Solar Microcells

To achieve high efficiency from Si solar cell, it is important for Si to absorb incoming light as much as possible. The amount of light absorbed depends on the optical path length and absorption coefficient. The attenuated light intensity in a material can be expressed as a function of the penetrating depth of light (d), which is as below.

$$I(d) = I_0 e^{-\alpha d} \tag{3.4}$$

In eq. (3.4), α indicates the absorption coefficient that is a property of a material that defines the amount of light that is absorbed by it. The inverse of absorption coefficient, $\alpha^{-1}$, is the average distance traveled by a photon before it gets absorbed and this value is called as absorption depth. The solar cell material should be thicker than the absorption depth $\alpha^{-1}$ (E) in order to absorb the photon of energy E. In case of Si in which the absorbed photon energy ranges between 400 nm and 1100 nm, the thickness should be around 130 μm to absorb sufficient photons without transmitting.

The small physical thickness of our microcells (~ 17 μm) can be a major hurdle of achieving good light absorption. By using commercial software (Essential Macleod), the absorbance of both bulk Si (180 μm) and ultrathin Si (17 μm) were calculated and their plots are shown in Fig. 3.15. Although reducing the Si thickness improved the carrier

collections, it aggravated the absorbance especially at longer wavelength (from ~750 nm).

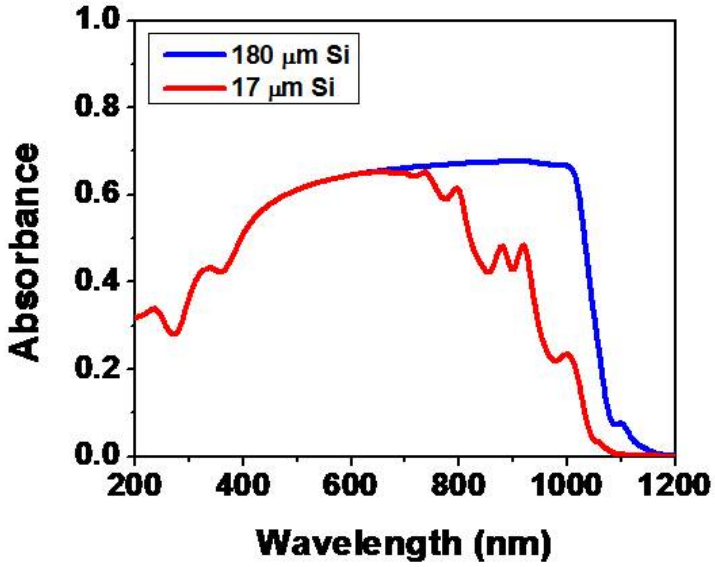


**Figure 3.15 Calculated absorbance spectrum of 180 μm thick Si (blue) and 17 μm thick Si significantly decreased in the long wavelength region. This calculation was executed using the Essential Macleod software (ver. 9.4).**

## 3.5 Ag Nanoparticles and Si Nanopillar Arrays on Solar Microcells

So far, we discovered remarkable absorption enhancements in Si by incorporating Ag nanoparticles or Ag nanoparticle/Si nanopillar arrays on the surface. Throughout the investigation of electrical and optical properties of bulk UMG-Si solar cell with various features, we chose 34 nm for the diameter of Ag nanoparticles and Ag nanoparticle/Si nanopillar arrays structures on the solar microcells since 34 nm Ag nanoparticle showed superior performance to 18 nm Ag nanoparticles. As described in chap. 3.2, same procedures were carried out on the microcells. The schematic of preparation of Ag nanopartilces and Ag nanoparticle/Si nanopillar arrays are shown in Fig. 3.16.

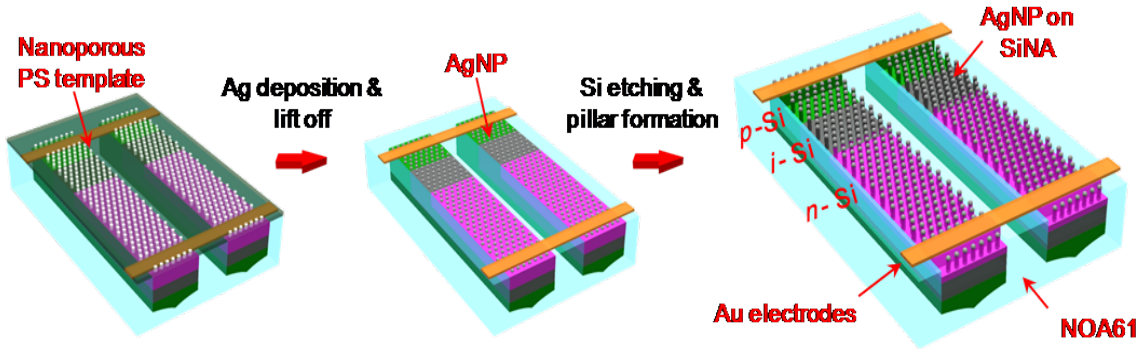


**Figure 3.16 Schematic illustration of the preparation of periodic and uniform Ag nanoparticles and Ag nanoparticle/Si nanopillar arrays on microcells.**

During the process of block copolymer lithography, we discovered that the PS-b-PMMA self-assembled film was selectively formed on the Si surface. This was confirmed from the SEM images in Fig. 3.16 (a) which was taken after PMMA removal showing nanopatterned PS template on Si microcells whereas no patterned structure on NOA 61 surface. This can be explained by the absence of –OH group on the surface of NOA 61 which is critical for obtaining self-assembled morphologies from block copolymers. However, this characteristic turned out to be beneficial for our microcell device, since this made it possible to have NOA 61 transparent and clean after formation of Ag nanoparticles. Fig. 3.16 (b) shows the optical image of the final microcells that have Ag nanoparticle/ Si nanopillar arrays on the microcells' surface showing excellent flexibility and semitransparency.

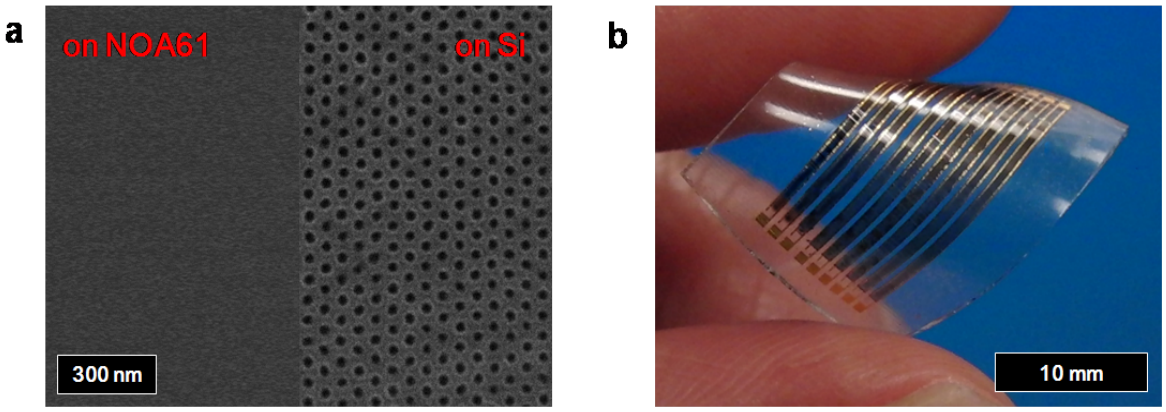


**Figure 3.17 (a) SEM images of the as-prepared PS template on a polymer substrate (NOA 61) and Si. The block copolymer (PS-b-PMMA) thin film was selectively self-assembled on the Si surface. (b) An optical image of a microcell module with Ag nanoparticle/Si nanopillar arrays structure. Both block copolymer lithography and reactive ion etching (RIE) did not affect the flexibility and the semitransparency of the microcell module.**

The J-V measurements were conducted under illumination of 1000W/m$^2$ for three different solar microcells: (1) a bare microcell with no Ag nanoparticles, (2) Ag nanoparticles on a microcell, and (3) Ag nanoparticles/ Si nanopillar array on a microcell. The J-V curves of these cells are shown in Fig. 3.17 and their detailed characteristics are in Table 3-5.

The $J_{SC}$ of the bare, Ag nanoparticle, and Ag nanoparticle/Si nanopillar array microcells were measured to be 19.55mA/cm$^2$, 24.32mA/cm$^2$, and 31.77mA/cm$^2$, respectively and their measured efficiencies (η) were 4.69%, 5.93%, and 8.08%, respectively. The $V_{OC}$ and FF did not exhibit noticeable changes showing values of ~ 0.4V and ~ 0.6, respectively. The current density ($J_{SC}$) exhibited constant increment as the nanostructures were added to the microcells and this implies that Ag nanoparticles and Ag nanoparticle/ Si nanopillar arrays are contributing to absorption enhancements.

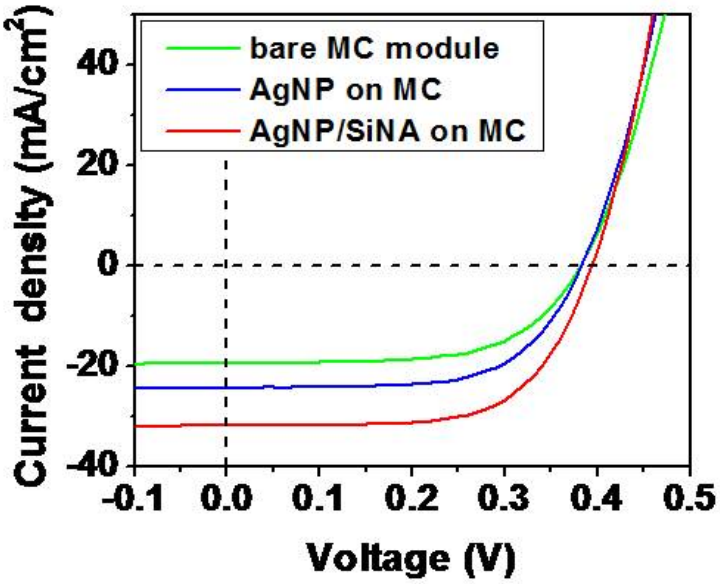


**Figure 3.18 Representative J-V curves of the bare microcell module (green), Ag nanoparticles on microcell module (blue), and Ag nanoparticle/Si nanopillar arrays on microcell module (red). The microcells were 17 μm thick.**

**Table 3-5 J-V characteristics of bare microcell module, Ag nanoparticles on microcell module, and Ag nanoparticle/Si nanopillar arrays on microcell module.**

| Microcells | $J_{SC}$ (mA/cm$^2$) | $V_{OC}$(V) | FF | η (%) |
|---|---|---|---|---|
| bare MC module | 19.55 | 0.40 | 0.60 | 4.69 |
| AgNP on MC | 24.32 | 0.40 | 0.61 | 5.93 |
| AgNP/SiNA on MC | 31.77 | 0.41 | 0.62 | 8.08 |

## 3.6 Conclusion

In this chapter, the fabrication method of creating nanostructures that can induce both plasmonic effect and anti-reflection and incorporation of the structures to the microcells were demonstrated. Implementing PS-b-PMMA self-assembly enabled obtaining metallic nanoparticles with diameters of 18nm and 34nm and further etching allowed forming Si nanopillars in addition to the nanoparticles. The detailed studies of

optical and electrical properties of bulk UMG-Si solar cells with various dimensions of Ag nanoparticle/ Si nanopillar array further elucidated the effects of the incorporation of the nanostructures on the overall solar cell performance.

From the investigation of the properties of UMG-Si, which was presented in chapter 2, it was predicted that the minority carrier diffusion length in UMG-Si is much shorter than that of crystalline Si. General approach to achieve moderate carrier collection from utilization of low quality material is to reduce the thickness of the solar cell so that the carriers can reach the electrode from the metallurgical p-n junction before the recombination can take place. We followed this strategy by producing 17 μm thick solar microcells from UMG-Si wafer.

Our solar microcells possess unique properties such as good mechanical flexibility and semitransparency that cannot be achieved from conventional fabrication techniques. Moreover J-V characteristic and diode ideality factor evaluations made it clear that 17 μm thicknesses of microcells enhance the collection of photogenerated carriers compared to the bulk (180 μm – thick) cells. However, optical calculation of Si in this thickness revealed light absorption loss at the long wavelength region.

After integration of Ag nanoparticles and Ag nanoparticles/Si nanopillar arrays, the low-cost UMG-Si based 17 μm thick solar microcell module exhibit enhanced performance. These nanostructures significantly increased light absorption in Si by plasmonic, antireflection, and light trapping effects induced by Ag nanoparticles and Si nanopillar arrays. The resulting solar microcell module yielded $\eta > 8\%$ efficiency.

Further enhancement in efficiency may be possible with surface passivation and backside reflection. The results reported here may provide useful design considerations for the future work in Metallurgical Grade (MG)-Si and other classes of solar cell systems.

# Chapter 4

# Multiple –Plasmonic Layers for Extreme Light Trapping

## 4.1 Introduction

In this work LSPR from multiple layers of metallic nanoparticles together with dielectric anti-reflection coating were implemented to increase the absorption of UMG-Si. In this chapter, the methodology of creating multiple plasmonic layers[87] (either double or quadruple plasmonic metallic nanoparticles layers) on the surface of UMG-Si solar cells using block copolymer lithography is introduced. Detailed studies on the electrical and optical properties of the developed solar cells elucidate the light trapping contributions of each individual layer and finally optimized structure that maximizes the light absorption and conversion efficiency was selected for application to the ultrathin UMG-Si cell.

The main challenge in developing solar cells utilizing thin Si film is poor absorption [112, 123]. Here, ultrathin (~12 μm thick) UMG-Si based solar cells that exhibit good bendability was prepared and investigation of its electrical and optical properties revealed severe optical loss. We equipped this solar cell with the optimized light trapping multiple-plasmonic layers and finally achieved ~11% conversion efficiency.

## 4.2 Fabrication of Multiple-Plasmonic Layers on UMG-Si

The overall experimental procedures of producing multiple-plasmonic layers on the bulk/ultrathin UMG-Si are depicted in the Fig. 4.1. The double side polished upgraded metallurgical grade (UMG) Si (thickness: 180μm for bulk solar cell/ 12μm for ultrathin solar cell) substrate was doped with boron at the bottom and phosphorous on top. A random copolymer PS-b-PMMA brush neutrally treated the top surface of doped UMG-Si. A thin film (100 nm) of asymmetric block copolymers, polystyrene-block-poly (methyl methacylate) (PS-b-PMMA) forming cylindrical nanostructures (molecular weight: PS/PMMA-46k/21k, PMMA cylinder diameter: 18 nm, center to center distance between neighboring cylinders: 34 nm) were spin-coated onto the wafer surface. After annealing at 190 °C, the substrates were irradiated with UV and subsequently rinsed with acetic acid and water to remove PMMA cylinder cores and crosslink the PS matrix. Using the PS nanotemplate as an etching mask, the UMG-Si substrate was etched in by RIE ($SF_6/C_4F_8$) to produce nanoporous structures, and the remaining PS nanoporous template was removed by oxygen plasma. This process duplicated the hexagonal arrangement of the block copolymer template and produces a highly dense and uniform nanoporous array on the surface of UMG-Si solar cells. The top-down and tilted views of the nanoporous UMG-Si is shown in Fig. 4.2 (a) and (b). The tilted view in Fig. 4.2 (b) shows that the mean depths of the naopores are ~ 20 nm.

For producing plasmonic nanoparticles, a metallic (either Ag or Au) thin film (t = 5 nm) was deposited over the nanoporous UMG-Si substrate, and the substrate was subsequently annealed on a hot plate (100°C, 10 min). This caused the deposited metal thin film to get wet and form nanoparticles both within the nanopores as well as outside

the nanopores, respectively. The metal nanoparticles have mean diameters of 16 nm and 18 nm inside and outside the nanopores respectively. These two plasmonic layers together constituted the bottom "double plasmonic layer" on the UMG-Si solar cell. The top-down views of nanoporous UMG-Si covered with metal film and after annealing are shown in Fig. 4.2 (c) and (d). The spin-on-glass (SOG) solution was spin coated on the double plasmonic layer and annealed for 1 hour at 400 °C. This layer is for the enhanced anti-reflection[129, 130] and served as a substrate for the deposition of two additional plasmonic layers. The top two plasmonic layers were fabricated on SOG film using the same procedure as was used earlier to fabricate the bottom two plasmonic layers. The final structure incorporates the bottom double plasmonic layers, the SOG, and the top double plasmonic layers which we call "quadaruple plasmonic layer" structure. The final structure is depicted in Fig. 4.3.

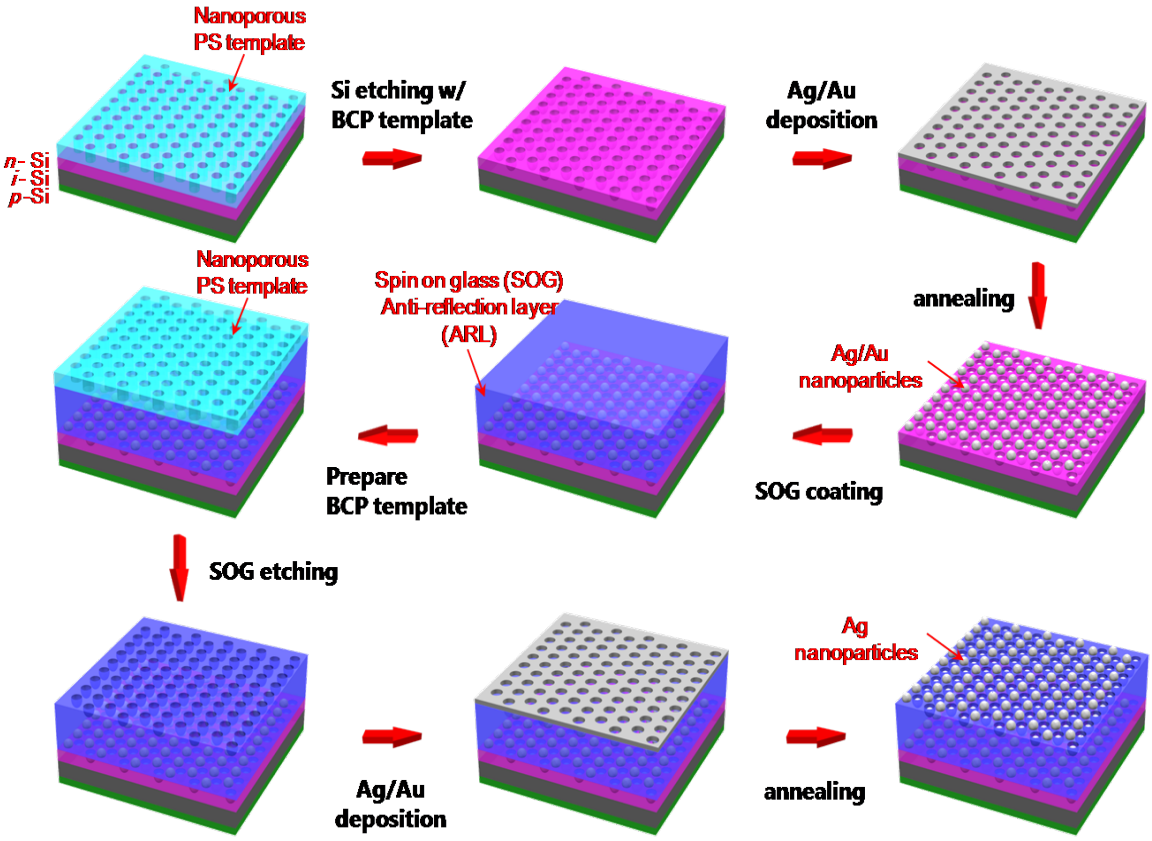


**Figure 4.1 Schematic illustration of the steps of producing quadruple plasmonic layer on ultrathin UMG-Si based solar cells.**

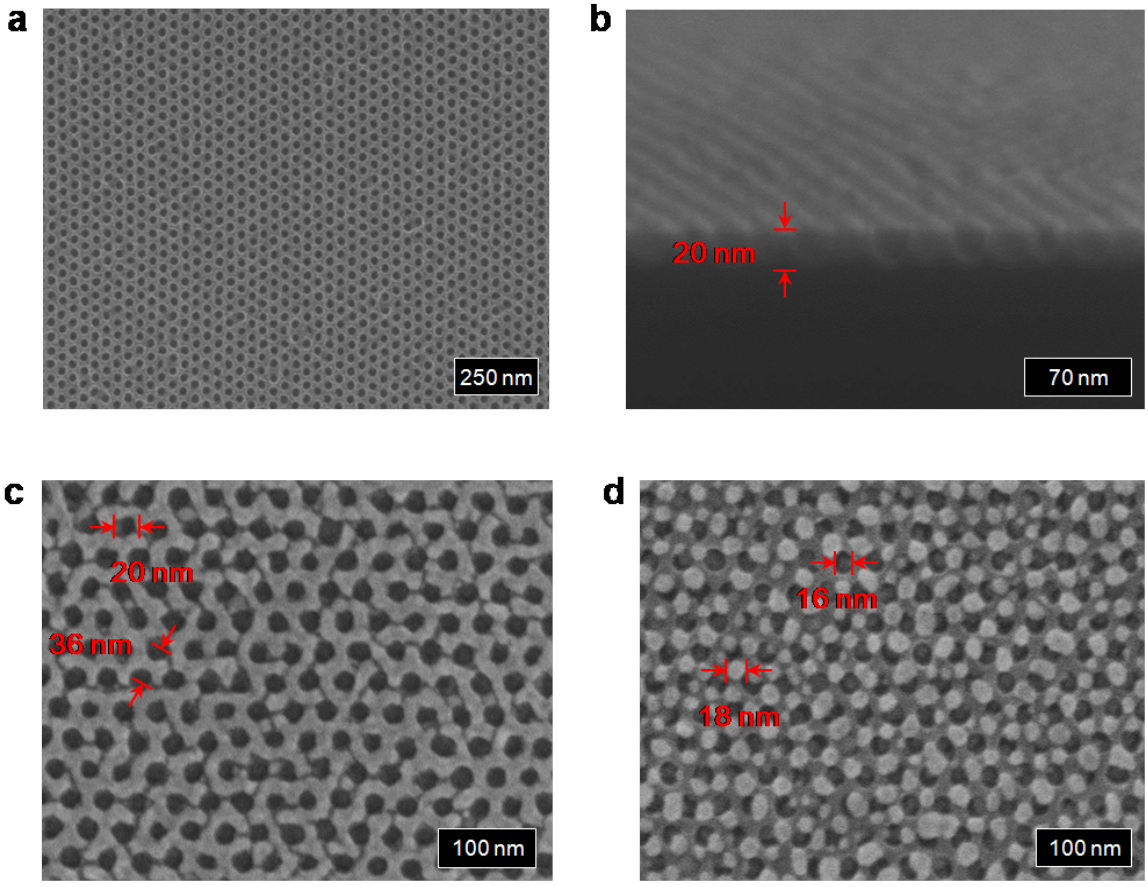


**Figure 4.2 SEM images of (a) top and (b) tilted view of the nanoporous UMG-Si patterned with block copolymer lithography. SEM images of nanoporous UMG-Si after depositing 5nm of Ag film (c) before and (d) after annealing.**

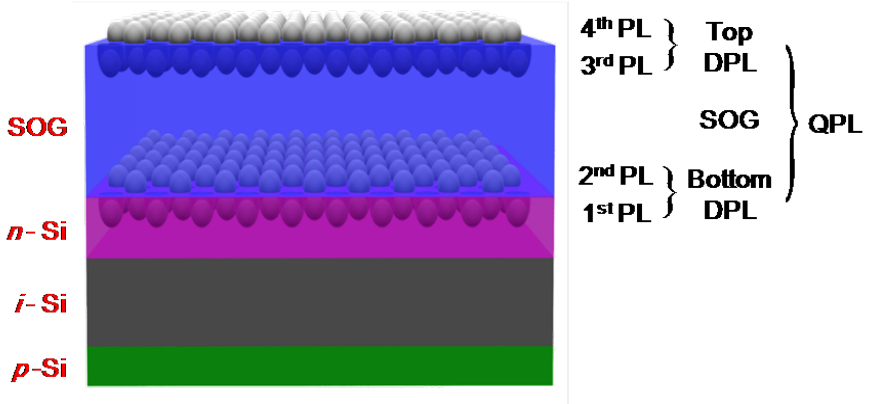


**Figure 4.3 Schematic illustration of the structure of quadruple plasmonic layers on UMG-Si solar cells. The total accumulated structure of "bottom double plasmonic layer/ spin-on-glass/top double plasmonic layer" worked as a quadruple plasmonic layer.**

## 4.3 Investigation of Constituents Comprising the Quadruple Plasmonic Layer

### 4.3.1 Electrical Studies of Solar Cells with Multiple-Plasmonic Layers

In order to have better understanding in the contribution of each constituent within the fabricated solar cells, the evaluations on the device performance on five different structures on 180 μm thick UMG-Si based solar cells were carried out: (1) A bare UMG-Si solar cell without any features, (2) a nanoporous UMG-Si solar cell, (3) an UMG-Si solar cell with Ag based double plasmonic layer, (4) an UMG-Si solar cell with Ag based double plasmonic layer, along with a top coating of SOG, and (5) an UMG-Si solar cell with quadruple plasmonic layer. The thickness of the SOG and the deposited Ag film were 100nm and 5nm respectively.

J-V measurements of the five different solar cells were conducted and the curves are plotted in Fig. 4.4 (a). The detailed J-V characteristics are in Table. 4-1. The J-V curves show that $J_{SC}$ consistently increases as the plasmonic layers are added to the surface of the UMG-Si solar cell. For example, $J_{SC}$ of bare UMG-Si cell was measured to be 13.67mA/cm$^2$, whereas the $J_{SC}$ of the UMG-Si cell with quadruple layer was 34.23mA/cm$^2$. These measurements manifest that $J_{SC}$ is greatly increased by the presence of the bottom double plasmonic layer, SOG, and the top double plasmonic layer. This increase of the short circuit current is attributed to the absorbance enhancement caused by the light trapping effects of each plasmonic layer, and the anti-reflection properties of SOG film [131].

The use of the plasmonic light trapping layers and anti-reflection layer influences $V_{OC}$ (open circuit voltage) and FF (fill factor) as well. Surface recombination of carriers results in a decrease of $V_{OC}$ and FF especially in thin film materials [40, 132, 133]. The front surface of the cell corresponds to the highest carrier generation region in the solar cell since most of the incident light is absorbed there. Decreasing surface recombination is typically achieved by reducing the number of dangling bonds at the front surface using a surface passivation layer. Fig. 4.4 (b) shows the $V_{OC}$ and FF for the same five cells as Fig. 4.4 (a). The data clearly shows that the surface passivation using SOG enhances both the $V_{OC}$ and FF. Overall, due to the absorption enhancement and surface passivation effect, the 180 μm thick UMG-Si cell with the quadruple plasmonic layer exhibited a very high efficiency of 11.5 %.

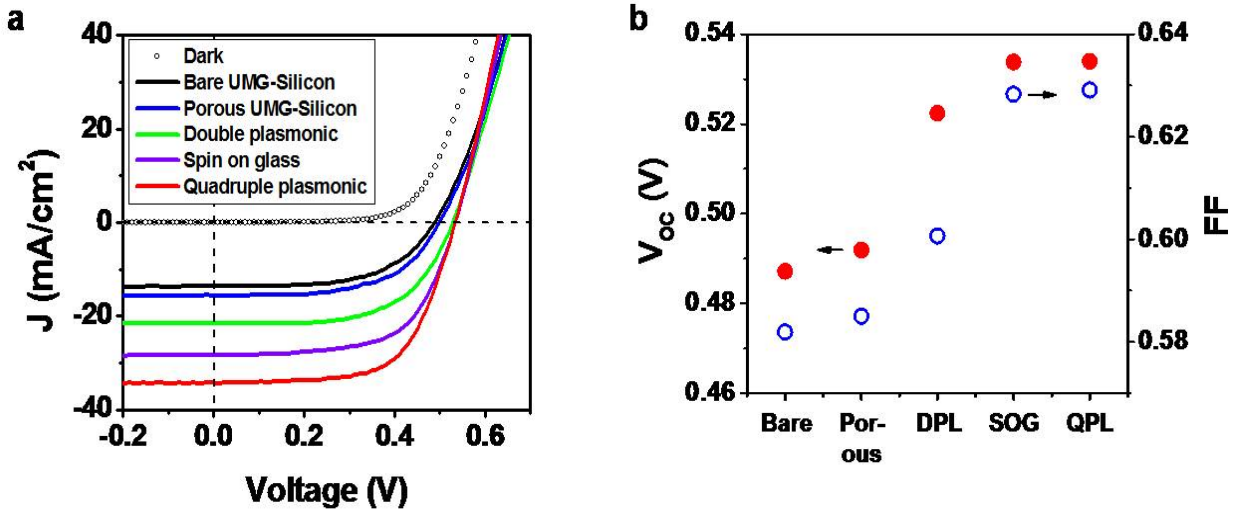


**Figure 4.4(a) J-V curves for bare UMG-Si (black), nanoporous UMG-Si (blue), Ag based double plasmonic layer on UMG-Si (green), and UMG-Si with Ag based quadruple plasmonic layer. (b) Absorbance spectrums for bare UMG-Si (black), double plasmonic layer on UMG-Si (green), and Ag based quadruple plasmonic layer on UMG-Si.**

**Table 4-1 J-V characteristics of bare UMG-Si, porous UMG-Si, Ag based double plasmonic layer (Ag-DPL) on UMG-Si, SOG on Ag based double plasmonic layer, and Ag based quadruple plasmonic layer (Ag-QPL) on UMG-Si.**

| Solar cells | $J_{SC}$ (mA/cm$^2$) | $V_{OC}$ (V) | FF | η (%) |
|---|---|---|---|---|
| Bare UMG-Silicon | 13.67 | 0.49 | 0.58 | 3.88 |
| Porous UMG-Silicon | 15.61 | 0.49 | 0.58 | 4.43 |
| Ag-DPL on UMG-Silicon | 21.53 | 0.52 | 0.60 | 6.89 |
| SOG on Ag-DPL | 28.27 | 0.53 | 0.63 | 9.48 |
| Ag-QPL on UMG-Silicon | 34.23 | 0.53 | 0.63 | 11.50 |

### 4.3.2 Optical Studies of Multiple-Plasmonic Layers

To better elucidate the effects of the individual plasmonic layers on the absorbance of the five solar cells, the reflectances (R) as a function of wavelength in the range 300 nm < λ < 950 nm for the bare UMG-Si cell, UMG-Si cell with the double plasmonic layer, and the UMG-Si cell with the quadruple plasmonic layer were investigated. Fig. 4.2 (a) shows the calculated absorbance of the three cells. The absorbances were calculated by subtracting the measured reflectance from unity assuming that 180 μm thickness is enough to allow no transmission losses (α (E) = 1 – R (E)). The double plasmonic layer dramatically enhanced the absorbance of UMG-Si cell for all wavelengths greater than 400 nm. In chapter 2, it was demonstrated that point dipole prediction and Fröhlich condition could be applied for a small metal particles (a << λ). According to Fröhlich condition, the resonance enhancement of polarization occurs when $|\varepsilon(\omega) + 2\varepsilon_m|$ is minimum (≈ 0) and particularly for single Ag sphere in air, this occurs at ~ 400 nm. In chapter 3.3.2, we demonstrated that in case of arrays of Ag

hemispheres on Si substrate, the resonance peak appears at ~ 450 nm due to scattering into Si and interactions between local electromagnetic modes. However in double plasmonic structure that is composed of 1st plasmonic layer that is embedded in Si and 2nd plasmonic layer that is on Si surface, have larger proportion of Si in the surrounding medium . Therefore, the wavelength that gives rise to plasmonic resonance undergoes further red-shift. Absorbance difference with respect to the bare Si was plotted in Fig. 4.5 (b) so that absorption in Si can be eliminated. The plot clearly shows the resonance peak at the longer wavelength (at 600 nm) than ~ 450 nm which is consistent with the theoretical prediction [56-58]. In contrast to the Ag double plasmonic layer, quadruple plasmonic layer has an additional SOG anti-reflective layer, and a top Ag based double plasmonic layer. The absorbance of the quadruple plasmonic layer reached ~ 98% across the entire wavelength spectrum, making the cell nearly a perfect light absorber.

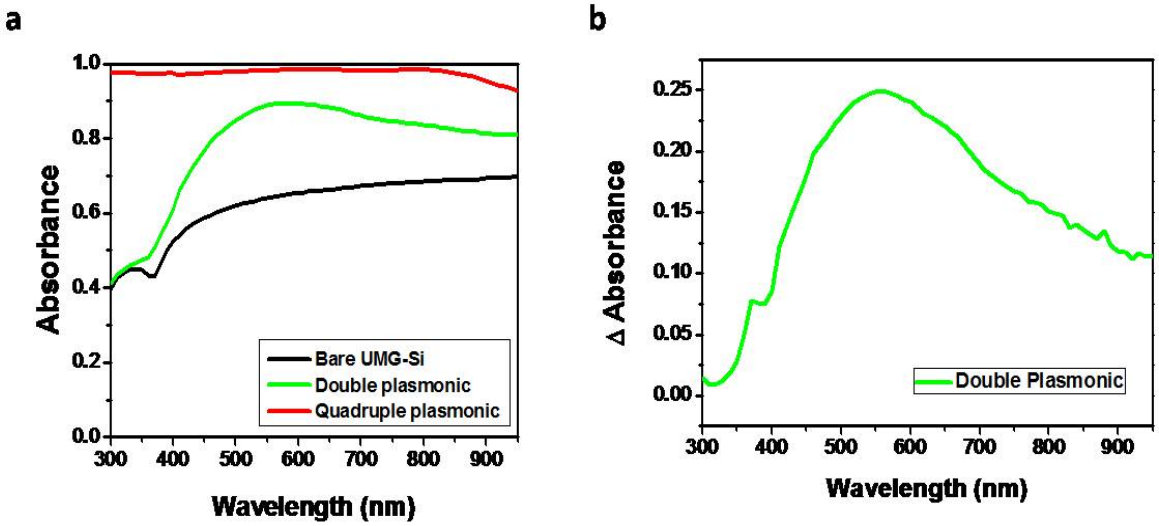


**Figure 4.5 (a) Absorbance spectrums for bare UMG-Si (black), double plasmonic layer on UMG-Si (green), and Ag based quadruple plasmonic layer on UMG-Si. (b) Absorbance difference with respect to the bare cell for double plasmonic layer on UMG-Si.**

### 4.3.3 Optical Modeling of Multiple-Plasmonic Layers on Si

To further elucidate the absorbance enhancement effects of multiple plasmonic layers on Si, the electromagnetic field intensities and the power absorption profiles for bare Si, the double plasmonic layer on Si, and the quadruple plasmonic layer on Si were calculated using FDTD method (Lumerical Solution, Inc). The designed structures' details for the calculations are the same as the actual structure in the experiments and they are depicted in Fig. 4.6.

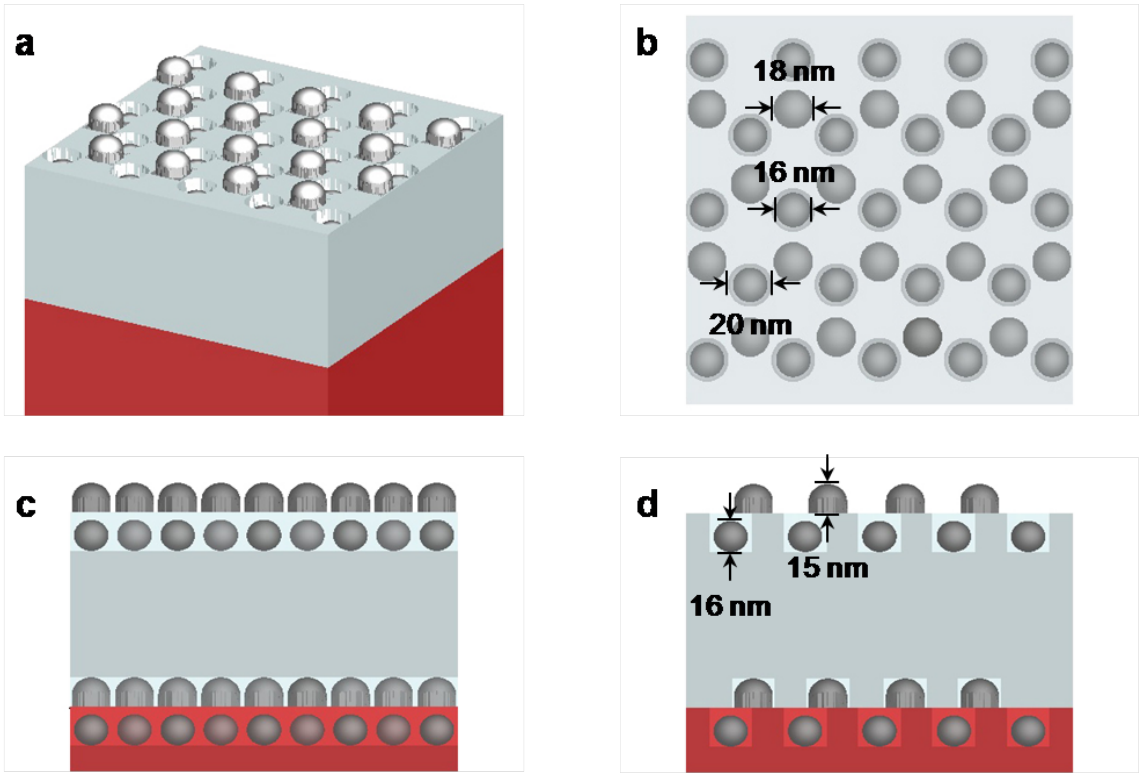


**Figure 4.6 (a) Perspectvie view, (b) x-y plane view, (c) x-z plane view, and (d) y-z plane view of the simulated structure of quadruple plasmonic layer on Si substrate. The lateral profile of nanoporous Si and nanoporous SiO2 substrate was set to be hemi-ellipse (D = 20nm, depth = 20nm). The bottom Ag/Au particles of double plasmonic layer were placed on the center of the pore, and the shape of them were set to be sphere (D = 16nm). The top Ag nanoparticles of double plasmonic layer were placed on the center from the three adjacent pores, and the shapes of them were set to be hemi-ellipse (D = 18nm, height = 15nm).**

The calculated electric fields maps are displayed in Fig. 4.7 (a), (b), and (c) and they clearly show the strong light trapping at the interface between the Ag nanoparticles and Si. The calculated total power absorption maps in Si are displayed in Fig. 4.7 (d), (e), and (f). The power absorption maps also show similar trend as the electric field maps, showing remarkable enhancements with the presence of both the Ag based double plasmonic layers and the quadruple plasmonic layer.

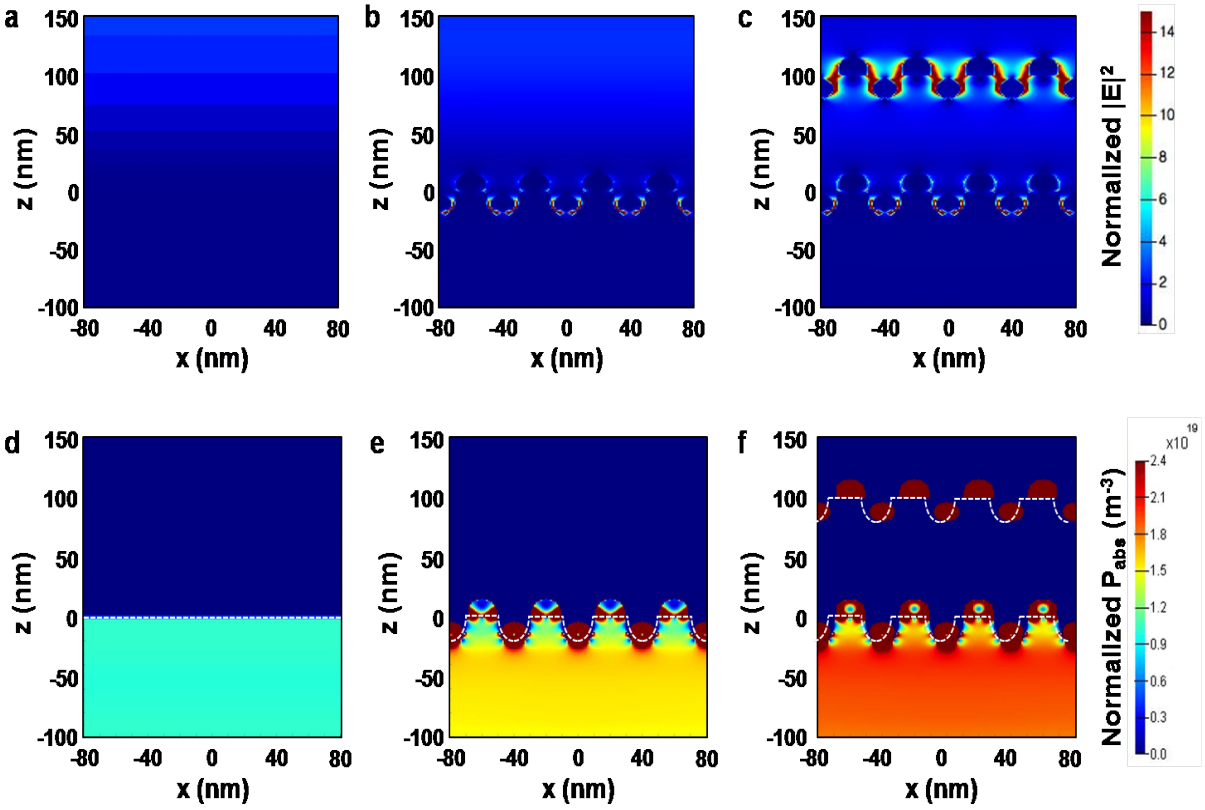


**Figure 4.7 Electric field intensity profiles and power absorption profiles calculated by Lumerical under an incident light of 600nm for x-z plane of (a and d) bare Si, (b and e) Ag based double plasmonic layer on Si, and (c and f) Ag based quadruple plasmonic layer on Si.**

### 4.3.4 Light Trapping Effect of Ag Nanoparticles at Different Locations

FDTD modeling of each constituent of the bottom double plasmonic layer, which are Ag nanoparticles buried in Si nanopores (first layer) and Ag nanoparticles sitting on the surface of the Si ( second layer), were carried out in order to better understand each layer's contributions to the absorption enhancements. Fig. 4.8 (a) shows the simulated structures, (b and c) show the calculated field intensity map and (d and f) show the power absorption map of each plasmonic layer that comprises the bottom double plasmonic layer.

LSPRs are non-propagating waves that are confined to the interface between metal and the surrounding dielectric[50, 54, 55]. Therefore magnitude of interfacial area becomes a key factor that determines the intensity of plasmonic interaction. The Ag nanoparticles from the first plasmonic layer are buried within UMG-Si which allows for a larger interfacial area with between the nanoparticle and Si compared to the Ag nanoparticles from the second plasmonic layer that are sitting on the surface of Si. It is the larger interfacial area with Si in the first plasmonic layer that resulted in more significant light trapping. Hence, from this optical modeling we can conclude that placing the Ag nanoparticles inside Si is more effective for light trapping.

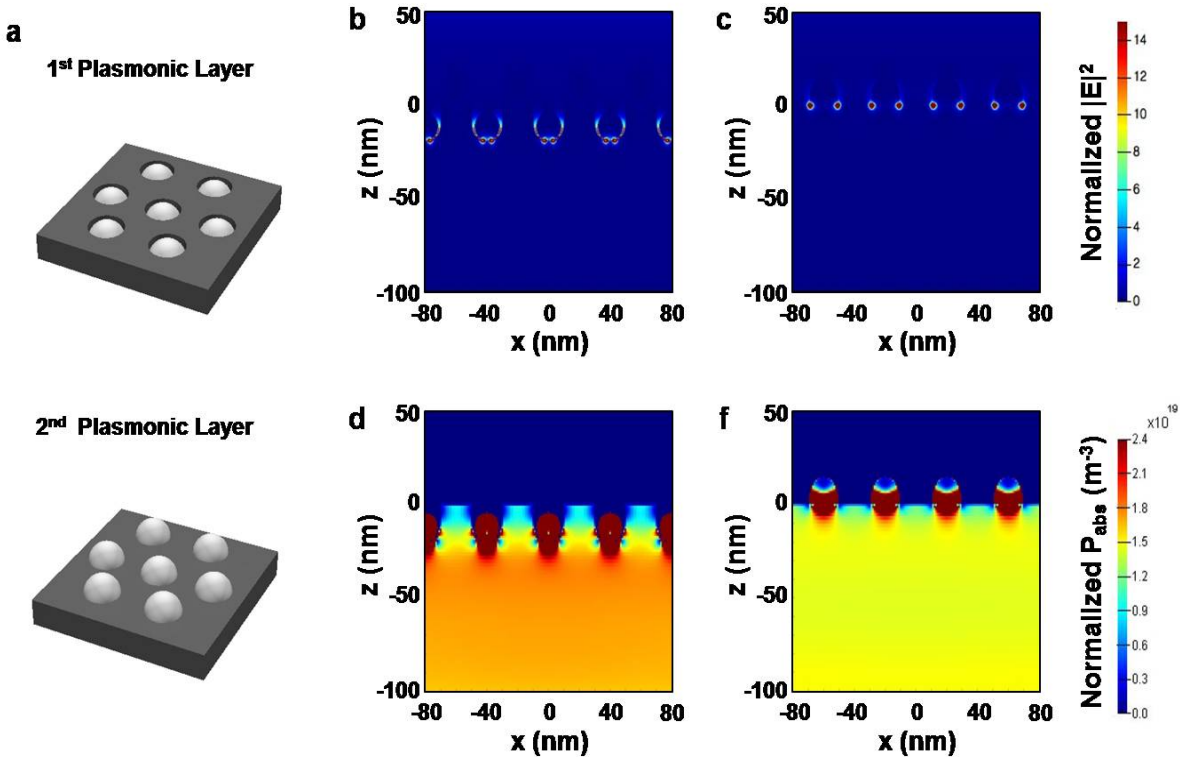


**Figure 4.8 (a and b) electric field intensity profiles and (c and d) power absorption profiles calculated by FDTD method under a incident light of 700nm for x-z plane of (a and c) first Ag based plasmonic layer of double plasmonic layer on Si and (b and d) second Ag based plasmonic layer of double plasmonic layer on Si.**

### 4.3.5 Optimization of Thickness of SOG Layer and Dimensions of Ag Nanoparticles

To maximize the light concentration and absorption due to the quadruple plasmonic layer, the three-dimensional placement of plasmonic nanoparticles and the surface passivation layer are critical. Fig. 4.9 (a) shows the J-V curves of the Ag based quadruple plasmonic solar cells as a function of SOG thickness and the detailed J-V characteristics are in Table 4-2. The thickness of SOG was varied from 0 nm, which is the cell where the double plasmonic layer was placed directly on the UMG-Si solar cell, to 200 nm. The $J_{SC}$ showed enhancements as the thickness of the SOG increased and

reached maximum when SOG was 100 nm. This observation shows good agreement with the previous works regarding optimized single-layer anti-reflective coating of $SiO_2$ for Si solar cells [129].

Fig. 4.9 (b) represents the J-V curves for Ag based quadruple plasmonic solar cells as a function of Ag thin film thickness. Since 100 nm of SOG was found to be the optimum, all of the cells' SOG thicknesses were fixed as 100 nm. The solar cell with 0 nm of Ag film indicates nanoporous UMG-Si solar cell with SOG on the top. As the Ag film's thickness increases, $J_{SC}$ showed significant enhancements and reached maximum value of 34.23mA/cm$^2$ when the Ag film was 5nm thick. However, $J_{SC}$ decreased with the further increase of Ag thickness and 15nm of Ag thin film finally yielded 7.09mA/cm$^2$, which is much lower than the bare UMG-Si solar cell. This trend is likely because with increasing the Ag film's thickness, it becomes more difficult to dewet the deposited Ag film. As a consequence, thick Ag film fails to form periodically placed Ag nanoparticles and remains as Ag thin film. The optical behavior of metal thin film is completely different from that of metal nanoparticles [54]. Thin metal films on semiconductor normally reflect light and hence prevent the underlying material from absorbing light. It is also possible for coherent electron oscillations to take place in metallic thin films, however this requires help of prism coupling [134, 135] or surface grating [136] if light is to be used to generate surface plasmons due to mismatch between momentum of surface plasmon mode and that of free-space photon of the same frequency [54, 55, 137]. The metal film with nanoscale gratings can be utilized as light trapping feature when placed at the backside of a solar cell by developing propagating surface plasmon mode at the interface between metal film and the absorbing semiconductor.

The J-V characteristic of 15 nm thick Ag film coated nanoporous UMG-Si cell implies the structure on the surface is nearly a thin Ag film and as a result, $J_{SC}$ and the device performance declined.

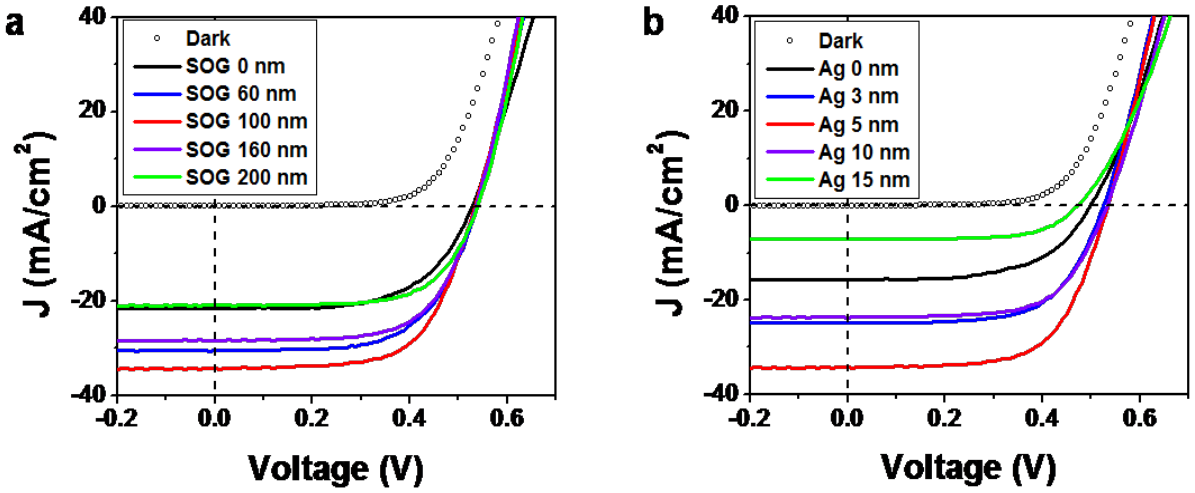


**Figure 4.9 (a) J-V curves of the Ag based quadruple plasmonic layer on 180µm thick UMG-Si solar cell as a function of spin-on-glass (SOG) thickness. (b) J-V curves for the Ag based quadruple plasmonic layer on 180 µm thick UMG-Si solar cell as a function deposited Ag film thickness.**

**Table 4-2 J-V characteristics of Ag based quadruple plasmonic layer (Ag-QPL) on UMG-Si as a function of spin-on-glass (SOG) thickness.**

| SOG thickness | $J_{SC}$ (mA/cm$^2$) | $V_{OC}$ (V) | FF | η (%) |
|---|---|---|---|---|
| 0 nm (Ag-DPL on UMG-Si) | 21.53 | 0.52 | 0.61 | 6.89 |
| 60 nm | 30.50 | 0.53 | 0.62 | 10.16 |
| 100 nm | 34.23 | 0.53 | 0.63 | 11.50 |
| 160 nm | 28.31 | 0.53 | 0.65 | 9.77 |
| 200 nm | 20.98 | 0.53 | 0.66 | 7.39 |

**Table 4-3 J-V characteristics of Ag based quadruple plasmonic layer on UMG-Si as a function of deposited Ag thickness.**

| Ag thickness | $J_{SC}$ (mA/cm$^2$) | $V_{OC}$ (V) | FF | η (%) |
|---|---|---|---|---|
| 0 nm (porous UMG-Si) | 15.61 | 0.50 | 0.58 | 4.55 |
| 3 nm | 24.80 | 0.53 | 0.63 | 8.29 |
| 5 nm | 34.23 | 0.53 | 0.63 | 11.50 |
| 10 nm | 23.73 | 0.53 | 0.63 | 7.98 |
| 15 nm | 7.09 | 0.47 | 0.64 | 2.15 |

## 4.4 Light Trapping Effects and Anti-Reflective Effects from Quadruple Plasmonic Layer

Absorption enhancement in the quadruple plasmonic layer involves both light trapping effects of Ag nanoparticles and anti-reflection effects of the SOG film. To further differentiate these two mechanisms, four different solar cells were fabricated and examined: (1) A bare UMG-Si cell, (2) a UMG-Si cell with a SOG layer, (3) a UMG-Si cell with a SOG layer, covered with top Ag based double plasmonic layer, and (4) a UMG-Si cell with bottom Ag based double plasmonic layer covered with SOG layer. Fig. 4.10 (a) shows the schematic of four prepared UMG-Si solar cells.

Fig. 4.10 (b) and (c) show the J-V curves and the efficiency measurements of the four prepared solar cells and the detailed characteristics are in Table 4-4. By comparing the performance of each cell, it became clear that good surface passivation from SOG was achieved since $V_{OC}$ and FF of the cells with SOG layer showed enhanced values. Further, the addition of SOG film resulted in absorbance enhancements of UMG-Si leading to increase in $J_{SC}$ up to 19.17mA/cm$^2$. The enhanced $J_{SC}$ brought 2.4% of efficiency increase. The addition of top Ag based double plasmonic layer (cell 3) and the

bottom plasomonic layer (cell 4) increased the $J_{SC}$ of the cells to 25.05mA/cm$^2$ and 28.28mA/cm$^2$, respectively. The changes in $V_{OC}$ (~ 0.53V) and FF (~ 0.63) among the three cells with SOG film were negligible. Therefore the top and the bottom Ag based double plasmonic layer increased the absolute efficiency of the cells by ~ 2.1% and ~ 3.2% respectively. The total efficiency improvements caused by the bottom Ag based double plasmonic layer (3.2%), SOG (2.4%), and the top Ag based double plasmonic layer (2.1%) add up to essentially the overall efficiency enhancement caused by the quadruple plasmonic layer on UMG-Si (7.5%).

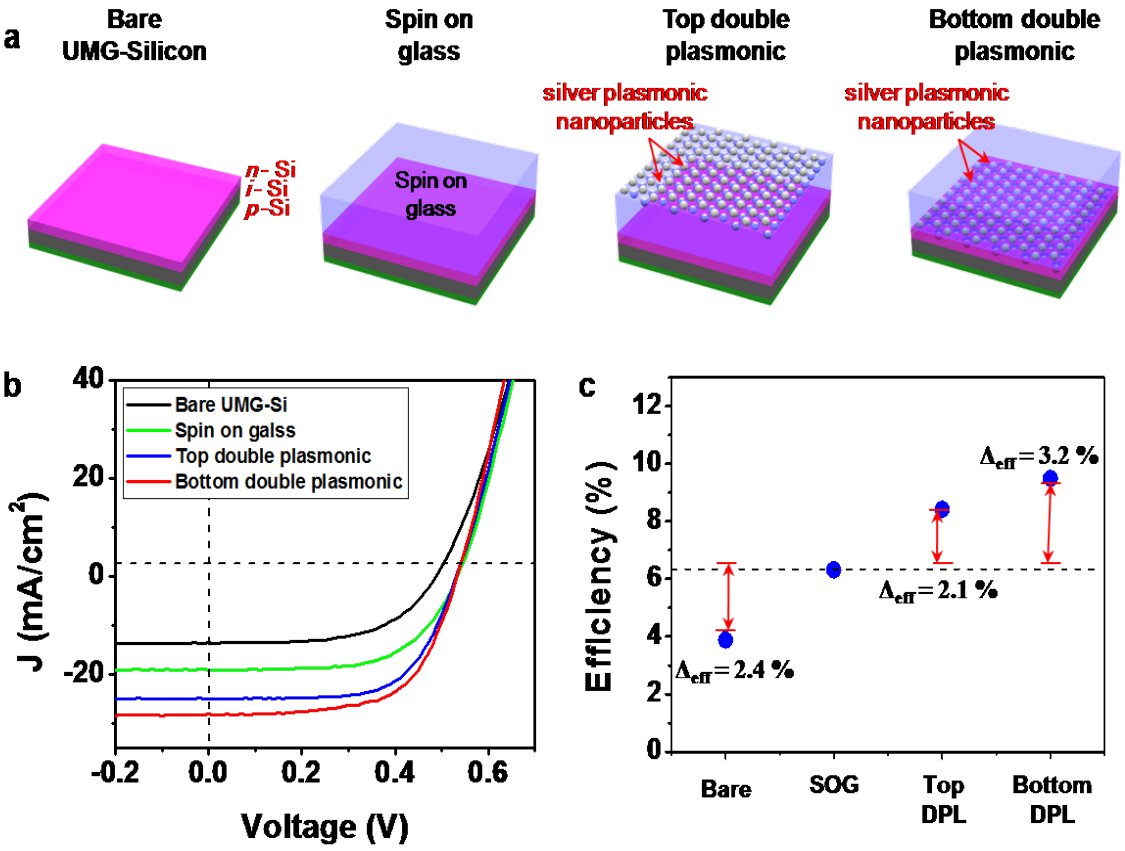


**Figure 4.10 (a) Schematic illustration of bare UMG-Si, spin-on-glass (SOG) on UMG-Si, top Ag based double plasmonic layer on SOG film, and bottom Ag based double plasmonic layer under SOG film. (b) J-Vcurves and (c) efficiency plots for each sample.**

**Table 4-4 J-V characteristics of bare UMG-Si, spin-on-glass (SOG)) on UMG-Si, top Ag based double plasmonic layer (Ag-DPL) on UMG-Si, and bottom Ag based double plasmonic layer (Ag-DPL) on UMG-Si.**

| Solar cells | $J_{SC}$ (mA/cm$^2$) | $V_{OC}$ (V) | FF | η (%) |
|---|---|---|---|---|
| Bare UMG-Silicon | 13.67 | 0.49 | 0.58 | 3.88 |
| SOG on UMG-Silicon | 19.17 | 0.53 | 0.62 | 6.32 |
| Top Ag-DPL | 25.07 | 0.53 | 0.63 | 8.42 |
| Bottom Ag-DPL | 28.28 | 0.53 | 0.63 | 9.49 |

The trend that was shown from the J-V measurements, also agrees with the calculated electric field intensity and power absorption profiles of $SiO_2$ on Si, top Ag based double plasmonic layer on Si, and bottom Ag based double plasmonic layer on Si. Fig. 4.11 shows the FDTD calculations of these cells. The larger increase in the magnitude of $J_{SC}$ caused by the bottom double plasmonic layer compared to the top double plasmonic layer can be explained by the difference in their respective dielectric environments. The bottom Ag based double plasmonic layer is surrounded by higher refractive index materials, Si (refractive index, n ~ 3.5) and $SiO_2$ (n ~ 1.5), which prevents significant dispersion of trapped light. In comparison, the top Ag based double plasmonic layer is surrounded by Air (n ~ 1) and $SiO_2$. When the metallic nanoparticle is placed close to the interface between two dielectrics, light scatters preferentially into the dielectric with the larger permittivity. Therefore, the bottom double plasmonic layer which is in touch with Si, contributes more to the light absorption than the top double plasmonic layer.

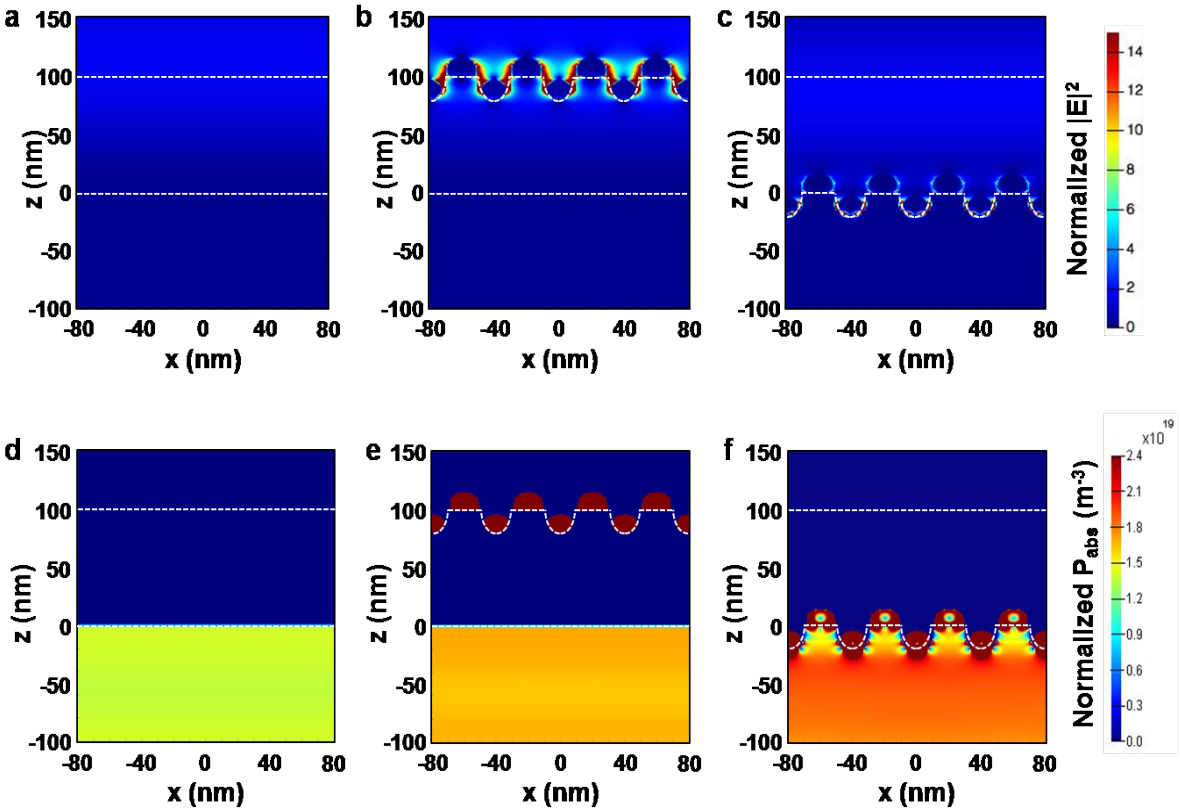


**Figure 4.11 Calculated electric field intensity profiles under an incident light of 600 nm for (a) $SiO_2$ (100 nm) on Si, (b) top Ag based double plasmonic layer on Si, and (c) bottom Ag based double plasmonic layer on Si. Calculated power absorption profiles for (d) $SiO_2$ (100 nm) on Si, (e) top Ag based double plasmonic layer on Si, and (f) bottom Ag based double plasmonic layer on Si.**

## 4.5 Comparison of Ag Nanoparticles and Au Nanoparticles

Besides Ag, other metallic nanoparticles can also be used to fabricate effective plasmonic light trapping layers. Gold (Au) nanoparticles have been previously considered as a good material for the application of plasmonics [69, 120, 138]. We compared the effects of utilizing Ag and Au nanoparticle layers within quadruple plasmonic layer on the overall efficiency of the UMG-Si solar cells. The first cell (denoted as the Au/Ag cell) has a bottom double plasmonic layer composed of Au nanoparticles, a SOG layer, and a

top double plasmonic layer composed of Ag nanoparticles. Fig. 4.12 depicts the cross-section of the first cell. The second cell (denoted as the Ag/Ag cell) has same quadruple plasmonic layer, which has been presented throughout this chapter that has both the bottom and the top double plasmonic layers composed of Ag nanoparticles.

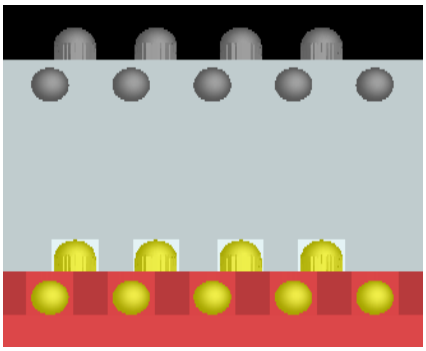

**Figure 4.12 Schematic of the cross-section of the quadruple plasmonic layer comprising bottom double plasmonic layers generated from Au nanoparticles, SOG layer, and top double plasmonic layers generated from Ag nanoparticles.**

Fig. 4.13 (a) and (b) show the J-V curves, FF, and overall efficiency plots for two UMG-Si cells with different quadruple plasmonic layers. According to Fröhlich condition and experimental reports [59, 79], the resonance of Au nanoparticles in air occurs at ~ 510 nm which is longer wavelength regime compared to Ag nanoparticles (400 ~ 450 nm) due to less electron density in Au relative to Ag which results in weaker restoring force inside the nanoparticle. Therefore we have used Ag nanoparticles for the top double plasmonic layers for both cells because so that the top plasmonic layer can trap the short wavelength light.

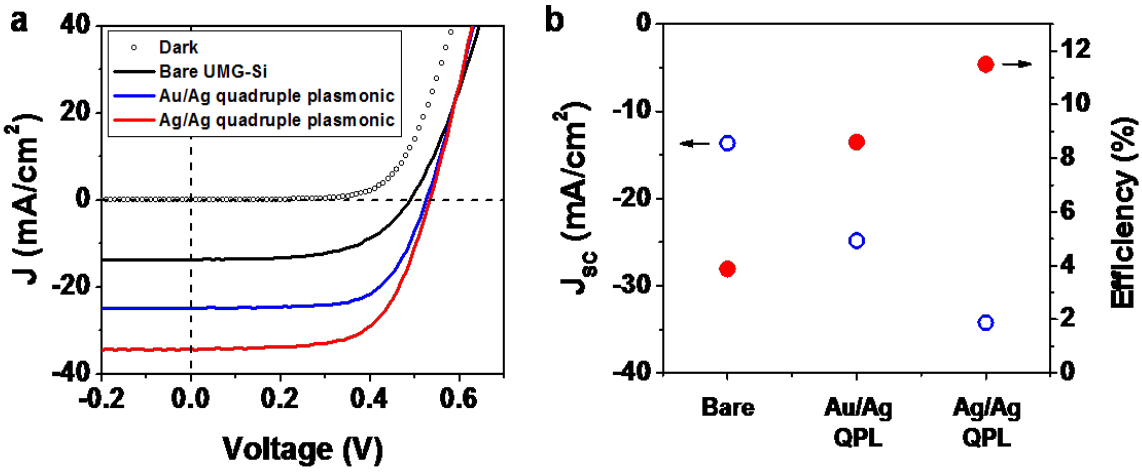


**Figure 4.13 (a) J-V curves as well as (b) fill factor (FF) and efficiency plots of bare UMG-Si, Au/Ag quadruple plasmonic layers and Ag/Ag quadruple plasmonic layer.**

**Table 4-5 J-V characteristics of bare UMG-Si, Au/Ag quadruple plasmonic layer on UMG-Si and Ag/Ag quadruple plasdmonic layer on UMG-Si solar cells.**

| Solar cells | $J_{SC}$ (mA/cm$^2$) | $V_{OC}$ (V) | FF | η (%) |
|---|---|---|---|---|
| Bare UMG-Silicon | 13.67 | 0.49 | 0.58 | 3.88 |
| Au/Ag QPL | 24.82 | 0.53 | 0.66 | 8.61 |
| Ag/Ag QPL | 34.23 | 0.53 | 0.63 | 11.50 |

Table 4-5 shows the detailed J-V characteristics of Au/Ag cell and Ag/Ag cell. The $J_{SC}$ for Au/Ag cell and the Ag/Ag cell were measured to be 24.82mA/cm$^2$ and 34.23mAg/cm$^2$ respectively. The FF for both cells showed small variation and were measured to be 0.66 and 0.63 respectively. Although Au/Ag cell showed slightly higher value for the FF (probably due to the anti-oxidation properties of Au), the Ag/Ag cell had a higher value for the $J_{SC}$ due to significantly higher light trapping. The calculated electric field intensity maps for the Au/Ag cell and the Ag/Ag cell shown in Fig. 4.11 (a) and (b)

respectively and they clearly show the difference in light trapping intensities between the Ag and Au nanoparticles. The power absorption profiles also support this hypothesis.

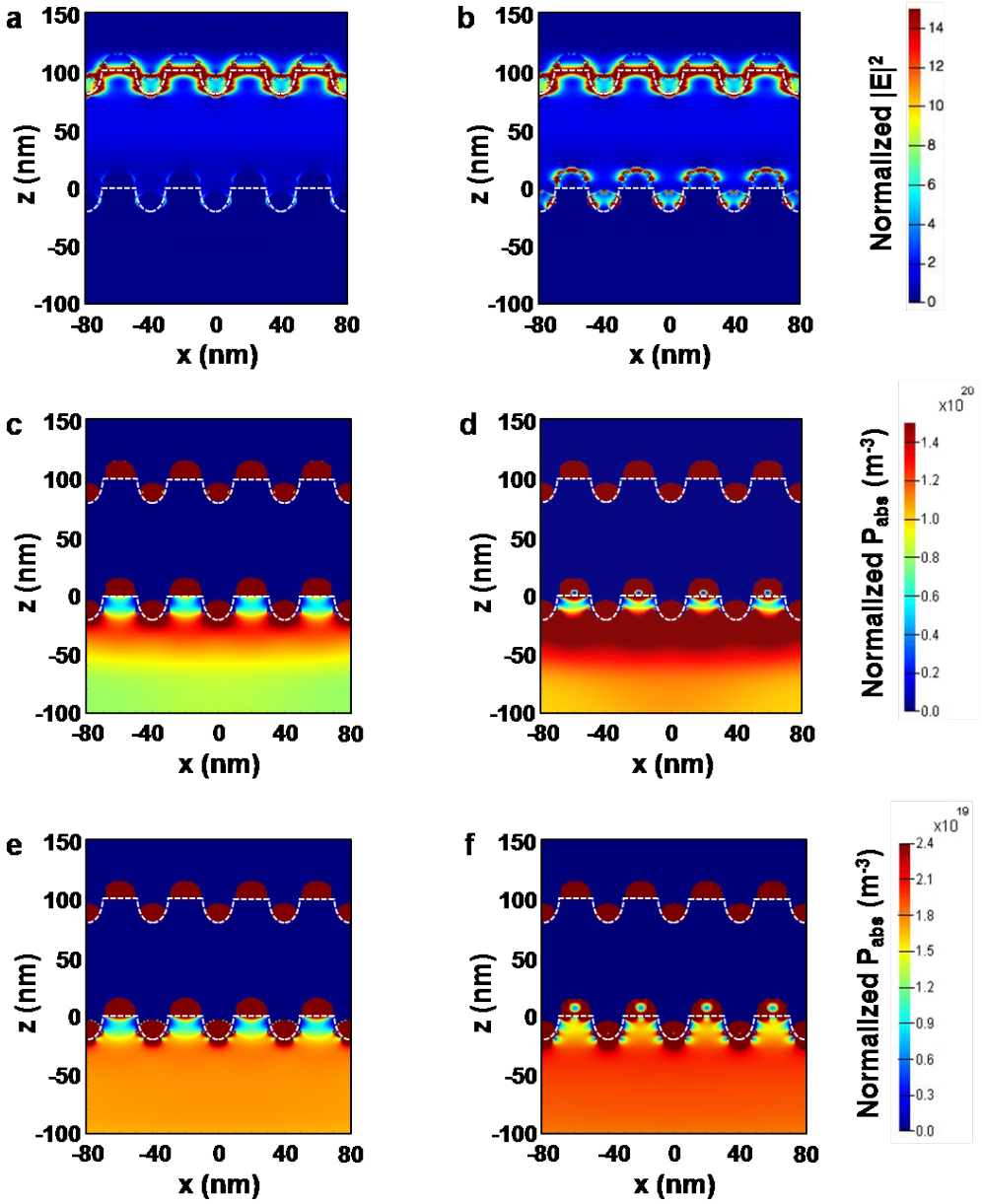


**Figure 4.14 Calculated electric field intensity profiles under incident light of 400nm for x-z plane of (a) Au/Ag quadruple plasmonic layer and (b) Ag/Ag quadruple plasmonic layer on Si. Calculated power absorption profiles under an incident light of 400 nm (c and d) and 600 nm (e and f) for x-z plane of Au/Ag quadruple plasmonic layer (c and e) and Ag/Ag quadruple plasmonic layer on Si.White dotted lines show surfaces of Silicon (near 0 nm) and spin on glass (near 100 nm).**

## 4.6 Ultrathin Solar Cells based on UMG-Si

### 4.6.1 Fabrication of Ultrathin UMG-Si Solar Cells

The bulk UMG-Si wafer was lapped and polished using chemical mechanical polisher to reduce the thickness down to 12 µm. Then the wafer was doped with phosphorous and boron on the topside and the backside respectively using solid source targets (PH-1000N, BN-1250, Saint Gobain) to make p-i-n junction. The diffusion doping was conducted at 1000°C in Ar ambient for 20 minutes. To make contact on the boron-doped side, thin layer of Al was sputtered on the backside of the wafer. The wafer was cut and pasted to Ti/Au coated polyamide film for easy handling.

Fig. 4.15 (a) shows the prepared 12 µm thick UMG-Si piece which is bendable up to 10 mm of bending radius without fracture due to the small thickness. The completed ultrathin UMG-Si solar cell for measurement is shown in Fig. 4.15 (b).

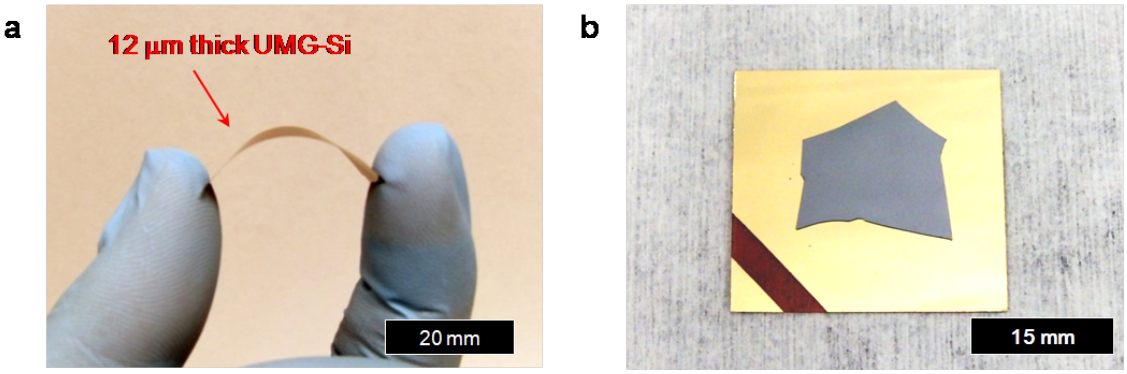


**Figure 4.15(a) Optical image of a 12 µm thick UMG-Si. Due to the small thickness, the UMG-Si solar cell was bendable up to ~ 10 mm of bending radius. (b) The ultrathin UMG-Si was processed by attaching the sample on a polymide (125 µm) /Ti (20 nm)/Au (200 nm) substrate for easy handling and measurement.**

### 4.6.2 Electrical and Optical Characteristics of Ultrathin UMG-Si Solar Cells

The J-V measurements of both ultrathin (12μm) and bulk (180μm) solar cells generated from UMG-Si were carried out under illumination of 1 sun. J-V measurement results of 17μm thick solar microcells presented in Chapter 3.4.1 exhibited that short carrier collection pathway improves the conversion efficiency (η) which is concomitant with the increase in the photocurrent ($J_{sc}$). Fig. 4.16 (a) shows the J-V curves of the ultrathin solar cell and the bulk solar cell and their detailed J-V characteristics are in Table. 4-6. In case of 12 μm thick UMG-Si solar cell, the short circuit current density ($J_{SC}$) was measured to be smaller (9.53mA/cm$^2$) compared to that of bulk (180μm) UMG-Si solar cell even though much shorter carrier collection pathway was provided. Due to the significant decline in the photocurrent in the ultrathin solar cell, other related parameters such as open circuit voltage ($V_{OC}$), fill factor (FF), and finally efficiency (η) decreased as well.

For further investigation of optical property in the 12μm Si, optical absorptance calculations of Si in 12μm and in 180μm thicknesses were carried out using the Essential Macleod. The calculation shown in Fig. 4.16 (b) manifests serious optical loss in the 12μm Si as its absorptance drops sharply from wavelength of 600nm. In this case, loss of photogenerated carriers outweighs enhanced photogenerated carrier collection and that results in diminished overall performance of the device.

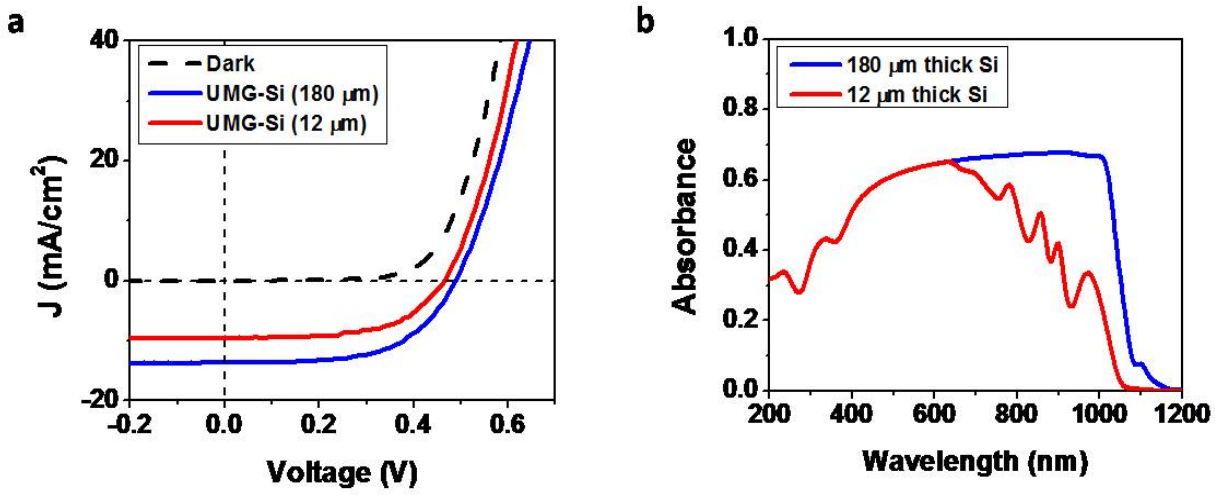


**Figure 4.16 (a) Calculated absorbance spectrum of the 180 μm thick Si (blue) and the 12 μm thick Si (red). The absorbance of the 12 μm Si decreased significantly in the long wavelength region. (b) J-V curves of the 180 μm thick UMG-Si solar cell (blue) and the 12 μm thick UMG-Si solar cell (red) under light (1000W/m$^2$). Compared to the $J_{SC}$ of the 180 μm thick UMG-Si solar cell, the $J_{SC}$ of the 12 μm thick UMG-Si solar cell was decreased by 30% due to the low absorbance at the long wavelength region.**

**Table 4-6 J-V characteristics of a 12 μm thick bare UMG-Si solar cell and a 180 μm thick bare UMG-Si solar cell.**

| Solar cells | $J_{SC}$ (mA/cm$^2$) | $V_{OC}$(V) | FF | η (%) |
|---|---|---|---|---|
| 12 μm thick UMG-Si | 9.53 | 0.46 | 0.59 | 2.59 |
| 180 μm thick UMG-Si | 13.67 | 0.49 | 0.58 | 3.88 |

## 4.7 Quadruple Plasmonic Layer on Ultrathin UMG-Si Solar Cells

Throughout the experiments of fabricating bulk (180μm thick) UMG-Si solar cells with various light trapping features and investigating their electrical and optical properties, we found out the optimum material and surface design that maximizes the light trapping. Our ultimate goal is to integrate these nanostructures to the ultrathin (12 μm thick) UMG-Si solar cell. Therefore, by employing all the conditions that were

discovered so far, we produced ultrathin UMG-Si solar cell with quadruple plasmonic layer. The quadruple plasmonic layer has a bottom double plasmonic layer composed of Ag nanoparticles, a SOG layer (100 nm thick), and a top double plasmonic layer composed of Ag nanoparticles. The optical image of ultrathin UMG-Si solar cell without and with quadruple plasmonic layer is shown in Fig. 4.17 (a) and (b) respectively. Compared to the bare ultrathin UMG-Si substrate, the presence of Ag based quadruple plasmonic layer greatly decreases the reflection of light from the sample surface. As a consequence, the color of the cell becomes significantly darker after the incorporation of the quadruple plasmonic layer.

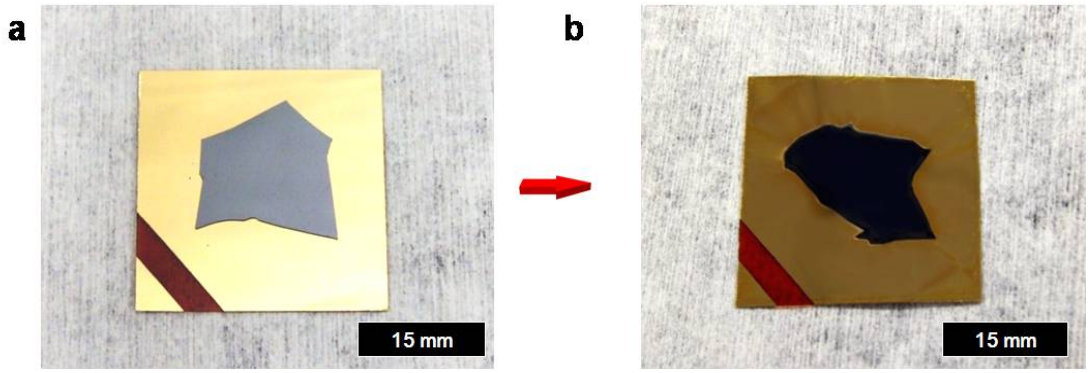


**Figure 4.17 Optical images of ultrathin (12 μm) UMG-Si solar cells (a) without and (b) with the Ag based quadruple plasmonic layers on the surface.**

Fig. 4.18 shows the J-V measurements for a 12 μm thick bare UMG-Si cell, as well as same type of cell coated with the quadruple plasmonic layer under 1000W/m$^2$ of light in room temperature. $J_{SC}$ for the UMG-Si cell without and with the quadruple plasmonic layer were measured to be 9.53mA/cm$^2$ and 31.16mA/cm$^2$ respectively. The corresponding solar cell conversion efficiencies were measured to be 2.59% and 10.73%

respectively. The results show that incorporating quadruple plasmonic layer increased the efficiency of the ultrathin UMG-Si solar cell by greater than 400%.

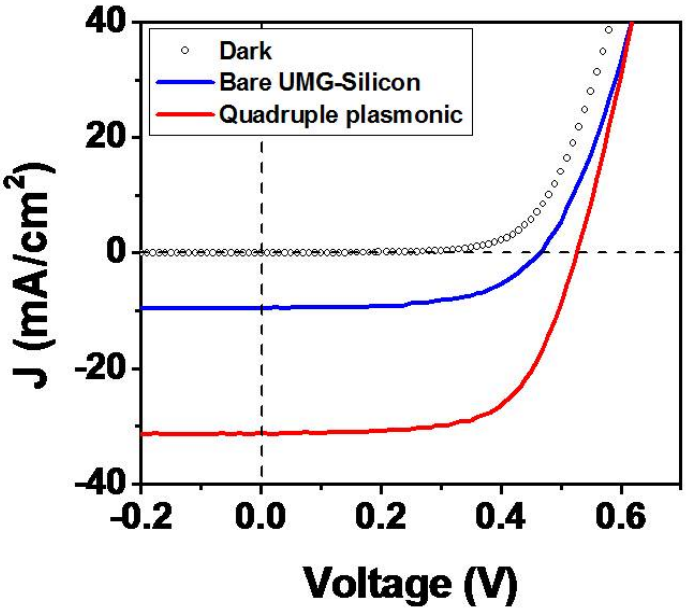


**Figure 4.18 Representative J-V curves of 12 µm thick UMG-Si solar cells without (blue) and with (red) Ag based quadruple plasmonic layer under light (1000 W/m$^2$).**

**Table 4-7 J-V characteristics of the 12 µm thick bare UMG-Si and the Ag based quadruple plasmonic layer (Ag-QPL) on UMG-Si.**

| Solar cells | $J_{SC}$ (mA/cm$^2$) | $V_{OC}$ (V) | FF | η (%) |
|---|---|---|---|---|
| Bare UMG-Silicon | 9.53 | 0.46 | 0.59 | 2.59 |
| Ag-QPL on UMG-Silicon | 31.16 | 0.53 | 0.65 | 10.73 |

## 4.8 Conclusion

The results of this work illustrate that multiple-plasmonic layers composed of double or quadruple metallic plasmonic nanoparticle layers can be used to fabricate ultrathin Si solar cells with nearly perfect light absorption. Our quadruple plasmonic layers where fabricated on ultrathin (12 μm), low-cost UMG-Si substrates, and exhibit significantly enhanced $J_{SC}$, $V_{OC}$, and FF over bulk cells, resulting in overall solar cell efficiencies almost ~ 11%. The developed cells are flexible, use relatively impure and small amount of Si, thereby potentially addressing both the material and installation costs for Si based solar cells.

Systematic studies on the optical and electrical properties of the quadruple plasmonic layers elucidate the light trapping effects of each individual component within the developed module. FDTD calculations help explain the mechanisms behind the enhanced absorption caused by each double plasmonic layer and the SOG. The results of this work may provide useful design direction for the future work on UMG-Si based solar cells.

# Chapter 5

# Conclusion

## 5.1 Nanostructures for Light Trapping

The properties of surface plasmons in nanoscale metallic features has been explored extensively as the synthetic techniques that enables numerous ways of realizing nanostructures with well-controllable composition, size, and shape have developed. Various nanofabrication techniques showing excellent yields are currently available and we obtained metallic nanoparticles with diameters smaller than 100 nm by means of block copolymer self-assembly which allows inexpensive and simple process. The major interest of LSPRs in metallic nanoparticles on dielectric substrates lies in potential to confine light to the metal/dielectric interface which in turn generates intense local electromagnetic fields. Therefore LSPR can provide substantial photocurrent enhancement when applied to weak light absorbing solar cells.

We introduced various nanostructures generated from metallic nanoparticles that can significantly improve the light absorption of ultrathin Si. They are mainly divided into two categories: (1) Ag nanoparticle/ Si nanopillar array and (2) Quadruple plasmonic layers.

**(1) Ag nanoparticle/ Si nanopillar arrays**

The structure of Ag nanoparticle/ Si nanopillar arrays on ultrathin Si was proven to enhance the light absorption and conversion efficiency of the solar cell by greater than ~170%. The mechanism of absorption enhancement arising from the presence of the structures is combinations of LSPR at Ag nanoparicles and scattering of light at Si nanopillars. Separate ananlysis of Ag nanoparticles and Si nanopillar revealed that increase in the efficiency mostly stems from the contribution of Si nanopillars.

**(2) Quadruple plasmonic layers**

There have been huge amount of research on distribution of metallic nanoparticles on dielectric substrates. The quadruple plasmonic layer is an evolved plasmonic structure for maximizing light absorption from LSPR. The ultrathin Si solar cell incorporating quadruple plasmonic layer resulted in increase in the conversion efficiency by ~400%. The mechanism of absorption enhancement stems from LSPR at four layers of Ag nanoparticles placed inside and outside Si and from anti-reflection from thin $SiO_2$ layer. Studying each component comprising the quadruple plasmonic layer revealed that higher than 90% of absorbance throughout the entire spectrum can be achieved by using this structure.

## 5.2 Outlook

The nanostructures presented here can provide absorption improvements to various classes of solar cells that suffer optical loss from material properties besides thin Si. By using different combinations of block copolymers, it is possible to manipulate shapes and dimensions of the nanostructures. Moreover placing light trapping

nanostructures at different locations other than the front surface such as at the rear surface or in the bulk can also lead to optical absorption enhancement in semiconductors. Exploitation of proper nanoscale characterization techniques together with optical simulation tools enables researchers to find optimized designs for solar cells composed of various materials and further investigations in this field can offer useful insights to solar cell developments.

Plasmon resonance at noble metal/dielectric interface also amplifies signals derived from techniques that rely on light. Therefore besides solar cells, there are numerous technological applications that can take advantage of surface plasmons at metallic nanoparticles such as Raman scattering [62, 139, 140], sensing [77-79], and etc. Further advancements in nanofabrication process and characterization techniques are expected to enable integration of photonic signals with electronics and make this become industrialized [137].

# Bibliography


1. Lewis, N.S., *Powering the Planet.* MRS Bulletin, 2007. **32**: p. 808-820.

2. Administration, E.I., *Renewable Energy Consumption and Electricity Preliminary 2007 Statistics.* 2008.

3. Lewis, N.S., *Toward cost-effective solar energy use.* Science, 2007. **315**(5813): p. 798-801.

4. Horiuchi, T., et al., *High efficiency of dye-sensitized solar cells based on metal-free indoline dyes.* J Am Chem Soc, 2004. **126**(39): p. 12218-9.

5. Scharber, M.C., et al., *Design Rules for Donors in Bulk-Heterojunction Solar Cells - Towards 10% Energy -Conversion Efficiency.* Advanced Materials, 2006. **18**(6): p. 789-794.

6. Yang, F., M. Shtein, and S.R. Forrest, *Controlled growth of a molecular bulk heterojunction photovoltaic cell.* Nature Materials, 2005. **4**: p. 37-41.

7. Gunes, S., H. Neugebauer, and N.S. Sariciftci, *Conjugated polymer-based organic solar cells.* Chem Rev, 2007. **107**(4): p. 1324-38.

8. Park, S.H., et al., *Bulk heterojunction solar cells with internal quantum efficiency approaching 100%.* Nature Photonics, 2009. **3**: p. 297-302.

9. Meyers, P.V., *Design of a thin film CdTe solar cell.* Solar Cells, 1988. **23**(1-2): p. 59-67.

10. Chu, T.L., et al., *13.4% efficient thin-film CdS/CdTe solar cells.* Jounal of Applied Physics, 1991. **70**(12): p. 7608-7612.

11. Romeo, N., et al., *A highly efficient and stable CdTe/CdS thin film solar cell.* Solar Energy Materials and Solar Cells, 1999. **58**(2): p. 209-218.

12. Wada, T., et al., *High-efficiency CIGS solar cells with modified CIGS surface.* Solar Energy Materials and Solar Cells, 2001. **67**(1-4): p. 305-310.

13. Naghavi, N., et al., *High-efficiency copper indium gallium diselenide (CIGS) solar cells with indium sulfide buffer layers deposited by atomic layer chemical vapor deposition (ALCVD).* Prog. Photovolt: Res. Appl, 2003. **11**(7): p. 437-443.

14. Carlson, D.E. and D.R. Wronski, *Amorphous silicon solar cell.* Applied Physics Letters, 1976. **28**(11): p. 671-673.

15. Staebler, D.L., R.S. Carndall, and R. Willliams, *Stability of n-i-p amorphous silicon solar cells.* Applied Physics Letters, 1981. **39**(9): p. 733-735.

16. Shah, A.V., et al., *Thin-film silicon solar cell technology.* Prog. Photovolt: Res. Appl, 2004. **12**: p. 113-142.

17. Fraas, L.M., et al., *GaSb Booster cells for over 30% efficient solar-cell stacks.* Journal of Applied Physics, 1989. **66**(8): p. 3866-3870.

18. Bertness, K.A., et al., *29.5%-efficient GaInp/GaAs tandem solar cells.* Applied Physics Letters, 1994. **65**(8): p. 989-991.

19. Geisz, J.F., et al., *High-efficiency GaInP/GaAs/InGaAs triple-junction solar cells grown inverted with a metamorphic bottom junction.* Applied Physics Letters, 2007. **91**(2): p. 023502-023505.

20. Ramanarhan, K., et al., *Properties of 19.2% efficiency ZnO/CdS/CuInGaSe$_2$ thin-film solar cells.* Progress in Photovoltaics: Research and Applications, 2003. **11**(4): p. 225-230.

21. J.Katayama, et al., *Performance of Cu$_2$O/ZnO Solar Cell Prepared by Two-Step Electrodeposition.* Journal of Applied Electrochemistry, 2004. **34**(7): p. 687-692.

22. Bagnall, D.M. and M. Boreland, *Photovoltaic Technologies.* Energy Policy, 2008. **36**: p. 4390-4396.

23. Ginley, D., M.A. Green, and R. Collins, *Solar Energy Conversion Toward 1 Terawatt.* MRS Bulletin, 2008. **33**: p. 355-372.

24. Surek, T., *Crystal growth and materials research in photovoltaics: progress and challenges.* Journal of Crystal Growth, 2005. **275**(1–2): p. 292-304.

25. Shockley, W. and H.J. Queisser, *Detailed Balance Limit of Efficiency of p-n Junction Solar Cells.* Journal of Applied Physics, 1961. **32**(3): p. 510-519.

26. Wang, A., J. Zhao, and M.A. Green, *24% efficient silicon solar cells.* Applied Physics Letters, 1990. **57**(6): p. 602-604.

27. Morita, K. and T. Miki, *Thermodynamics of solar-grade silicon refining.* Intermetallics, 2003. **11**: p. 1111-1117.

28. Canizo, C.d., G.d. Coso, and W.C. Sinke, *Crystalline silicon solar module technology : Towards the 1€ per watt-peak goal.* Progress in Photovoltaics: Research and Applications, 2008. **17**(3): p. 199-209.

29. Luque, A. and S. Hegedus, *Handbook of Photovoltaic Science and Engineering*2011: John Wiley & Sons.

30. Mauk, M.G., *Silicon Solar Cells: Physical Metallurgy Principles.* JOM, 2003: p. 38-42.

31. Bathey, B.R. and M.C. Cretella, *Review Solar-grade Silicon.* Journal of Materials Science, 1982. **17**: p. 3077-3096.

32. Wolf, S.D., et al., *Solar cells from upgraded matallurgical grade (UMG) and plasma-purified UMG-multicrystalline silicon substrates.* Solar Energy Materials and Solar Cells, 2002. **72**: p. 49-58.

33. Kohler, D., et al., *Upgraded metallurgical Grade Silicon Solar Cells: A Detailed Material Analysis.* 24th EU PVSEC, 2009: p. 21-25.

34. Kwapil, W., et al., *High net doping concentration responsible for critical diode breakdown behavior of upgraded metallurgical grade multicrystalline silicon solar cells* J. Appl. Phys., 2010. **108**(2): p. 023708-023708-6.

35. *2008 Solar Technologies Market Report*. 2010.

36. Kayes, B.M., H.A. Atwater, and N.S. Lewis, *Comparison of the device physics principles of planar and radial p-n junction nanorod solar cells* Jounal of Applied Physics, 2005. **97**(11): p. 114302-114302-11.

37. Garnett, E.C. and P. Yang, *Silicon Nanowire Radial p-n Junction Solar Cells.* J. Am. Chem. Soc., 2008. **130**(29): p. 9224-9225.

38. *Direct and Global 37 Deg Tilt: ASTM G-173*, A.S.o.T.a. Measurement, Editor.

39. Pierret, R.F., *Semiconductor Device Fundamentals*1996: Addison Wesley.

40. Nelson, J., *The Physics of Solar Cells*2003: Imperial College Press.

41. Cui, Y., et al., *High Performance Silicon Nanowires Field Effect Transistors.* Nano Lett, 2003. **3**(2): p. 149-152.

42. Shan, Y., et al., *From Si Source Gas Directly to Positioned, Electrically Contacted Si Nanowires: The Self-Assembling "Growth-in-Place" Approach.* Nano Lett, 2004. **4**(11): p. 2085-2089.

43. Arnold., M.S., et al., *Field-Effect Transistors Based on Single Semiconducting Oxide Nanobelts.* J. Phys. Chem. B, 2003. **107**(3): p. 659-663.

44. Roberts, M.M., et al., *Elastically relaxed free-standing strained-silicon nanomembranes.* Nat Mater, 2006. **5**(5): p. 388-93.

45. Sirringhaus, H., N. Tessler, and R.H. Friend, *Integrated optoelectronic devices based on conjugated polymers.* Science, 1998. **280**(5370): p. 1741-4.

46. Katz, H.E., Z. Bao, and S.L. Gilat, *Synthetic Chemistry for Ultrapure, Processable, and High-Mobility Organic Transistor Semiconductors.* Acc. Chem. Res., 2001. **34**(5): p. 359-369.

47. Khang, D.Y., et al., *A stretchable form of single-crystal silicon for high-performance electronics on rubber substrates.* Science, 2006. **311**(5758): p. 208-12.

48. Baca, A.J., et al., *Printable Single-Crystal Silicon Micro/Nanoscale Ribbons, Platelets, and Bars Generated from Bulk Wafers.* Adv. Funct. Mater., 2007. **17**: p. 3051-3062.

49. Baca, A.J., et al., *Semiconductor wires and ribbons for high-performance flexible electronics.* Angew Chem Int Ed Engl, 2008. **47**(30): p. 5524-42.

50. Willets, K.A. and R.P.V. Duyne, *Localized Surface Plasmon Resonance and Spectroscopy and Sensing.* Annu. Rev. Phys. Chem., 2007. **58**: p. 267-297.

51. Chan, G.H., et al., *Plasmonic Properties of Copper Nanoparticles Fabricated by Nanosphere Lithography.* Nano Lett, 2007. **7**(7): p. 1947-1952.

52. Maier, S.A., et al., *Local detection of electromagnetic energy transport below the diffraction limit in metal nanoparticle plasmon waveguides.* Nat Mater, 2003. **2**(4): p. 229-32.

53. Bohren, C.F. and D.R. Huffman, *Absorption and Scattering of Light by Small Particles*1983: Wiley-VCH.

54. Maier, S.A. and H.A. Atwater, *Plasmonics: Localization and guiding of electromagnetic energy in metal/dieletric structures.* Journal of Applied Physics, 2005. **98**(1): p. 011101-011101-10.

55. Maier, S.A., *Plasmonics: Fundamentals and Applications*2007: Springer.

56. Xu, G., et al., *Wavelength tuning of surface plasmon resonance using dieletric layers on silver island films.* Applied Physics Letters, 2003. **82**(22).

57. Mertens, H., et al., *Infrared surface plasmons in two-dimensional silver nanoparticles arrays in silicon* Applied Physics Letters, 2004. **85**(8): p. 1317-1319.

58. Beck, F.J., A. Polman, and K.R. Catchpole, *Tunable light trapping for solar cells using localized surface plasmons.* Journal of Applied Physics, 2009. **105**(11): p. 114310-114310-7.

59. Atwater, H.A. and A. Polman, *Plasmonics for improved photovoltaic devices.* Nat Mater, 2010. **9**(3): p. 205-13.

60. Stockman, M.I., *Nanoplasmonics: The physics behind the applications.* Physics Today, 2011. **64**(2): p. 39-44.

61. Xia, Y., N. J.Halas, and G. Editors, *Shape-Controlled Synthesis and Surface Plasmonic Properties of Metallic Nanostructures.* MRS Bulletin, 2005. **30**: p. 338-348.

62. Nie, S. and S.R. Emory, *Probing Single Molecules and Single Nanoparticles by Surface-Enhanced Raman Scattering.* Science, 1997. **275**(5303): p. 1102-6.

63. Maier, S.A., *Plasmonic field enhancement and SERS in the effective mode volume picture.* Opt Express, 2006. **14**(5): p. 1957-1964.

64. Mie, G., *Beiträge zur Optik trüber Medien, speziell kolloidaler Metallösungen.* Annalen der Physik, 1908. **330**(3): p. 377-445.

65. Catchpole, K.R. and A. Polman, *Plasmonic solar cells.* Opt Express, 2008. **16**(26): p. 21793-800.

66. Ferry, V.E., et al., *Plasmonic Nanostructure Design for Efficient Light Coupling into Solar Cells.* Nano Lett, 2008. **8**(12): p. 4391-4397.

67. Catchpole, K.R. and A. Polman, *Design principles for particle plasmon enhanced solar cells* Appl . Phys. Lett, 2008. **93**(19): p. 191113-191113-3.

68. Rockstuhl, C., S. Fahra, and F. Lederer, *Absorption enhancement in solar cells by localized plasmon polaritons.* Journal of Applied Physics, 2008. **104**(123102).

69. Derkacs, D., et al., *Improved performance of amorphous silicon solar cells via scattering from surface plasmon polaritons in nearby metallic nanoparticles.* Applied Physics Letters, 2006. **89**(9): p. 093103-093103-3.

70. Ferry, V.E., et al., *Plasmonic nanostructure design for efficient light coupling into solar cells.* Nano Lett, 2008. **8**(12): p. 4391-7.

71. Li, X., et al., *Dual Plasmonic Nanostructures for High Performance Inverted Organic Solar Cells.* Advanced Materials, 2012. **24**(22): p. 3046-3052.

72. Mock, J.J., et al., *Shape effects in plasmon resonance of individual colloidal silver nanoparticles* J. Chem. Phys., 2002. **116**(15): p. 6755-6759.

73. Maier, S.A., et al., *Observation of near-field coupling in metal nanoparticle chains using far-field polarization spectroscopy.* Phys. Rev. B, 2002. **65**(19).

74. Krenn, J.R., et al., *Light field propagation by metal micro- and nanostructures.* Journal of Microscopy, 2001. **202**(1): p. 122-128.

75. Elghanian, R., et al., *Selective colorimetric detection of polynucleotides based on the distance-dependent optical properties of gold nanoparticles.* Science, 1997. **277**(5329): p. 1078-81.

76. Nath, N. and A. Chilkoti, *A colorimetric gold nanoparticle sensor to interrogate biomolecular interactions in real time on a surface.* Anal Chem, 2002. **74**(3): p. 504-9.

77. Haes, A.J., et al., *A Localized Surface Plasmon Resonance Biosensor: First Steps toward an Assay for Alzheimer's Disease.* Nano Lett, 2004. **4**(6): p. 1029-1034.

78. Kim, S., et al., *Localized surface plasmon resonance (LSPR) sensitivity of Au nanodot patterns to probe solvation effects in polyelectrolyte brushes.* Chem Commun (Camb), 2008(31): p. 3666-8.

79. Shin, D.O., et al., *A plasmonic biosensor array by block copolymer lithography.* J. Mater. Chem., 2010. **20**: p. 7241-7247.

80. Krenn, J.R., *Nanoparticle waveguides: Watching energy transfer.* Nat Mater, 2003. **2**(4): p. 210-1.

81. Stockman, M.I., *Nanofocusing of Optical Energy in Tapered Plasmonic Waveguides.* Phys Rev Lett, 2004. **93**(13): p. 137404.

82. Veronis, G. and S. Fan, *Bends and splitters in metal-dielectric-metal subwavelength plasmonic waveguides* Applied Physics Letters, 2005. **87**(13): p. 131102-131102-3.

83. Kneipp, K., et al., *Surface-enhanced Raman scattering and biophysics.* J. Phys.: Condens. Matter, 1999. **14**(18).

84. Dieringer, J.A., et al., *Surface-enhanced Raman excitation spectroscopy of a single rhodamine 6G molecule.* J Am Chem Soc, 2009. **131**(2): p. 849-54.

85. Stuart, H.R. and D.G. Hall, *Island size effects in nanoparticle-enhanced photodetectors* Appl . Phys. Lett, 1998. **73**(26): p. 3815-3817.

86. Rand, B.P., P. Peumans, and S.R. Forrest, *Long-range absorption enhancement in organic tandem thin-film solar cells containing silver nanoclusters.* J. Appl. Phys., 2004. **96**(12): p. 7519-7526.

87. Pillai, S., et al., *Surface plasmon enhanced silicon solar cells* J. Appl. Phys., 2007. **101**(9).

88. Zhu, J., et al., *Nanodome solar cells with efficient light management and self-cleaning.* Nano Lett, 2010. **10**(6): p. 1979-84.

89. Stephen Y. Chou, Peter R. Krauss, and P.J. Renstrom, *Nanoimprint lithography.* J. Vac. Sci. Technol. B, 1996. **14**(6): p. 4129-4133.

90. Schift, H., *Nanoimprint lithography: An old stroy in modern times? A review.* J. Vac. Sci. Technol. B, 2008. **26**(2): p. 458-480.

91. Bates, F.S. and G.H. Fredrickson, *Block Copolymers-Designer Soft Materials.* Phys. Today, 1999. **52**(32): p. 32-38.

92. Bates, F.S. and G.H. Fredrickson, *Block copolymer thermodynamics: theory and experiment.* Annu Rev Phys Chem, 1990. **41**: p. 525-57.

93. Bates, F.S., *Polymer-Polymer Phase Behavior.* Science, 1991. **251**(4996): p. 898-905.

94. van Hest, J.C.M., et al., *Polystyrene-Dendrimer Amphiphilic Block Copolymers with a Generation-Dependent Aggregation.* Science, 1995. **268**(5217): p. 1592-1595.

95. Zhang, L. and A. Eisenberg, *Multiple Morphologies of "Crew-Cut" Aggregates of Polystyrene-b-poly(acrylic acid) Block Copolymers.* Science, 1995. **268**.

96. Zhang, L., K. Yu, and A. Eisenberg, *Ion-Induced Morphological Changes in "Crew-Cut" Aggregates of Amphiphilic Block Copolymers.* Science, 1996. **272**(5269): p. 1777-1779.

97. Park, M., et al., *Block Copolymer Lithography: Periodic Arrays of ~$10^{11}$ Holes in 1 Square Centimeter* Science, 1997. **276**: p. 1401-1404.

98. Ouk Kim, S., et al., *Epitaxial self-assembly of block copolymers on lithographically defined nanopatterned substrates.* Nature, 2003. **424**(6947): p. 411-414.

99. Cheng, J.Y., et al., *Dense Self-Assembly on Sparse Chemical Patterns: Rectifying and Multiplying Lithographic Patterns Using Block Copolymers.* Advanced Materials, 2008. **20**(16): p. 3155-3158.

100. Lee, D.H., et al., *Hierarchically Organized Carbon Nanotube Arrays from Self-Assembled Block Copolymer Nanotemplates.* Advanced Materials, 2008. **20**(13): p. 2480-2485.

101. Lee, D.H., W.J. Lee, and S.O. Kim, *Highly Efficient Vertical Growth of Wall-Number-Selected, N-Doped Carbon Nanotube Arrays.* Nano Lett, 2009. **9**(4): p. 1427-1432.

102. Jeong, S.-J., et al., *Universal Block Copolymer Lithography for Metals, Semiconductors, Ceramics, and Polymers.* Advanced Materials, 2008. **20**(10): p. 1898-1904.

103. Cheng, J.Y., A.M. Mayes, and C.A. Ross, *Nanostructure engineering by templated self-assembly of block copolymers.* Nat Mater, 2004. **3**(11): p. 823-8.

104. Hawker, C.J. and T.P. Russell, *Block Copolymer Lithography: Merging "Bottom-Up" with "Top-Down" Processes.* MRS Bulletin, 2005. **30**(12): p. 952-966.

105. Segalman, R.A., *Patterning with block copolymer thin films.* Materials Science and Engineering: R: Reports, 2005. **48**(6): p. 191-226.

106. Hamley, I.W., *Nanotechnology with Soft Materials.* Angewandte Chemie International Edition, 2003. **42**(15): p. 1692-1712.

107. Black, C.T. *Integration of self assembly for semiconductor microelectronics*. in *Custom Integrated Circuits Conference, 2005. Proceedings of the IEEE 2005*. 2005.

108. Lazzari, M. and M.A. López-Quintela, *Block Copolymers as a Tool for Nanomaterial Fabrication.* Advanced Materials, 2003. **15**(19): p. 1583-1594.

109. Jaeger, R.C., *Introduction to microelectronic fabrication*1988: Addison-Wesley Publishing Company, Inc.

110. Hull, R., *Properties of Crystalline Silicon*1999, London: INSPEC.

111. Zschech, D., et al., *Ordered Arrays of ⟨100⟩-Oriented Silicon Nanorods by CMOS-Compatible Block Copolymer Lithography.* Nano Lett, 2007. **7**(6): p. 1516-1520.

112. Kwon, J.Y., et al., *High efficiency thin upgraded metallurgical-grade silicon solar cells on flexible substrates.* Nano Lett, 2012. **12**(10): p. 5143-7.

113. Hu., L. and G. Chen., *Analysis of Optical Absorption in Silicon Nanowire Arrays for Photovoltaic Applications.* Nano Lett, 2007. **7**(11): p. 3249-3252.

114. Zhu, J., et al., *Optical absorption enhancement in amorphous silicon nanowire and nanocone arrays.* Nano Lett, 2009. **9**(1): p. 279-82.

115. Spinelli, P., M.A. Verschuuren, and A. Polman, *Broadband omnidirectional antireflection coating based on subwavelength surface Mie resonators.* Nat Commun, 2012. **3**: p. 692.

116. Hicks, E.M., et al., *Controlling plasmon line shapes through diffractive coupling in linear arrays of cylindrical nanoparticles fabricated by electron beam lithography.* Nano Lett, 2005. **5**(6): p. 1065-70.

117. Chou, S.Y., P.R. Krauss, and P.J. Renstrom, *Imprint Nanolithography with 25-Nanometer Resolution.* Science, 1996. **272**: p. 85-87.

118. Park, S., et al., *Macroscopic 10-terabit-per-square-inch arrays from block copolymers with lateral order.* Science, 2009. **323**(5917): p. 1030-3.

119. Chang, S.-w., et al., *Metal-Catalyzed Etching of Vertically Aligned Polysilicon and Amorphous Silicon Nanowire Arrays by Etching Direction Confinement.* Advanced Functional Materials, 2010. **20**(24): p. 4364-4370.

120. Maier, S.A., P.G. Kik, and H.A. Atwater, *Observation of coupled plasmon-polariton modes in Au nanoparticle chain waveguides of different lengths: Estimation of waveguide loss* Appl. Phys. Lett., 2002. **81**(9): p. 1714-1716.

121. Johnson, P.B. and R.W. Christy, *Optical Constants of the Noble Metals.* Physical Review B, 1972. **6**(12): p. 4370-4379.

122. Palik, E.D., *Handbook of Optical Constants of Solids*1991: Academic Press.

123. Yoon, J., et al., *Ultrathin silicon solar microcells for semitransparent, mechanically flexible and microconcentrator module designs.* Nat Mater, 2008. **7**(11): p. 907-15.

124. Baca, A.J., et al., *Compact monocrystalline silicon solar modules with high voltage outputs and mechanically flexible designs.* Energy & Environmental Science, 2010. **3**(2): p. 208-211.

125. Staebler, D.L. and C.R. Wronski, *Reversible conductivity changes in discharge-produced amorphous Si* Appl . Phys. Lett, 1977. **31**(4).

126. Strutzmann, M., W.B. Jackson, and C.C. Tsai, *Kinetics of the Staebler-Wronski effect in hydrogenated amorphous silicon.* Appl . Phys. Lett, 1984. **45**(10): p. 1075-1077.

127. Crandall, R.S., *Defect relaxation in amorphous silicon: Stretched exponentials, the Meyer-Neldel rule, and the Staebler-Wronski effect.* Physical Review B, 1991. **43**(5): p. 4057-4070.

128. Fritzsche, H., *Photo-induced structural changes associated with the Staebler-Wronski effect in hydrogenated amorphous silicon.* Solid State Communications, 1995. **94**(12): p. 953-955.

129. Zhao, J. and M.A. Green, *Optimized antireflection coatings for high-efficiency silicon solar cells* Electron Devices, IEEE Transactions on, 1991. **38**(3): p. 1925-1934.

130. Richards, B.S., *Comparison of TiO2 and other dielectric coatings for buried-contact solar cells: a review.* Progress in Photovoltaics: Research and Applications, 2004. **12**(4): p. 253-281.

131. Zhou, W., et al., *Microstructured surface design for omnidirectional antireflection coatings on solar cells* J. Appl. Phys., 2007. **102**(10): p. 103105-103105-9.

132. Das, U.K., et al., *Surface passivation and heterojunction cells on Si (100) and (111) wafers using dc and rf plasma deposited Si:H thin films.* Applied Physics Letters, 2008. **92**(6): p. 063504-063504-3.

133. Green, M.A., *Limiting efficiency of bulk and thin-film silicon solar cells in the presence of surface recombination.* Progress in Photovoltaics: Research and Applications, 1999. **7**(4): p. 327-330.

134. Kretschmann, E. and H. Raether, *Radiative decay of nonradiative surface plasmons excited by light.* Z. Naturforsch., 1968. **A23**: p. 2135-2136.

135. Otto, A., *Excitation of nonradiative surface plasma waves in silver by the method of frustrated total reflection.* Zeitschrift für Physik, 1968. **216**(4): p. 398-410.

136. Ritchie, R.H., et al., *Surface-Plasmon Resonance Effect in Grating Diffraction.* Phys Rev Lett, 1968. **21**(22): p. 1530-1533.

137. Barnes, W.L., A. Dereux, and T.W. Ebbesen, *Surface plasmon subwavelength optics.* Nature, 2003. **424**(6950): p. 824-30.

138. Wei, Q.H., et al., *Plasmon Resonance of Finite One-Dimensional Au Nanoparticle Chains.* Nano Lett, 2004. **4**(6): p. 1067-1071.

139. Wang, M.H., et al., *Au nanoparticle monolayers: preparation, structural conversion and their surface-enhanced Raman scattering effects.* Nanotechnology, 2010. **21**(14): p. 145608.

140. Kneipp, K., H. Kneipp, and J. Kneipp, *Surface-enhanced Raman scattering in local optical fields of silver and gold nanoaggregates-from single-molecule Raman spectroscopy to ultrasensitive probing in live cells.* Acc Chem Res, 2006. **39**(7): p. 443-50.